POLITECNICO DI TORINO
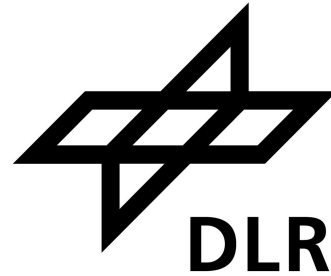
Department of Mechanical and Aerospace Engineering

Master's Degree in Aerospace Engineering

Master's Degree Thesis

Landing Simulations of a Solar-Powered High-Altitude Platform with Skid-Type Landing Gear in the Presence of Lateral Wind Disturbances

Supervisors

Prof. Matteo D. L. Dalla Vedova

Prof. Paolo Maggiore

Ing. Yasim J. Hasan

Candidate

Marco Tommasi

A. Y. 2023/2024 - March/April Session

La semplicità è la suprema sofisticazione

Leonardo da Vinci

Abstract

A so-called High-Altitude Platform (HAP) is designed for flight at very high altitudes and for a prolonged period. However, flight at low altitudes, especially in the presence of atmospheric perturbations, is challenging. Therefore, thorough investigations of the aircraft's landing capabilities and the associated limiting wind conditions are crucial for reducing the risk of a loss of the aircraft during landing. This Master's Thesis deals with landing simulations in the presence of lateral wind of different types. For this purpose, a model for lateral friction forces of a skid was developed and a lateral controller, based on THCS and a guidance block was implemented. Subsequently, several landings in the presence of lateral constant wind, wind shear and gusts with additional continuous turbulence were simulated using the controller mentioned above and the limiting cases were determined. The simulation process is evaluated through different studies: a parameter evaluation, a sensitivity analysis, a limiting cases identification and a batch evaluation process, to also include a statistical evaluation of the vehicle's responses. The results of the batch simulation show that the gust disturbances are not very critical, while the wind shear is quite effective in most cases. Additionally, the height of encounter of the disturbances, alongside with the bank angle of the vehicle during the touchdown is crucial with respect to the success of a landing.

Contents

List of Figures

List of Tables

Nomenclature

Abbreviations

AVL	Athena Vortex Lattice
CS	Certification Specification
DFT	Discrete Fourier Transform
DLR	Deutsches Zentrum für Luft- und Raumfahrt (German Aerospace Center)
DOF	Degree of Freedom
FAA	Federal Aviation Administration
FCS	Flight Control System
FFT	Fast Fourier Transform
FG&C	Flight Guidance and Control
FMA	Flight Mode Annunciation
FSF	Flight Safety Foundation
FT	Fourier Transform
HALE	High-Altitude Long-Endurance
HAP	High Altitude Platform
IQR	Interquartile Range
ISO	International Organization for Standardization
LH	Left-hand
LOC	Loss of Control
LWG	Left Wing Gear
MCP	Mode Control Pane
MG	Main Gear
MIMO	Multi-Input Multi-Output

MIT	Massachusetts Institute of Technology
NASA	National Aeronautics and Space Administration
NED	North-East-Down
NLR	Nederlands Lucht- en Ruimtevaartcentrum (Netherlands Aerospace Centre)
PC	Payload Compartment
PD	Proportional Derivative
PI	Proportional Integral
PID	Proportional Integral Derivative
PIO	Pilot Induced Oscillations
Q1	First Quartile
Q3	Third Quartile
RH	Right-hand
RWG	Right Wing Gear
RWY	Runway
SISO	Single-Input Single-Output
SLS	Standard Linear Solids
TAS	True Air Speed
TD	Touchdown
TECS	Total Energy Control System
TG	Tail Gear
THCS	Total Heading Control System
TLAR	Top-Level Aircraft Requirements
VLM	Vortex Lattice Method
VTP	Vertical Tailplane

Indices

AGL	Above Ground Level
dyn	Dynamic
eff	Effective
GE	Ground Effect

HTP   Horizontal Tailplane

SW   Sidewash

VTP   Vertical Tailplane

WB   Wing-body

Chapter 1

Introduction

This initial chapter briefly introduces the general theoretical aspects of the work done so far, and, in more detail, the motivations behind the specific work of this thesis, as well as the structure of the document. Given that this thesis work is located towards the temporal end of the project, it takes up and utilises much of the knowledge from previous years of research.

Therefore, the motivations and aims of this project will be briefly outlined, in addition to the necessary technical descriptions that serve as a basis for the current work. Then, the context, the motivation and the structure of the work will be pointed out to give a complete and clearer idea of the organisation of the document.

1.1 Context and motivation

A HAP, also known as a high-altitude long-endurance (HALE) aircraft, operates at high altitudes for extended periods, particularly in the lower stratosphere, without interfering with commercial air traffic. Unmanned solar-powered HAPs (high-altitude platforms) have the potential for permanent operation or several weeks before landing becomes necessary. Recent years have seen intensified research and various projects involving different HAP types. Drawing insights from previous works [17], the advantages of high-altitude platforms become apparent.

To begin with the clear benefits of using solar power, HAPs have an extended endurance, and to catch the majority of this energy, they need to fly at high operation altitudes. These features suggest how these vehicles are excellent candidates for applications that are usually in the scope of satellite use, such as telecommunications and Earth observation.

If used for these purposes, they take advantage of some other unique features, like the possibility of operating with flexible trajectories, which let HAPs excel in Earth observation missions, humanitarian crises surveillance, agricultural support, and health monitoring and the usage of high-resolution imaging, which enables them to capture high-resolution observation images, providing detailed information for the

above-mentioned applications. In addition to this, more continuous telecommunications support can be established, other than some secondary services like flexible and transitional communication networks, offering internet and radio support in areas with poor infrastructure or during events. Finally, no space debris is left behind, addressing this new and recent problem by combining the use of regular configuration aircraft employed for space-oriented activities.

Despite their numerous advantages, HAPs come with inherent challenges. The following points highlight key considerations and potential drawbacks associated with these innovative airborne systems.

- **High Structural Flexibility**: due to both the high aspect ratio and the low weight, HAPs usually have high flexibility, which needs to be carefully investigated to address various implications, like the aeroelastic interactions, of the structural integrity.

- **Low Operating Airspeed**: due to the need for extremely efficient flight. Since the consumed power is proportional to the cube of the operating velocity, there is an absolute need to reduce it. This also implies a very restricted velocity flight envelope, as well as a very high glide ratio (related to the aerodynamic efficiency). Such features give evidence of the need for a strict and precise flight mechanical analysis.

- **Absence of Airbrakes**: only low rates of descent are achievable, thus extreme attention needs to be paid in the landing context, both considering the ground effect and the extended airborne period during approach to the ground.

- **Small Speed Range:** HAPs face restrictions in allowable speed range due to their large altitude envelope, ranging from sea level to the lower stratosphere. In addition to this, high-lift devices are usually omitted due to weight restrictions, limiting their operational flexibility.

- **Battery Weight Penalty:** The requirement for batteries to store energy for overnight flights imposes a considerable weight penalty on HAPs, affecting their overall efficiency.

- **Communication Dependency:** As unmanned aircraft beyond the line of sight, HAPs require termination systems, adding weight, and face challenges in case of interrupted communication, necessitating a naturally stable design.

Among the above-mentioned challenges of the HAPs, some results are quite crucial for the landing phase. While the high flexibility, low airspeed and small airspeed band impose more profound flight mechanical considerations, the most critical part is flight in low altitudes. More specifically, due to very low airspeed, already small wind perturbations are influential and can heavily affect the flight stability and the interaction with the ground during the approach phase.

A flight test campaign is needed to assess the landing capabilities, and for this reason, in order to decrease the risk of a loss of aircraft, there is an absolute need to analyse the landing, understand the effects of different types and find approximate limits for allowable wind.

1.2   DLR project HAP

The German Aerospace Center (DLR) is actively involved in advancing state-of-the-art, certifiable, unmanned solar aircraft tailored for high-altitude operations in the context of the internal project HAP. Guided by the Institute of Flight Systems, DLR employs a comprehensive strategy, not only constructing a platform but also formulating a ground station, Earth observation payloads, and essential operational protocols. At the end of the project, a comprehensive flight test campaign, featuring multiple flights, is planned. This collaborative initiative involves 16 institutes specializing in aerospace, space, and security.

Since its initiation in 2018, the project's primary goal has been to assess promising technologies and design concepts while showcasing various application potentials in the domain of solar-powered high-altitude platforms. The platform itself adheres to a conventional configuration but distinguishes itself with a lightweight design, boasting a 136 kg total weight and an expansive 27 m wingspan. The sensor systems, including a high-resolution camera and a synthetic aperture radar, each weigh less than 5 kg, facilitating tasks such as monitoring shipping routes and observing ice fields. Given the platform's operational altitude of 20 kilometres, meticulous weight considerations become pivotal in both aircraft and system design, highlighting the project's commitment to precision and innovation [14].

Figure 1.1 provides an artistic impression of the HAP alpha aircraft.

Figure 1.1: Artist's impression of the HAP alpha aircraft (Source: DLR)

1.3 Outline of the project

The HAP alpha technology demonstrator is set to undergo its initial flight tests in 2025, commencing with low-altitude flights at the National Test Center for Unmanned Aerial Systems in Cochstedt. Throughout the project's progression, multiple review gates were and will be traversed, involving external subject matter experts who will evaluate the project's status and the feasibility of achieving its objectives. Currently, the project is nearing the Test Readiness Review.

Upon successful testing of the aircraft and proper training of the ground crew, the HAP alpha will incrementally ascend to altitudes of up to 20 kilometres. Subsequently, comprehensive demonstration flights incorporating payload systems will be conducted at high altitudes. To facilitate these high-altitude flights, discussions are underway with appropriate flight test facilities worldwide possessing the necessary extensive ground and air exclusion zones up to elevated altitudes [14].

1.4 Structure of this work/thesis

The different chapters of this thesis project are listed in the list below. The can be divided into two parts: the first one (of preliminary support to the subsequent) deals with the theoretical background, literature review and the controller design, and the second unravels the actual simulation process.

- **Introductive configuration**: to summarise the previous work done until this work, and state the most important specifications of the vehicle.

- **Flight dynamic model**: for deepening into the adopted dynamic model.

- **Literature research**: in particular on skid friction forces during a skewed landing (touchdown with crab angle) and on different types of ground (tarmac, grass).

- **Implementation of the lateral controller**: compliant with various requirements, ranging from performances to controllability and response similarity between the actual landing and the human-piloted one.

- **Setup for the landing simulation**: combinations of gusts of different magnitudes and associated encounter altitudes during the landing approach, as well as the formulation of evaluation criteria, based on physical and structural limitations.

- **Simulation, analysis of the results and assessment of the landing capabilities**: through the use of statistical models that consider both the deterministic behaviour of the model and pseudo-random external factors, such as atmospheric turbulence.

Chapter 2

DLR HAP configuration

The German Aerospace Center (DLR) is undertaking the development of a HAP system for Earth observation missions, which also includes the ground segment, the ground station, the different payloads for Earth observation and the operational procedures, essential for carrying out corresponding missions. The underlying vehicle can be equipped with a payload of up to 5 kilograms. The chosen configuration is a fixed-wing aircraft, dynamically generating lift for optimal station-keeping during missions. This decision stems from the performance advantages over airships, ensuring stable positioning even at higher wind speeds. The HAP system encompasses the aircraft, flight control system, operational concept, ground segment, flight termination system, and two designated instruments. The aircraft's development involves conceptual, preliminary, and detailed design phases, fabrication, a flight test campaign, and final high-altitude mission demonstrations. The project is currently in the detailed design phase. This signifies that the design has converged and only minor and detailed changes are applied. A brief description of the already completed conceptual design and the preliminary design follows. Afterwards, the flight dynamic model used within this work is outlined and the current DLR HAP configuration is presented.

2.1 Conceptual design

The initial configuration of the HAP involves determining high-level parameters such as wing area, wing span, and masses to meet top-level aircraft requirements (TLAR). The TLAR specify that the HAP must operate for a minimum of 30 days at specific geographical coordinates, carrying a 5 kg payload. Traditional conceptual design methods are complemented by a high-level mission simulation, considering the overall energy balance of the aircraft. Using TLAR-based inputs, aerodynamic lift, drag calculations, and mass approximations are performed. The resulting mass difference from the target (140 kg) is allocated to batteries.

The HAP, treated as a point mass, undergoes a kinematic mission (example in figure 2.1) with a 15-minute simulation step time. The aircraft executes a round-trip flight, harnessing solar radiation to

(a) Altitude

(b) Battery state of charge
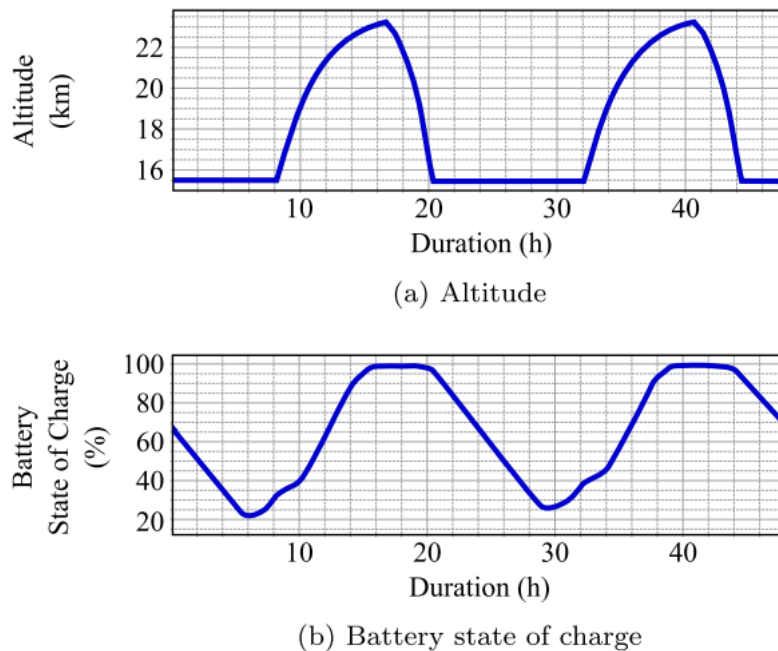
Figure 2.1: Example of mission profile [17]

charge batteries based on solar cell coverage and incidence angle. A simple controller commands climbing flight in order to gain potential energy, utilizing excess solar power. During the nighttime, altitude and thereby potential energy decrease first until a minimum is reached, and battery energy maintains this level until sunrise. Strategic heading adjustments maximize solar energy gain during low radiation periods. Feasibility is confirmed if the battery state of charge never falls below 20% throughout the mission simulation, classifying the configuration (wing area, wing span, tailplane size, and battery mass) as viable.

2.2   Preliminary design

Within the preliminary design phase, the configuration found within the conceptual design is considered more thoroughly and modified to account for all disciplinary needs. The design process for this HAP aircraft involves multiple interconnected disciplines, including aerodynamics, structure, aeroelastics, flight mechanics, and flight control. Given the challenging TLAR, compromise among disciplines is crucial. The design loops are iterative, with modifications in one area necessitating adjustments in others. For example, altering the Vertical Tailplane (VTP) requires resizing structural masses, leading to recalculations of design loads. This process involves continuous refinement, particularly in the face of the unique challenges posed by HAPs, demanding more detailed analyses than typical preliminary design approaches for conventional aircraft. The choice of control surface geometry is primarily influenced by gust rejection simulations, emphasizing the importance of an integrated flight control system. A general scheme of the

19

preliminary design phase is shown in figure 2.2.
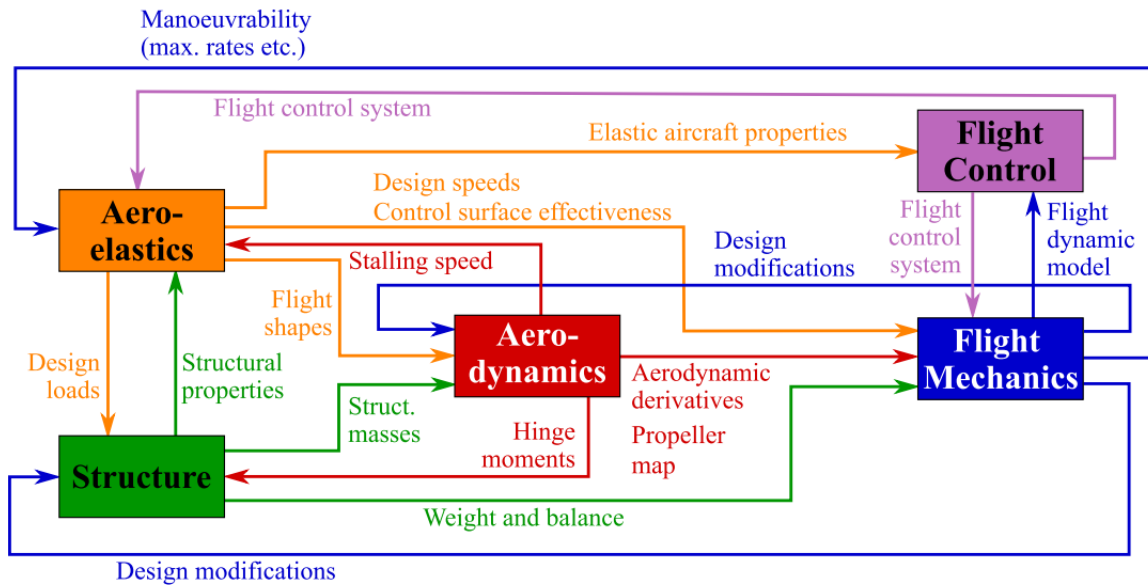
Figure 2.2: Sketch of the preliminary design working group, the disciplinary interplay and the exchange of aircraft data and results [17]

2.2.1 Aerodynamics

The aerodynamics of the HAP aircraft involve a delicate balance marked by low wing loading and dynamic operating altitudes. This profile necessitates high-lift coefficients at low Reynolds numbers, and the classical Vortex Lattice Method (VLM) plays a crucial role in shaping the airfoil design. Focusing on lift coefficients from 0.6 to 0.9, VLM determines a judicious twist distribution for optimal performance.

The unswept, high aspect ratio wing planform accentuates the intricacies of the aerodynamic wing design. Classical methods grounded in potential theory, such as the Athena Vortex Lattice (AVL) method from MIT (Massachusetts Institute of Technology), prove particularly appropriate. AVL's valuable modules enrich the entire design process, with a focus on achieving low induced drag and safe stall characteristics. In the pursuit of optimal performance, AVL determines a reasoned twist distribution for the wing. This configuration aims to achieve not only low induced drag but also safe stall characteristics. The spanwise lift distributions at various flight speeds serve as critical requirements for shaping the airfoil design.

Within the context of the HAP's typical operating envelope, the airfoil sections of the main wing generate lift coefficients ranging from 0.6 to 0.9. These coefficients extend further, reaching up to 1.6 at high-altitude stall speeds and dipping down to 0.2 at dive speeds. The holistic approach to aerodynamic wing design extends beyond lift and drag considerations to address structural constraints.

Achieving a soft stall is not merely a matter of aerodynamics; it involves a detailed analysis of spanwise lift distributions at higher angles of attack and the adaptation of airfoil sections to ensure a

stall occurs first on the inboard wing, minimizing the risks of stall-induced rolls or spins. Transitioning to the initial design phase, flexibility becomes a focal point. The absence of a complete structure and mass model is compensated by considering the effects of flexibility across various design speeds. Four different shapes, generated based on preliminary aeroelastic analysis, usher in a new dimension to the aerodynamic database, encompassing static, dynamic, control surface, and ground proximity derivatives for the deformed yet rigid aircraft.

In tandem with the intricacies of aerodynamic design, a dedicated effort is directed towards the propellers essential for the HAP aircraft. The propellers must deliver consistent thrust across the altitude envelope, exhibiting low power and rpm at low altitudes and high power and rpm at high altitudes. The design process, rooted in an inverse design method aligned with the theory of minimum loss propellers, unfolds through the blade element method. The resulting propeller design encapsulates a delicate compromise between propeller efficiency and motor mass, crucial for climb performance at low altitudes. The comprehensive analysis of mission points and the determination of structural loads contribute to the intricate engineering involved, showcasing characteristics in the form of power and thrust coefficients vs. advance ratio.

2.2.2 Structure

The preliminary structural sizing process for the HAP aircraft involves determining masses, stiffnesses, and moments of inertia of primary structural elements using an algorithm based on analytical methods. A beam model of the aircraft is generated, encompassing wing segments, longerons (fuselage, pylons), and tail segments. Wing and tail ribs, along with frame positions of the longerons, define control points for calculating section loads and exchanging them with aeroelastic load cases. Mass calculation employs Bernoulli beam theory for main structural elements, and other components are scaled volumetrically or two-dimensionally. The main structural element for wing spars and longerons is a tubular beam, chosen for low wing loading and manufacturing considerations. Sizing criteria include material strength, stability, torsional, and bending stiffness, with tube thickness, diameter, rib or frame distance, and material parameters as dimensioning parameters. The design process involves iterative cycles between load calculation and structural sizing, beginning with an initial structural design and progressing through multiple load and sizing loops.

2.2.3 Aeroelasticity

The aeroelastic modelling of the HAP structure, shown in figure 2.3 employs a finite elements model with beam elements, closely mirroring the actual structural design. Beam elements, discretized at every rib station along the wing, represent the long and slender structure accurately. The model includes leading and trailing edges connected to the main spar with rigid body links. Structural masses are derived from material thickness and density, while non-structural masses encompass solar generators, battery packs,

and engines. Torsional eigenmodes and eigenfrequencies receive special attention, modelling mass and inertia properties as condensed masses attached to structural grid points.
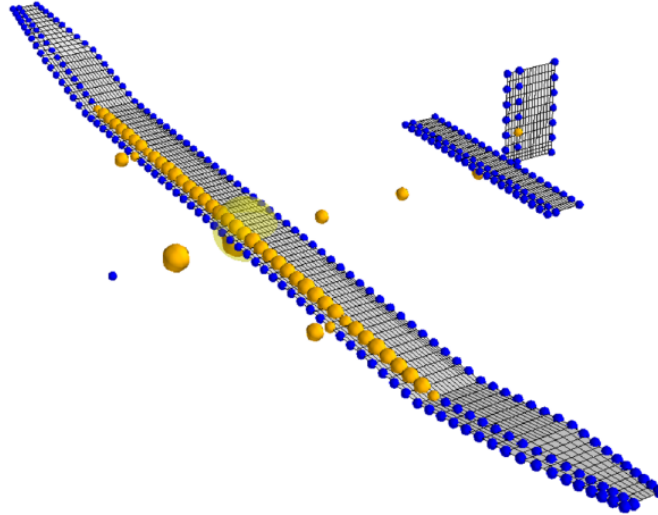
Figure 2.3: Structural discretisation (blue), condensed masses (yellow) and aerodynamic panel mesh of the aeroelastic model citepaperintro

Within the subsonic regime of flight speed, panel methods like the steady Vortex Lattice Method yield an acceptable representation of lifting surfaces. A transformation matrix couples displacements of the structural and aerodynamic grids to evaluate the impact of aerodynamic forces on the structure. Forces and moments transfer accordingly. Aeroelastic analyses include comprehensive loads analysis, considering manoeuvre, dynamic gust, landing, and gyroscopic loads. Section loads from this analysis inform structural sizing, leading to an iterative process of load analysis and sizing for convergence.

Once convergence is achieved, aerodynamic specialists define the desired flight shape for optimal cruise conditions, with a principal interest in wing twists for a favourable lift distribution. Elastic deformations require adjustments to the jig shape to match the flight shape. Wing flexibility influences lateral stability analyses due to elastic wing bending contributing to geometrical dihedral. The elastic behaviour of the empennage and fuselage induces a shift in the aerodynamic centre, impacting longitudinal stability. Evaluating aeroelastic control surface effectiveness becomes crucial for controllability and manoeuvrability.

2.3 Current configuration

A sketch of the current configuration of the vehicle is shown in figure 2.4, with a list of specifications and features resulting from the various trade-offs performed during the development phase.

The key parameters of the HAP so far developed are listed in the table 2.1. Even if the role of the DLR HAP is to obtain, generate and publish research about this aircraft type, a comparison with already
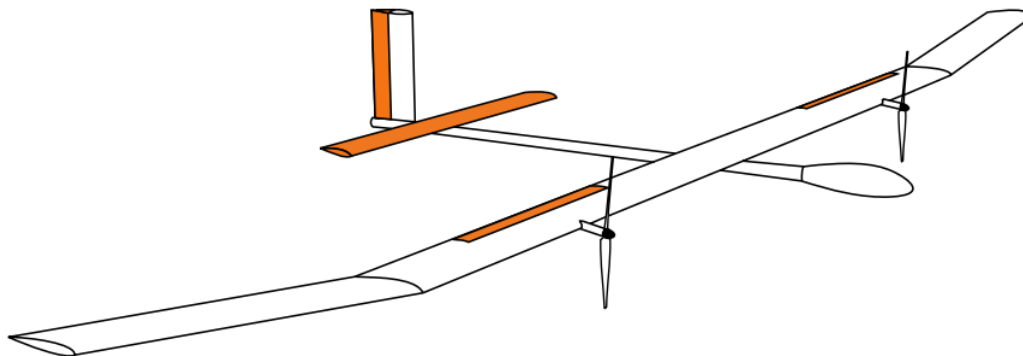
Figure 2.4: Sketch of the DLR HAP aircraft [16]

existing alternatives can be made to draw up some more insights.

Table 2.1: Key parameters of the DLR HAP aircraft

Parameter	Specification	Value
Wing area		36 m^2
Wing span		27 m
Dihedral	Inner wing	0°
	Outer wing	12°
Sweep		0°
Total mass		140 kg
Mass moments of inertia	I_x	3600 kg m^2
	I_y	620 kg m^2
	I_z	4200 kg m^2
	I_{xy}	15 kg m^2

The example model is the Airbus Zephyr S, based on the information in [13]. Despite similar wing spans and aspect ratios, the DLR HAP has a significantly higher total mass and wing loading than the Zephyr S. The differences in mass are attributed to the use of possibly more expensive components and a focus on risk mitigation in the DLR HAP design. The DLR HAP's conventional tail and ailerons contribute to its weight penalty. Additionally, the DLR HAP is suggested to have a more conservative structural sizing for increased structural stability [17].

2.3.1 Skids and landing

A special mention goes to the skids of the HAP, as they play a central role in both the literature research and the actual simulation process of this thesis.

For the case of the DLR HAP aircraft, two crucial factors increase the level of complexity of the landing procedure, other than the ones already mentioned in section 1.1. Firstly, the total mass of around 140 kg imposes the necessity of landing gear, making a hand collection of the aircraft impossible.

Then, since a retractable gear would lead to an excessive weight penalty, small non-retractable skids are used as landing gear, which cause only a little additional drag but bring some risks associated with the landing, like high landing loads and rollovers, as highlighted in [15].

This situation adds to the already poor ground clearance, which makes a go-around impossible, and therefore draws attention to the fact that the skids must be carefully designed and positioned. In addition, the analysis of the loads they receive during the landing is also of paramount importance in terms of the actual feasibility of the landing.

Regarding the configuration, the HAP aircraft is equipped with four (plus the payload compartment) non-retractable skids that are used as landing gear, shown below in figure 2.5.
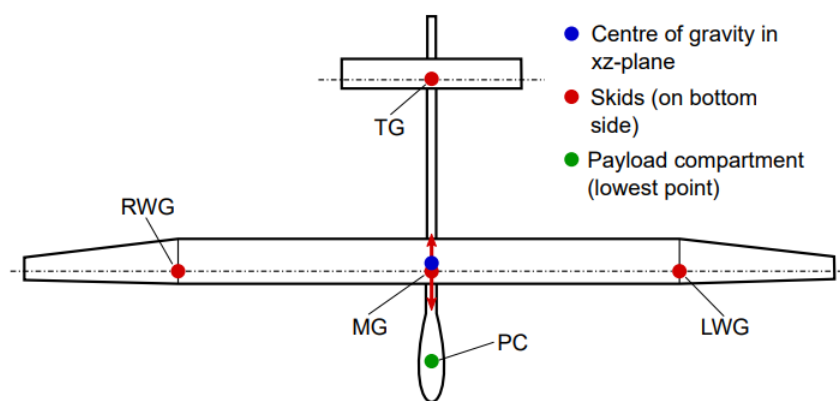
Figure 2.5: Top view of HAP aircraft and skid positions [15]

The skids are here referred to as MG (Main Gear), TG (Tail Gear), LWG (Left Wing Gear), RWG (Right Wing Gear) and PC (Payload Compartment). They also play a central role in the definition of the landing sequence. In fact, in contrast to the typical landing procedure for tail dragger aircraft, which often touches down with the rear gear first to achieve a higher angle of attack, in the DLR HAP the main skid touches down first.

A further complication is constituted by the need to ensure that the payload compartment, containing sensitive instruments, never touches the ground, and the allowable pitch range at touchdown is then defined and set to range from $-3°$ to $1°$, as shown in figure 2.6.
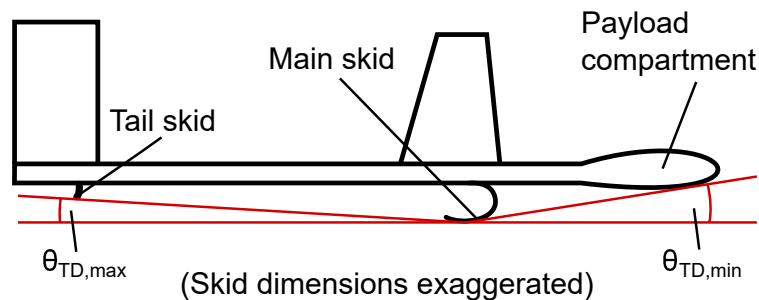
Figure 2.6: Side view of HAP aircraft and approximate allowable pitch angles at touchdown [15]

To summarise, the previous considerations highlight how complex and challenging the landing can be, and this is the main reason for the need for an extended study of this topic. The final goal is to have a more detailed and precise characterisation of the expected behaviour of the HAP demonstrator in the landing phase, considering many different external disturbances (like the wind conditions) and the terrain properties, as discussed in the literature research.

Chapter 3

Flight dynamic model

The flight dynamic model of the HAP is based on a classical non-linear six-degrees-of-freedom (6DOF) dynamic model, also used for highly accurate simulator models meeting Level-D simulator certification criteria. The translational motion expressed for a thrust vector aligned with the body axes and including the forces due to the skids is:

$$
\begin{cases}
\dot{u}_K = rv_K - qw_K + \frac{\overline{q}S}{m}C_X - g\sin(\Theta) + \frac{T}{m} + \sum_i^N \frac{R_{x,skid,i}}{m} \\[2mm]
\dot{v}_K = pw_K - ru_K + \frac{\overline{q}S}{m}C_Y + g\cos(\Theta)\sin(\Phi) + \sum_i^N \frac{R_{y,skid,i}}{m} \\[2mm]
\dot{w}_K = qu_K - pv_K + \frac{\overline{q}S}{m}C_Z + g\cos(\Theta)\cos(\Phi) + \sum_i^N \frac{R_{z,skid,i}}{m}
\end{cases}
\tag{3.1}
$$

Where the flight path velocities (labelled as Kinetic) are the sum of the air path ones (aerodynamics) and the wind ones ($\mathbf{V}_K = \mathbf{V}_A + \mathbf{V}_W$), while the rotational motion in a symmetric condition around the xz-plane is expressed by:

$$
\begin{cases}
\dot{p}I_x - \dot{r}I_{xz} = \overline{q}SsC_l - qr(I_z - I_y) + pqI_{xz} + \sum_i^N M_{x,skids,i} \\[2mm]
\dot{q}I_y = \overline{q}S\overline{c}C_m - pr(I_x - I_z) - (p^2 - r^2)I_{xz} + \sum_i^N M_{y,skids,i} \\[2mm]
\dot{r}I_z - \dot{p}I_{xz} = \overline{q}SsC_n - pq(I_y - I_x) + qrI_{xz} + \sum_i^N M_{z,skids,i}
\end{cases}
\tag{3.2}
$$

3.1 Longitudinal dynamics

The aerodynamics of longitudinal motion are modelled using a two-point model, allowing separate consideration of the main wing and horizontal tail plane (HTP) aerodynamics. The model accounts for the lag effect of wing downwash and different passing times of oncoming longitudinal and vertical wind components at the HTP. The lift coefficient is decomposed into a wing-body (WB) component and a

component for the horizontal tail (HTP), calculated as:

$$
\begin{cases}
C_{L_{WB}} = C_{L0_{WB}} + C_{L\alpha_{WB}}\alpha + C_{Lq_{WB}}q^* \\
C_{L_{HTP}} = C_{L0_{HTP}} + C_{L\alpha_{HTP}}\alpha_{HTP}k_{HTP,eff}
\end{cases}
\tag{3.3}
$$

Where $q^* = \frac{q\bar{c}}{V_{TAS}}$, giving a final lift coefficient of:

$$
C_L = C_{L_{WB}} + C_{L_{HTP}}\frac{S_{HTP}}{S}cos(\alpha_{dyn} - \epsilon_{HTP} + \Delta\alpha_{W_{HTP}})
\tag{3.4}
$$

With:

$$
\begin{cases}
\Delta\alpha_{W_{HTP}} = \alpha_{W_{HTP}} - \alpha_W \\
\alpha_{W_{HTP}} = \alpha_W(1 - \tau) \\
\tau = \frac{\chi_{HTP}}{V_{TAS}}
\end{cases}
\tag{3.5}
$$

In the C_L expression, $\Delta\alpha_{W_{HTP}}$ is the difference of the angles of attack due to wind between the HTP and the wing, $\alpha_{W_{HTP}}$ is the delayed wind component at the HTP, α_W is the wind component applied to the aircraft wing and τ is the time delay until a fluid element reaches the HTP after passing the wing.

The same structure is adopted for the pitching moment coefficient, divided into wing body components:

$$
\begin{cases}
C_{X_{WB}} = C_{L_{WB}}\sin(\alpha) \\
C_{Z_{WB}} = -C_{L_{WB}}\cos(\alpha)
\end{cases}
\tag{3.6}
$$

and the HTP components:

$$
\begin{cases}
C_{X_{HTP}} = C_{L_{WB}}\sin(\alpha_{HTP}) \\
C_{Z_{HTP}} = -C_{L_{HTP}}\cos(\alpha_{HTP})
\end{cases}
\tag{3.7}
$$

The two components, give the final pitching moment coefficient, expressed as:

$$
C_m = C_{m0_{WB}} + C_{Z_{WB}}\frac{x'_{WB}}{\bar{c}} - C_{X_{WB}}\frac{z'_{WB}}{\bar{c}} + C_{Z_{HTP}}\frac{S_{HTP}}{S}\frac{x'_{HTP}}{\bar{c}} - C_{X_{HTP}}\frac{S_{HTP}}{S}\frac{z'_{HTP}}{\bar{c}}
\tag{3.8}
$$

At the HTP, the angle of attack is:

$$
\begin{cases}
\alpha_{HTP} = \alpha + i_{HTP} + \alpha_{dyn} - \epsilon_{HTP} + \Delta\alpha_{W_{HTP}} \\
\alpha_{dyn} = tan^{-1}\left(q\frac{x'_{HTP}}{V_{TAS}}\right) \\
\epsilon_{HTP} = \epsilon_{0_{HTP}} + \frac{\partial\epsilon}{\partial\alpha}\alpha(t - \tau)
\end{cases}
\tag{3.9}
$$

The downwash angle ϵ_{HTP} describes the influence of the wing on the tail. The control surface effectiveness of the HTP due to flexible deformation as a result of a change in angle of attack or stabiliser input is

represented by $k_{HTP,eff}$.

Referring to the polar equation (3.10) and combining it with the lift coefficient, the force coefficients result as equations (3.11):

$$C_D = C_{D0} + \frac{C_L^2}{e\pi\Lambda} \tag{3.10}$$

$$\begin{cases} C_X = -C_D \cos(\alpha) + C_L \sin(\alpha) \\ C_Z = -C_D \sin(\alpha) - C_L \cos(\alpha) \end{cases} \tag{3.11}$$

3.2   Lateral-directional dynamics

Concerning the lateral dynamics, the coefficient for the lateral force, the rolling moment and the yawing moment are:

$$\begin{cases} C_Y = C_{Y_\beta}\beta + C_{Y_p}p^* + C_{Y_r}r^* + C_{Y_\zeta}\zeta \cdot k_{\zeta,eff} \\ C_l = C_{l_\beta}\beta + C_{l_p}p^* + C_{l_r}r^* + C_{l_\xi}\hat{\xi}k_{\xi,eff} + C_{l_\zeta}\zeta k_{\zeta,eff} \\ C_n = C_{n_\beta}\beta + C_{n_p}p^* + C_{n_r}r^* + C_{n_\zeta}\zeta k_{\zeta,eff} + C_{n_\xi}\hat{\xi}k_{\xi,eff} \end{cases} \tag{3.12}$$

Here, the combined aileron deflection is $\hat{\zeta} = \frac{1}{2}(\zeta_r - \zeta_l)$, while the dimensionless roll and yaw rate are the following, with s as the semi-span:

$$\begin{cases} p^* = \frac{ps}{V_{TAS}} \\ r^* = \frac{rs}{V_{TAS}} \\ s = \frac{b}{2} \end{cases} \tag{3.13}$$

The flexible deformations of the aileron and rudder are taken into account by the two coefficients $k_{\xi,eff}$ and $k_{\zeta,eff}$.

3.3   Flexibility

It is important to remark on the fact that the entire flight mechanical model is made up of a derivative-based aerodynamic model and a quasistatic dynamic pressure-dependent approach to account for flexibility effects due to the flight shape

This means that, instead of using the complete structural dynamics, the aerodynamic derivatives are given for different equivalent airspeeds, and then interpolation is performed between them to account for a quasistatic change in flight shape and its influence on aerodynamics.

As subsequently discussed in [16], the approach simulation approach is able to capture reactions to wind or control inputs, but it doesn't consider changes in flight shape due to rotational rates or varying load factors, nor does it address cross-coupling effects between aircraft structural dynamics and aerodynamics. In the context of the simulator environment, the interaction between the pilot, aircraft

aerodynamics, and structural dynamics cannot be accurately reproduced, leading to an inability to assess risks like pilot-induced oscillations driven by flexible dynamics. However, it does allow for the assessment of effects such as adverse aerodynamic properties or insufficient control authorities due to high airspeed excursions.

3.4 Stall models

As presented in [16], two stall models are included, one for the wind and one for the VTP.

3.4.1 Wing stall model

Wing stall is modelled using an approach that considers the flow separation point at the main wing due to the angle of attack, taking the reference from [11]. the angle of attack-dependent portion of the wing-body (WB) lift coefficient is reduced by a factor that represents the degree of flow separation:

$$(C_{L_{WB}})_\alpha = C_{L\alpha_{WB}} \cdot \alpha \cdot \left(\frac{1 + \sqrt{X}}{2} \right)^2 \tag{3.14}$$

Here, X is the non-dimensional separation point, ranging from 0 to 1 and modelled as:

$$X = \frac{1}{2} \cdot [1 - \tanh(C_1 \cdot (\alpha - \tau\dot{\alpha} - \alpha^*))] \tag{3.15}$$

where C_1 is a coefficient, τ is a time constant and α^* is the angle of attack at which the flow separation function has its turning point.

3.4.2 VTP stall model

For this part, the previous model coming from [15] was updated to also take into account the stall effects of the VTP. The new version of the equations is taken from [16] and considers the VTP side force curves for different rudder deflections ζ. It computes the VTP side force with the local side-slip angle β_{VTP}, and it has a negligible effect on the rolling motions due to the small lever arm of the VTP, so the (two) final equations are:

$$\begin{cases} C_Y = C_{Y_{WB}} + \cos(\beta_{VTP}) \cdot C_{Y_{VTP}}(\beta_{VTP}, \zeta) \cdot \frac{S_{VTP}}{S} \\ C_n = C_{n_{WB}} + \cos(\beta_{VTP}) \cdot C_{Y_{VTP}}(\beta_{VTP}, \zeta) \cdot \frac{S_{VTP}}{S} \cdot r_{VTP} \end{cases} \tag{3.16}$$

Where r_{VTP} is the horizontal VTP lever arm, S is the wing area and S_{VTP} is the VTP area and the VTP sideslip angle is:

$$\beta_{VTP} = \beta - \beta_W + \beta_{W_{VTP}} + \beta_{dyn} + \beta_{SW} \tag{3.17}$$

Here, β_W is the main wing sideslip angle due to wind, $\beta_{W_{VTP}}$ is the sideslip angle at the VTP due to wind and β_{dyn} is the dynamic sideslip angle at the VTP caused by a yawing motion. For the HAP aircraft, the sidewash angle is neglectable and thus $\beta_{SW} \approx 0°$. Note that the stall models can be switched on and off arbitrarily. If the stall model is switched on, equation (3.16) replaces the equations for yawing moment and side force from (3.12).

3.5 Ground effect model

The ground effect (GE) model, is described in [15], only taking care of the longitudinal motion. Thus, the ground impact factors are defined as:

$$
\begin{cases}
\sigma_1 = 1 - \tanh\left(a_1 \cdot \frac{h_{WB_{AGL}}}{b}\right) \\
\sigma_{1,HTP} = 1 - \tanh\left(a_1 \cdot \frac{h_{HTP_{AGL}}}{b_{HTP}}\right) \\
\sigma_2 = 1 - \tanh\left(a_2 \cdot \frac{h_{WB_{AGL}}}{b}\right)
\end{cases}
\tag{3.18}
$$

In this context, a_1 and a_2 are modelling coefficients and b is the wingspan. Then, $h_{WB_{AGL}}$ and $h_{HTP_{AGL}}$ represent the altitude above ground of the wing neutral point, respectively the HTP neutral point.

The effects on the WB and HTP lift coefficients are modelled as:

$$
\begin{cases}
C_{L_{WB}} = C_{L_{WB,base}} + C_{L\alpha_{WB,GE}} \cdot \sigma_1 \cdot \alpha \\
C_{L_{HTP}} = C_{L_{HTP,base}} + C_{L\alpha_{HTP,GE}} \cdot \sigma_{1,HTP} \cdot \alpha_{HTP}
\end{cases}
\tag{3.19}
$$

For the decrease in the induced drag, the corrective term is integrated into the model by:

$$
C_D = C_{D_{base}} - \sigma_1 \cdot \frac{C_L^2}{e\pi\Lambda}
\tag{3.20}
$$

Additionally, the attenuation of the main wing downwash at the HTP and the pitching moment coefficient are corrected by:

$$
\epsilon_{HTP} = \epsilon_{HTP_{base}} + \left(\frac{\partial\epsilon_{HTP}}{\partial\alpha}\right)_{GE} \cdot \sigma_2 \cdot \alpha(t-\tau)
\tag{3.21}
$$

$$
C_m = C_{m_{base}} + \sigma_1 \cdot C_{m0_{GE}}
\tag{3.22}
$$

3.6 Skid model

As previously discussed, the skids are the main character of the landing context, and so their mathematical model is briefly outlined.

All four skids have uniform viscoelastic properties, including stiffness and damping. A control point at the payload compartment, also modelled with the same means as the skids, is designated to detect ground contact, and any such contact is considered unacceptable for landing. The skids are represented using standard linear solids (SLS), with the skid reference point defined as the lowest point assuming no inclination or uneven ground. Dynamic equations for these systems are well-documented [3], and figure 3.1 shows the Kelvin-Voigt representation.
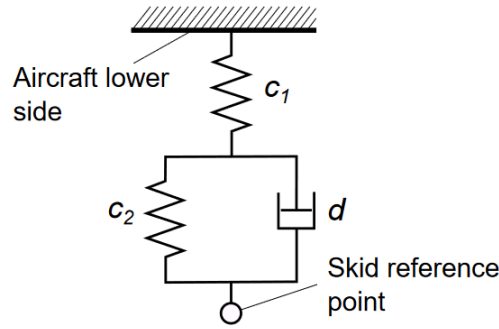
Figure 3.1: Skid modelled as standard linear solid in Kelvin-Voigt representation [15]

The vertical force exerted depends on the skid compression and vertical velocity when in contact with the ground. The model is expressed as:

$$
R_{z,g_{Skid}} =
\begin{cases}
\int \dot{R}_{z,g_{Skid}} \, dt = \int \left(\dot{h}_{AGL_{Skid}} \cdot c_1 + h_{AGL_{Skid}} \frac{c_1 \cdot c_2}{d} - R_{z,g_{Skid}} \frac{c_1 + c_2}{d} \right) dt & : h_{AGL_{Skid}} < 0 \ m \\
0 & : h_{AGL_{Skid}} \geq 0 \ m
\end{cases}
$$

$$(3.23)$$

Here, $h_{AGL_{Skid}}$ is the altitude above ground of the skid reference point of the respective skid, which considers the effect of the elastic deformation of the aircraft, while the spring constants c_1 and c_2, and the damper constant d are expressed in table 3.1.

Table 3.1: Skid model parameters

Parameter	Value	Unit
$c_1 = c_2$	40000	N/m
d	500	Ns/m

In conclusion, the final forces along the three axes result as:

$$
\begin{cases}
R_{x,b_{Skid}} = \mu \cdot sign(u_{K,b_{Skid}})R_{z,g_{Skid}}\cos(\Theta) - R_{z,g_{Skid}}\sin(\Theta) \\[2mm]
R_{y,b_{Skid}} = \mu \cdot sign(u_{K,b_{Skid}})R_{z,g_{Skid}}\sin(\Phi)\sin(\Theta) - \mu_S \cdot sign(\tau_S)R_{z,g_{Skid}}\cos(\Phi) \\[2mm]
\quad + R_{z,g_{Skid}}\sin(\Phi)\cos(\Theta) \\[2mm]
R_{z,b_{Skid}} = \mu \cdot sign(u_{K,b_{Skid}})R_{z,g_{Skid}}\cos(\Phi)\sin(\Theta) + \mu_S \cdot sign(\tau_S)R_{z,g_{Skid}}\sin(\Phi) \\[2mm]
\quad + R_{z,g_{Skid}}\cos(\Phi)\cos(\Theta)
\end{cases}
\tag{3.24}
$$

Here, τ_S is the skid crab angle, assumed the same for all the skids, and equivalent to:

$$
\tau_S = -arctan\left(\frac{\nu_{K,b_{Skid}}}{u_{K,b_{Skid}}}\right)
\tag{3.25}
$$

At the time of the paper, the model was completed with a kinetic friction coefficient of $\mu = 0.4$, while the lateral friction coefficient was assumed to be $\mu_S = 0.55$. The first part of the literature research deals with this topic, aiming to define a more accurate value for this latter friction coefficient and also taking other factors into account like the weight-dependent ground penetration.

In this work, rectangular skid shapes with a length of $l = 0.15$ m and a width of $b = 0.075$ m are assumed when calculating the friction coefficients.

Chapter 4

Literature research

This literature research aims to deepen several fields of interest, in order to achieve a better understanding of certain not fully explored topics, such as the lateral friction coefficient developed by the skids when the aircraft is on softer ground e.g. grass and the skids are supposed to penetrate the ground to a certain extent.

Then, this chapter will be divided into sections, and each of them will focus on its specific literature research, from the scientific revision of the current state of the art to the actual assumed adaptations for this specific purpose. The latter one is a specifically crucial part of the work since the overall project is pretty avant-garde, and so not always something in the literature was found.

4.1 Skid lateral friction force

The first part of the literature research deals with the estimation of the skid's lateral friction coefficient.

4.1.1 Current model

The current version of the model assumes a constant friction coefficient, particularly $\mu = 0.4$ for the longitudinal and $\mu_S = 0.55$ for the lateral motion. As stated in the previous works [15] this model was acceptable since the lateral direction only played a minor role in the evaluation of the overall landing capabilities. But, with the introduction of other factors, such as an intense crosswind and a crabbed landing, the model needs an update. It is important to remember that a crabbed landing is not always the consequence of crosswind since a vehicle could also just fly with a sideslip angle.

4.1.2 Different approaches

Even if some research was conducted on various aspects of tribology, not all of them take into account the shape of the moving object, especially in the aeronautical field. Also, if the topic includes any kind

of skid-equipped vehicles, the available material is reduced a lot. The most promising research was conducted in the fields of helicopters, re-entry space planes and skid-steering land vehicles.

Regarding the helicopters, the main focus is on the skid's kinetic/structural properties and the general ground dynamic model of the vehicle, designed for different types of landing ([28], [27] and [35]). In all of them, there is always accordance regarding the overall friction coefficient, expressed according to the formula used by Sareen, Smith and Howard [32], which is:

$$\mu = F_k + (F_s - F_k)e^{-\beta\nu} \tag{4.1}$$

where F_k is the kinetic friction coefficient, F_s is the static friction coefficient, β is the exponential decay coefficient, and ν is the relative velocity between the sliding components, here intended as the overall velocity of the helicopter. Even if this model is quite interesting for ground interaction modelling, it does not capture the differentiation between the longitudinal coefficient and the lateral one.

The second topic is one of the space planes, which were quite popular during the sixties and the seventies, thanks to many studies conducted in the United States. Both in the McDonnell Douglas Corp. report [10] and in the NASA one [34], the concepts were equipped with main gear skids and a single nose wheel. Even by considering the crosswind component during landing, mostly for the stability and steering control assessment, the friction coefficient was considered only within the longitudinal motion and then split according to the geometrical components, so it does not accurately match the purpose of this work.

The third approach is taken from the field of terramechanics, which can be described as the study of soil properties, specifically for the interaction of wheeled or tracked vehicles on various surfaces. This discipline has an interesting modelling regarding friction forces (both lateral and longitudinal) because they are really important in the dynamic of skid-equipped vehicles, such as tanks, agricultural machinery or even space rovers.
While Wismer and Luth [36] proposed the base for the empirical evaluation of the mechanical characteristics of a moving metal skid while sliding on a surface (usually off-road), Kitano and Kuma [20] (and also others [18], [6]) applied it to the plane motion of tracked vehicles, coming out with two different expressions for the lateral and longitudinal friction coefficients, namely:

$$\begin{cases} \mu_x = E_1(1 - e^{-E_2|S_j|}) \\ \mu_y = kE_1(e^{-E_2}) \end{cases} \tag{4.2}$$

where E_1 and E_2 are positive constants determined by the pull-slip test, S_j is the slip factor, and it is 1 in our case, while k is the anisotropic coefficient of friction, meaning that the isotropic is equal to 1. This approach is better working than the previous ones, but still, it does not consider the shape influence on the overall friction coefficient, and there is not much literature regarding the possible parameters for

the interested kind of ground surfaces (tarmac and grass). In conclusion, a similar work was taken into consideration and will be better exposed in the next section.

4.1.3 Proposed model

As already mentioned, the aim of this part of the work is the estimation of the lateral friction coefficient as a function of the landing terrain and the actual shape of the skid, assumed to have a rectangular area of contact. The idea is to have an expression of the total friction coefficient, which can, for example, be taken as longitudinal if the skid is pushed along a straight line, or lateral if it is pushed laterally, so directly by switching the two dimensions (b and l). This also allows to compute any intermediate situation (with a crabbed landing) just by combining the two different components.

Starting with the pressure-sinkage relation proposed by Bekker [4], which gives the relation between the deformation of the terrain due to pressure applied on it, it is possible to compute the work performed by the resistance force [37], also considering the shape of the skid, here rectangular.

$$p = \left(\frac{k_c}{b} + k_\phi \right) z^n \tag{4.3}$$

In the Bekker's equation (4.3), p is the pressure, which will hereafter be expressed as the weight W over the surface $(b \cdot l)$, z is the sinkage, while k_c, k_ϕ and n are parameters of the terrain, particularly, n is the exponent of terrain deformation, k_c is the frictional terrain modulus and k_ϕ is the cohesive terrain modulus.

The final equation for the overall resistance of a skid is the following (4.4):

$$R_c = \frac{b}{(n+1) \left(\frac{k_c}{b} + k_\phi \right)^{\frac{1}{n}}} \left(\frac{W}{bl} \right)^{\frac{n+1}{n}} \tag{4.4}$$

In order to evaluate the output of this model, a MATLAB script was written to compare the different combinations of each parameter of the equation. An already known value to refer to is 0.4, for the longitudinal friction coefficient on grass, so this has to be considered to adapt the following results and adjust the model's parameters.

Before presenting the results, a preliminary note on the W parameter, representing the mass bearing on the skid. It was set at 80 kg, which is derived from considerations regarding not only the weight sharing between the different skids, but also to account for the difference in lift and weight at touchdown.

Grass model

By looking at some examples of applications [37], the identified values for the equation's parameters for grass are:

Here, the skid dimensions are assumed to be equivalent to $l = 0.075$ m for the length and $b = 0.15$ m for

Table 4.1: Estimated parameters for grass

Parameters	n	k_c (kN/m^{n+1})	k_ϕ (kN/m^{n+2})
min	1.5	60	1800
max	2.5	90	2200

the width. The script can evaluate both the longitudinal and lateral friction coefficients just by switching the two dimensions, as a function of the three parameters that characterise it, as shown in figures 4.3, 4.4 and 4.5. In the following plots, only the longitudinal one is shown, but the results for the lateral one are equivalent.

The first two plots of figure 4.6 show how the length of the skid is way more influential than the width regarding the final friction coefficient value. It is due to say that, for the lateral coefficient, the most influential dimension will be the width, according to the switching of the two quantities under consideration.

Tarmac model

The same procedure was followed for the other type of ground, the asphalt, with the difference that the n exponent, which should represent the extent of the sinkage due to pressure, is meaningless in the sense that the asphalt could be assumed without any sinkage, so it should tend to a very high value.

The obtained values range within the ones in the table 4.2, while the correspondent results are shown in figure 4.9, 4.10 and 4.11.

Table 4.2: Estimated parameters for tarmac

Parameters	n	k_c (kN/m^{n+1})	k_ϕ (kN/m^{n+2})
min	14	170	5000
max	16	180	6000

As previously done, the first two plots of figure 4.12 show the same situation as the case of the grass, albeit with a decrease in the value of the friction coefficients, due to the use of different parameters to model the tarmac.

Overall results

To summarise the definitive parameters, the table 4.3 shows the chosen values for both terrains.

Table 4.3: Averaged estimated parameters

Parameters	n	k_c (kN/m^{n+1})	k_ϕ (kN/m^{n+2})
Grass	2.25	75	2000
Tarmac	15	175	5500
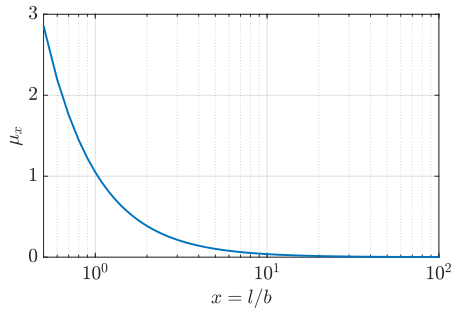
Figure 4.1: Grass friction coefficient with respect to the dimensions ratio $x = l/b$ for a fixed b
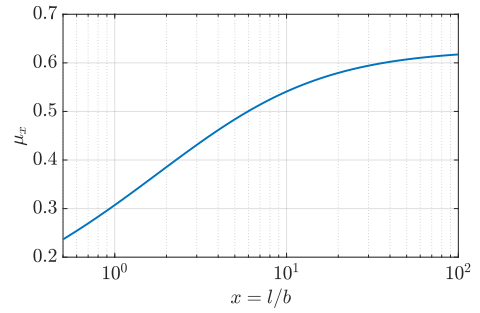
Figure 4.2: Grass friction coefficient with respect to the dimensions ratio $x = l/b$ for a fixed l
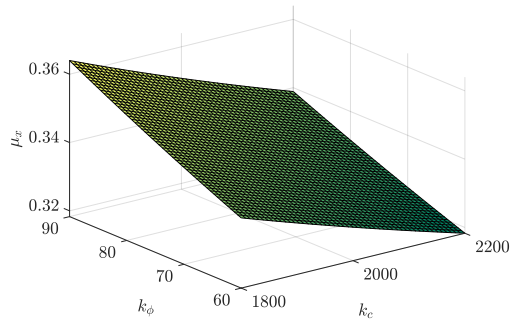
Figure 4.3: Grass friction coefficient with respect to k_c and k_ϕ
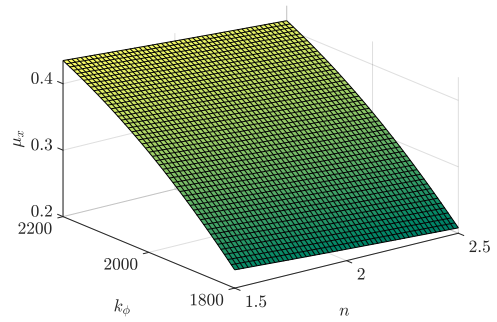
Figure 4.4: Grass friction coefficient with respect to n and k_ϕ
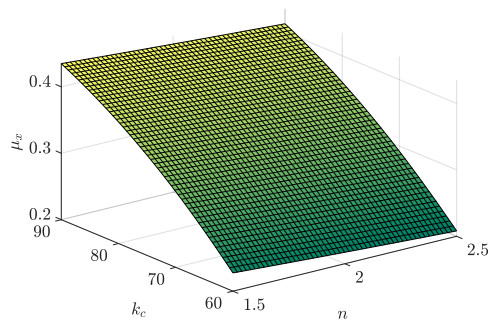
Figure 4.5: Grass friction coefficient with respect to n and k_c

Figure 4.6: Grass characteristic plots
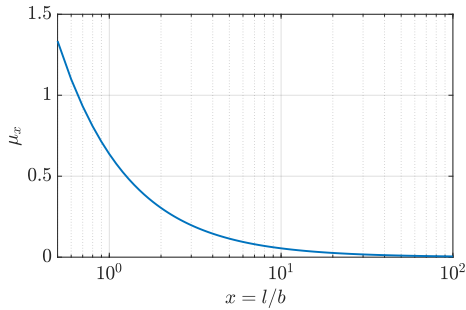
Figure 4.7: Tarmac friction coefficient with respect to the dimensions ratio $x = l/b$ for a fixed b
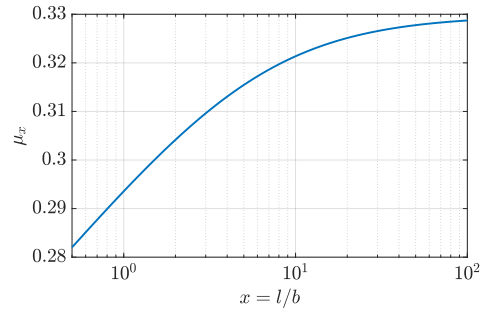
Figure 4.8: Tarmac friction coefficient with respect to the dimensions ratio $x = l/b$ for a fixed l
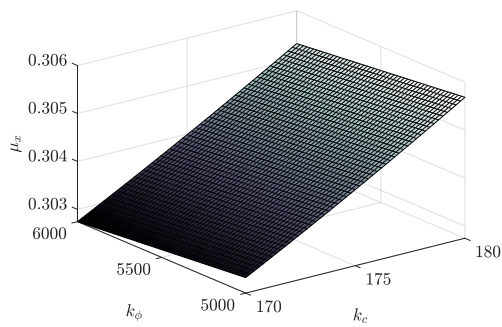
Figure 4.9: Tarmac friction coefficient with respect to k_c and k_ϕ
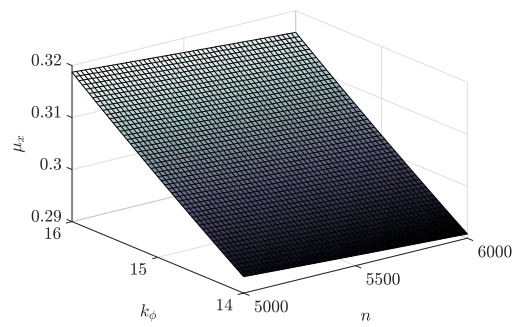
Figure 4.10: Tarmac friction coefficient with respect to n and k_ϕ
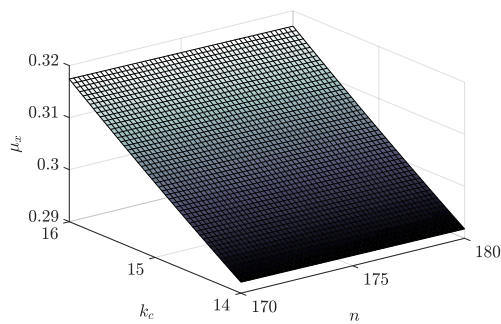
Figure 4.11: Tarmac friction coefficient with respect to n and k_c

Figure 4.12: Tarmac characteristic plots

By using these values, and by switching the dimensions for computing the lateral coefficient, the final results are shown in the table 4.4.

Table 4.4: Estimated friction coefficients

Terrain	μ_x	μ_y
Grass	0.3855	0.8361
Tarmac	0.3042	0.6149

Regarding the grass, the values seem reasonable, compared to the already existing one of 0.4 for the longitudinal friction coefficient. They have a ratio of almost 2.17, which is consistent with the skid's dimensions. The same is true for the tarmac, which shows a ratio of almost 2, while the single value is located within the usual value assumed for a longitudinal motion between steel and asphalt, which ranges from 0.2 to 0.5 [7]. Also, the values of the tarmac are smaller than the ones for grass, which is expected due to the different composition of these two terrains: while on the tarmac, it is easy to slide, on the grass there is a higher risk of sinking, and therefore to encounter greater resistance.

Drawbacks of the model

About the results obtained in table 4.4, some comments are necessary concerning the subsequent implications of this model.

In the case of grass, the values are generally acceptable and consistent with each other as already. The longitudinal value is very close to the already known 0.4.

On the other hand, in the case of tarmac, given that for a very rigid (ideally, infinitely rigid) terrain, sinkage should be almost nil or at least negligible, and therefore, the values of the coefficient of friction should differ less from each other, albeit consistent with the different skid dimensions. This suggests that the model in question may be less accurate for tarmac than it is for grass. Consequently, both for the reasons mentioned above and to pursue a conservative approach, only grass will be used in the first instance as the default terrain

4.2 Crosswind landing

The second part of the literature review is a summary of the different crosswind landing techniques, including their challenges and operational limits, with a short introduction to the safety issues related to them, and the final motivation for the choice used in this work.

4.2.1 Background and safety aspects

A crosswind landing indicates any final approach where the wind is blowing at an angle to the runway rather than parallel to the landing direction [1]. This condition is much more common than expected,

since almost all landings are crosswind landings [5], given that the air surrounding the plane is always in movement, which is not always just straight. Of course, not all of them are critical, but they become to be crucial from a certain magnitude and presence of the wind. This is different for each category of vehicle, and for the DLR HAP is of course smaller than a classical airliner, due to the evident differences in size and weight.

Regarding the safety aspects, the expression "aviation weather" is used to indicate "any type of weather that can affect the operation of an aircraft, anything from a brief delay in departure because of low visibility to a catastrophic accident during flight" [29]. This greatly impacts the landing procedures, as demonstrated in many technical documents. In fact, according to a report from the FSF (Flight Safety Foundation) [19] and as summarised in [21]:

- There were 287 fatal approach-and-landing accidents and 76 serious incidents (occurrences during 1984–1997).

- Adverse wind conditions (the presence of strong crosswinds, tailwinds and wind shear) are involved in one-third of approach-and-landing accidents.

- Two-thirds of the overruns or excursions occurred with at least two of the following weather factors: rain, fog and/or crosswind present.

- 85% of crosswind incidents and accidents occur at landing.

One of the leading causes of these excursions is a non-stabilized approach [9], as well as an excess of airspeed, early touchdown and other contingent runway conditions.

In addition to this, an analysis of the FAA's (Federal Aviation Administration) National Aviation Safety Data Analysis Center of Accident Investigations reported that [29] 42.6% of 5286 weather-related accidents were caused by wind/wind shear between the fiscal years 1987 and 1996, as shown in figure 4.13. Even if weather-related accidents involved 24% of all aviation accidents, 88% of them involved small private aircraft, clearly showing their higher exposure to adverse weather conditions.

As another example, the Royal Netherlands Aerospace Centre (NLR) reported [8] that weather is identified as a causal factor in about 10% of all accidents, and weather-related aviation accidents are most often caused by wind, according to the NLR Air Safety Database. All of those examples show the crucial importance of a secure and controlled landing, especially during crosswind conditions, in order to avoid any lack of safety, and to ensure the success of the mission.

4.2.2 Techniques

Concerning the airborne part of the overall landing, a crosswind landing aims to compensate the lateral wind component, assuming that the other flight properties are already stable, like the glide path angle and the aircraft ground speed vector lined up with the runway centreline. There are two possible techniques
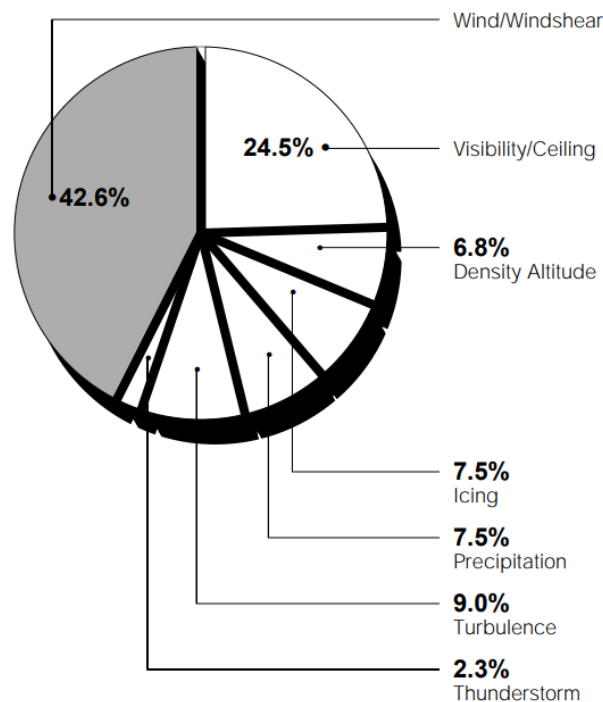
Figure 4.13: Incidence of weather factors in weather-related accidents [29]

for performing a crosswind airborne approach: the "crab" method and the wing-down/sideslip/low-wing method.

Crabbed approach

The first approach consists of heading towards the wind, trying to eliminate the sideslip angle β, in order to not drift out of lateral alignment of the ground path with the runway, and so keeping the track angle χ constant. So, the pilot has to turn the aircraft "into the wind" while continuing to track down the runway. The figure 4.14 shows the crabbed landing configuration, recommended by Airbus [33]. However, this landing also has some limitations/drawbacks, namely:

- The runway is seen from the side window, which results in an unnatural and disorienting condition for the pilot.

- Before landing, a de-crab is needed, requiring a combined rudder-aileron maneuver to prevent drifting on the runway.

- It is a good approach for big airliners, since the high inertia makes them straighten up fast, but not for small planes, because of the higher risk of jump and bounce, or even rollover if the alignment is not perfect.

The most important advantage, on the other hand, is that the plane is not banked when in this configuration (until the de-crab), so this maneuver is indicated for high aspect ratio wing vehicles.

41
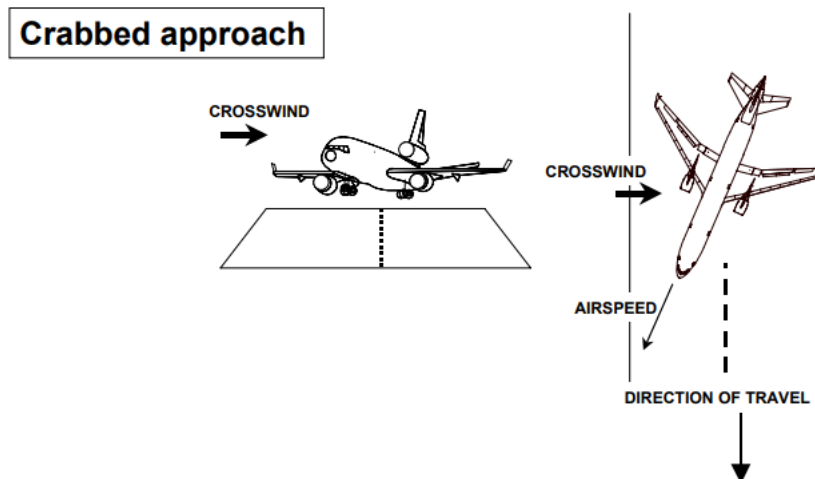
Figure 4.14: Crabbed approach for a crosswind landing [8]

Wing-down approach

This other technique suggests heading towards the runway. This way sideslip is established leading to a rolling and yawing moment and a side force. To counteract these, aileron inputs are applied to lower the upwind side of the wing. The resulting bank angle, together with aileron and opposite rudder inputs then counteract the forces and moments allowing a stationary approach. Figure 4.15 shows such an approach.

The positive aspects of this method are that it is a faster approach than the crabbed one, and directly allows to face the runway. On the other side, there is the necessity of an opposite control, so a counter-intuitive command and the bank angle can lead to a wing strike.
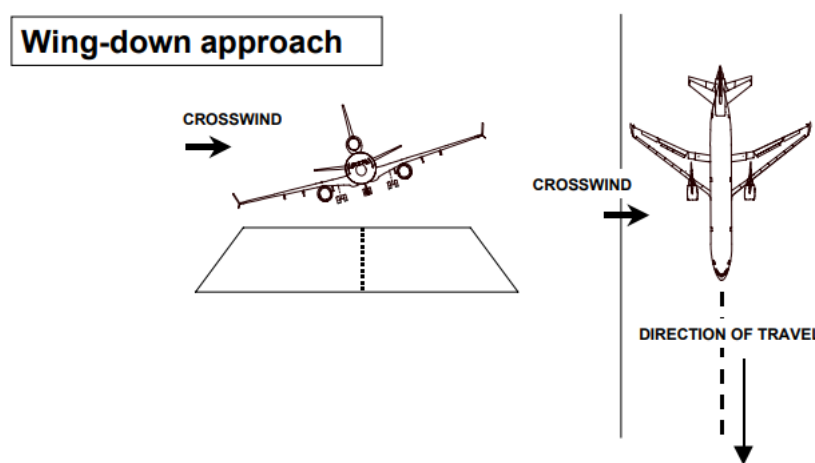
Figure 4.15: Wing-down approach for a crosswind landing [8]

4.2.3   Chosen approach technique

For the aim of this project, the landing procedure plays a crucial role. Some peculiar characteristics of the aircraft make a traditional landing particularly difficult, as already mentioned in chapter 2. In

addition to these, new challenges are posed by considering a crosswind landing, two in particular:

- There is not enough ground clearance during landing. This must be taken into account for several reasons, starting from the propellers, which need to be retracted before touchdown, and also for the limited sideslip range, in order to avoid any wing strike, due to the high aspect ratio of the wing.

- The vehicle is very sluggish and the highly coupled rolling and yawing motions are difficult to control. In the end, it is to be expected that a decrab manoeuvre is very difficult or even impossible to perform right before touchdown with this aircraft.

In the end, after considering these limitations, the most promising landing technique is the crabbed approach, but without any de-crab. This technique, which is not commonly used, is known e.g. from the Boeing B-52 Stratofortress.
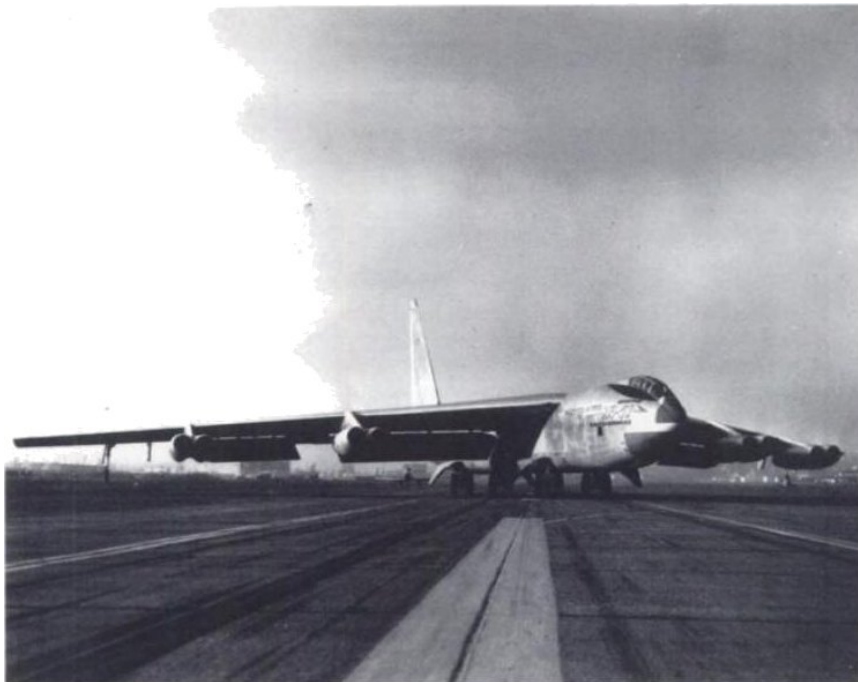
Figure 4.16: Crabbed landing of the Boeing B-52 (Source: Wikipedia)

This strategic bomber is famous for its possibility to pivot both the fore and aft main landing gear up to 20°. The choice was forced because of the low steering power of the rudder and allows landings even in strong crosswinds, as shown in figure 4.16.

Chapter 5

Implementation of the lateral controller

During the flight test campaign, the aircraft is remotely piloted due to the absence of a radar altimeter and the incremental activation of controllers. To accurately simulate landing maneuvers employing the complete six degrees of freedom (6DOF) model, the use of a controller becomes indispensable. Thus, within the scope of this study, the controller serves as a surrogate for a pilot, assuming a crucial role in executing flight operations with precision and fidelity.

It is important to state that the DLR HAP is a stable vehicle, so there is no need for a controller as it is meant in common sense. Instead, the usage of it is justified by the fact that the controller has the role of landing the aircraft in the context of the simulations, so it will behave as a guidance controller, and not for stabilisation.

This chapter will then deal with different aspects of the lateral controller, without considering the landing itself for now. An introductory section explains the input of the model, which is made up of a variable lateral wind. After this, various lateral controllers are presented and evaluated, based on their performances in terms of stability, settling time and robustness to variable inputs.

5.1 Purpose of the controller

The tasks of the controller can be summarised and pointed out as follows:

- **Sideslip-free condition**: through the specific heading into the wind direction, to let the following point.

- **Track maintaining**: to maintain lateral alignment with the runway and uphold the track angle, thereby preventing deviation from the intended ground path.

5.2   Wind input pattern for controller test

The idea is to test the robustness and the general functionality of the controller with a variable lateral wind input (which actually consists of a disturbance), consisting of 3 different components:

- Step input, from a specific time to the end.

- Different gusts, in accordance with the CS-25, adapted for this case.

- Ramp command.

The different inputs are shown all together in figure 5.1, with the total resulting value and its components. While the step is always fixed at a constant value, both the gusts and the ramps are variable, in terms of intensity, duration and slope (for the ramps). The resulting value is also designed to not heavily exceed for a long interval the value of 6 m/s, which is almost 2/3 of the longitudinal initial velocity set for the simulation.
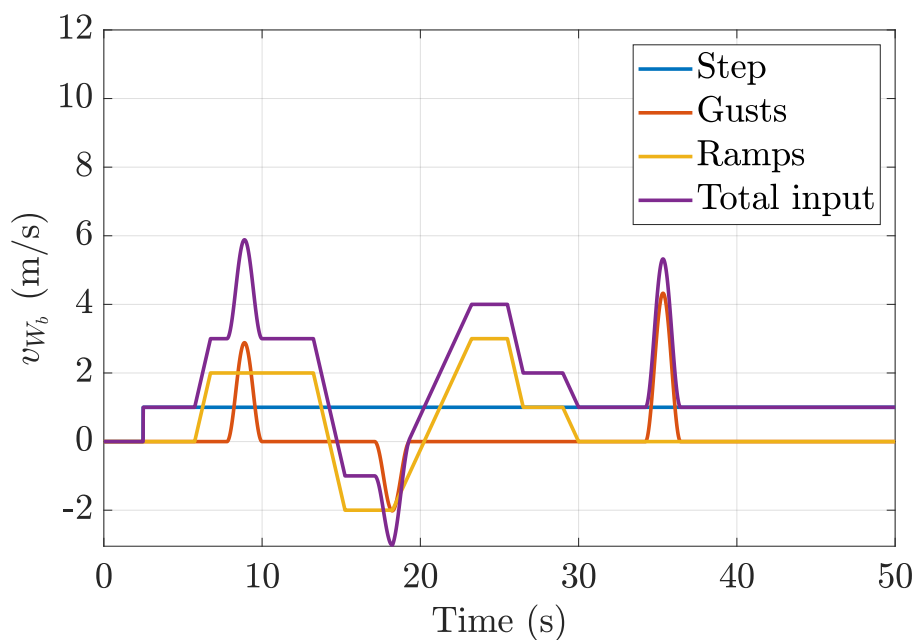
Figure 5.1: Total input

The resulting input is variable and diversified, so it excites the system both slowly and quickly, and in both directions of the lateral plane. This makes it possible to assess the robustness of the controller to various external disturbances. In addition, the final input will also present continuous turbulence, which is added as a basis for the entire simulation, shown in figure 5.2 (in the simulation timescale).
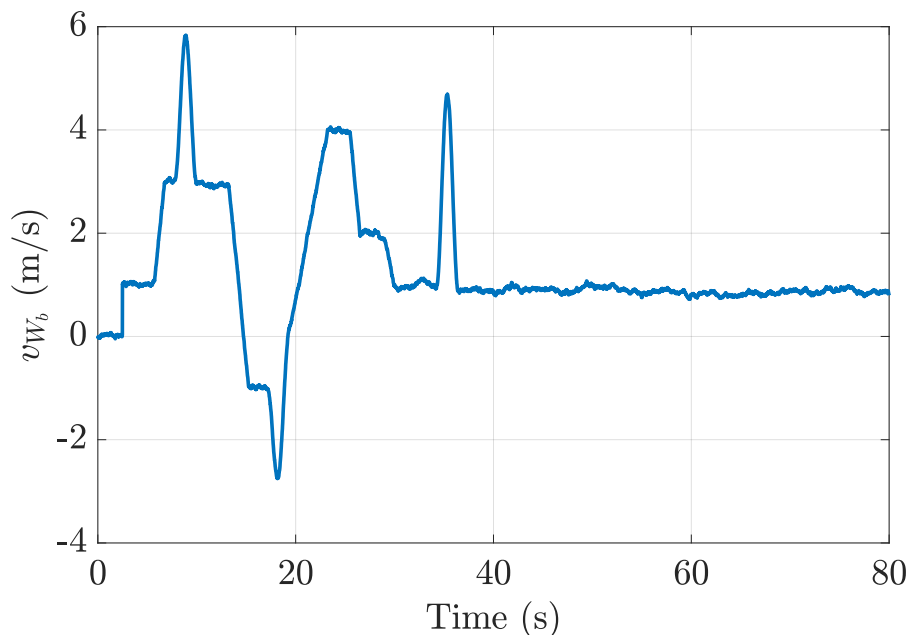
Figure 5.2: Total input with turbulence

5.3 Test task

This section deals with the preliminary evaluation of the involved variables, reference values and the controller assessment with respect to this initial test case. There are no classical requirements such as bandwidths and phase margin, but rather a simpler performance evaluation based on specific criteria explained further in this work.

About the current situation, some lateral controllers are being selected and tested, both to explore their capabilities and to ensure certain specifications are met. More specifically, a certain level of control is attended over some variables as stated in section 5.1, then a detailed explanation of them is provided in this section.

5.3.1 Sideslip angle

According to the ISO 1151-1 [12], the sideslip angle β indicates the angle which the aircraft velocity (belonging to the air-path axis system) makes with the reference plane of the aircraft. It is considered positive when the aircraft velocity component along the transverse axis is positive. The figure 5.3 is then showing a positive sideslip angle.

The β angle should reach a steady-state value of zero, meaning that no matter which is the direction of the oncoming flow, the nose of the vehicle has to point "into" it, in order to eliminate the sideslip itself. So, if the wind is coming from the left of the plane, it should yaw to the left until the sideslip is eliminated. Indeed, the HAP inherently shows this behaviour of reducing sideslip thanks to its weathercock stability. However, at low altitudes and low airspeeds, it takes quite a long time until a sideslip is eliminated by
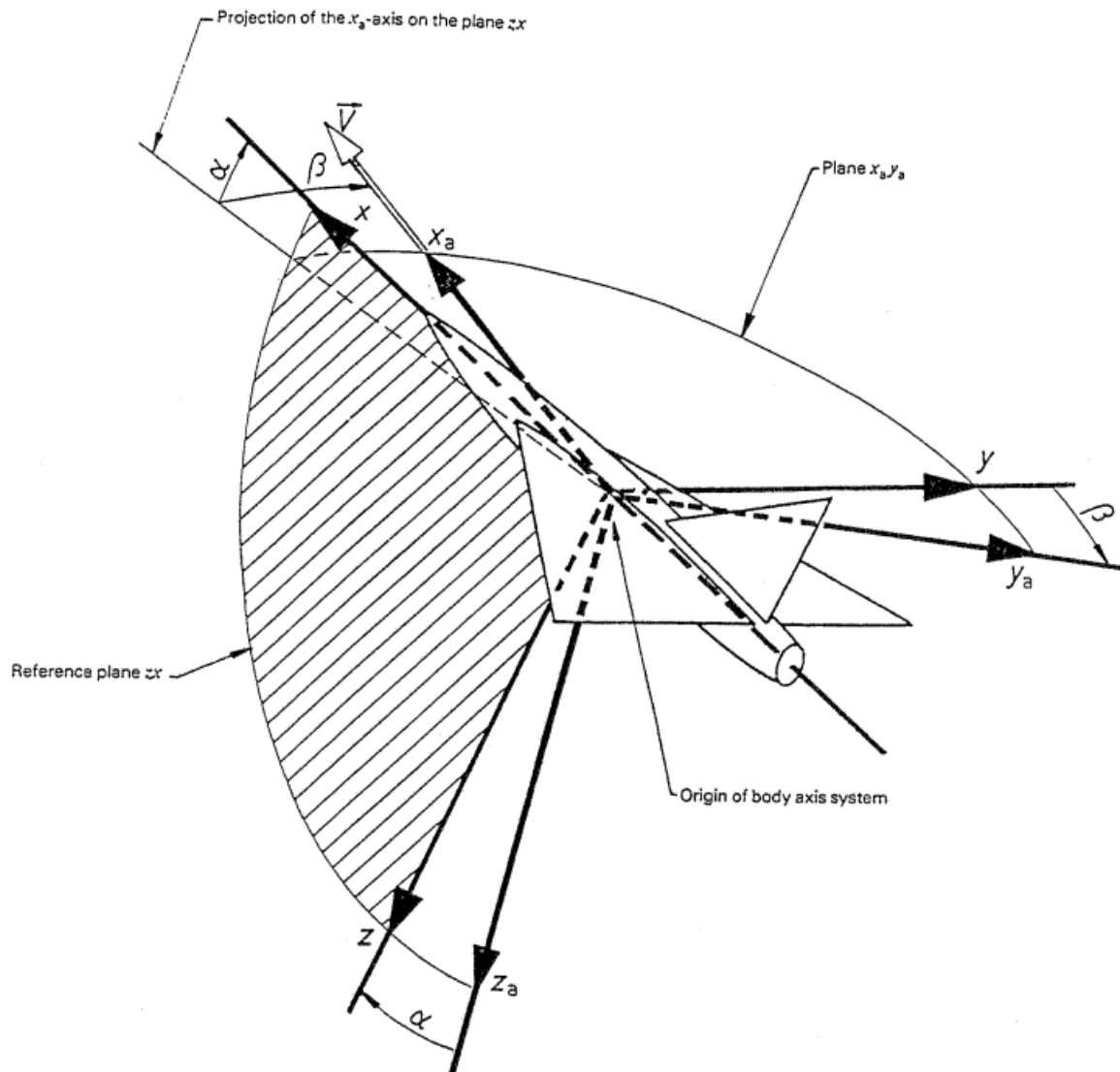
Figure 5.3: Sideslip angle visualisation [12]

the aircraft itself. Therefore, it is better to augment the sideslip angle stabilisation. In any case, one of the earlier versions of the controller was tried without β direct control, and it will be better explained in the next chapters.

Figure 5.3 shows the body axes system $(x - y - z)$, which are in this work represented by $(x_b - y_b - z_b)$, and the air-path axis system $(x_a - y_a - z_a)$.

5.3.2 Track angle

Similarly as done before, and by referring to the ISO standard [12], the track angle (more correctly the air-path azimuth/track angle) χ_a is defined as the rotation (positive, if clockwise) about the $z_o(z_g)$-axis which brings the $x_o(x_g)$-axis into coincidence with the projection of the air-path x_a-axis on the horizontal plane through the origin. In simpler words, it constitutes the angle between the axis $x_o(x_g)$ belonging

to the aircraft-carried normal earth axis system and the projection of the velocity vector laying in the horizontal plane $x_o y_o (x_g y_g)$.
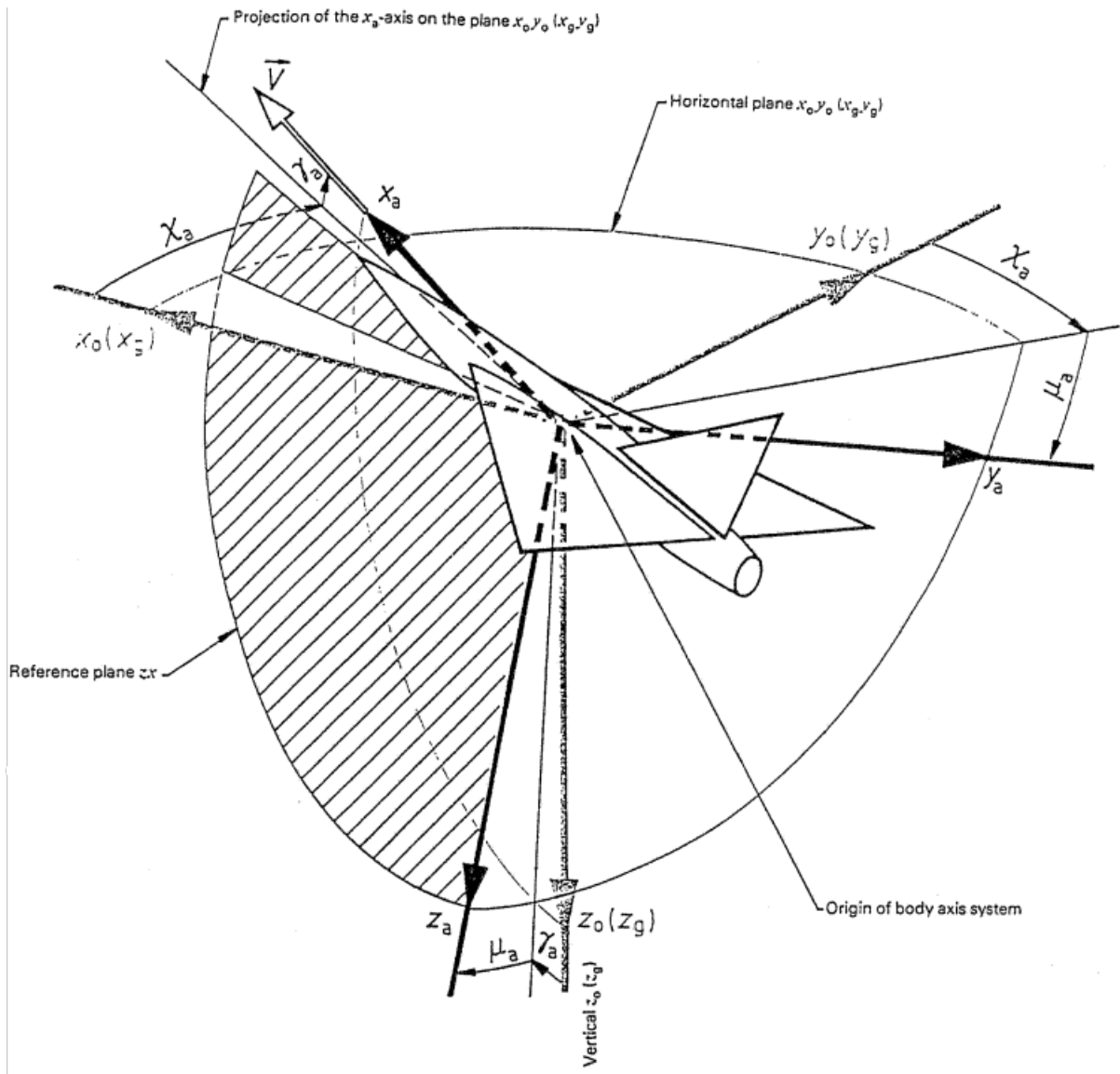
Figure 5.4: Track angle visualisation [12]

Figure 5.4 shows the aircraft-carried normal earth axis system $(x_o(x_g) - y_o(y_g) - z_o(z_g))$, and the air-path axis system $(x_a - y_a - z_a)$.

However, the track angle that is used in this work is not the air-path azimuth, but rather the inertial track angle χ_K, from now referred to as just χ for simplicity. It is not indicated in figure 5.4, but a clearer explanation comes from figure 5.5, where, the correct track angle is expressed as:

$$\chi_k = \chi = \angle(\overrightarrow{x}_{NED}, \overrightarrow{x'}_K) \tag{5.1}$$

The track angle is also related to the heading angle and the drift angle. The figure 5.5 shows the relations
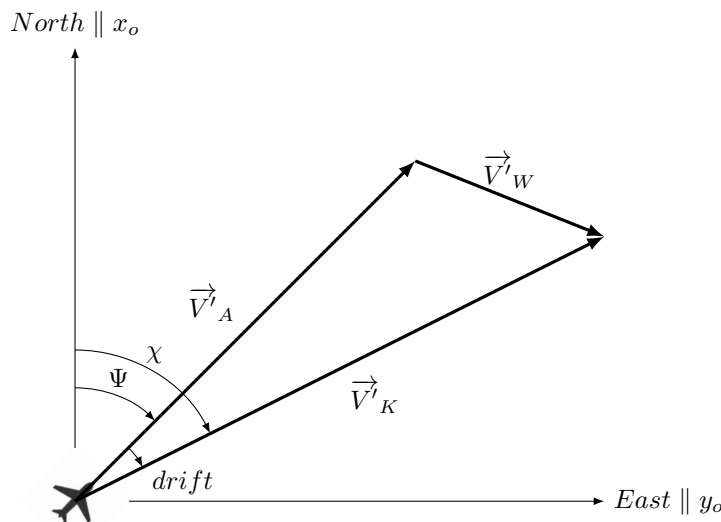
Figure 5.5: Track angle visualisation

in case of no sideslip angle. In this case, the direction of the airspeed with respect to the oncoming flow projected on the North-East plane ($\overrightarrow{V'}_A$) and the aircraft body axis projected on the same plane coincide. The heading angle Ψ is the angle between them and the North axis. The inertial speed $\overrightarrow{V}_K$ differs from $\overrightarrow{V}_A$ due to the wind vector $\overrightarrow{V'}_W$. The angle between the North axis and the projected inertial velocity vector ($\overrightarrow{V'}_K$) is the track angle. Thus the difference between heading and track, caused by the wind, is considered the drift angle.

For the purpose of this project, the track angle has to guide the directional motion of the HAP, in order to be perfectly aligned with the runway, through a guidance algorithm, based on the cross-track error, which constitutes the lateral deviation from the centre line.

5.4 Different controllers

From this section, all the examined control algorithms will be shown, from the most simple outer loops to the total heading control system. In the end, this latter is the selected one, so only its basic structure will be presented here, while all the further developments are shown in a separate section 5.5

5.4.1 Base configuration

All of the different controllers have the same architecture and structure, and they are arranged in parallel, so that a choice can be made through a multiport switch, as in figure 5.7. An example of one of them is shown in figure 5.6, and their structure is as follows:

- **Input**: by the *Aircraft_Motion* signal, which carries different state and output variables from the flight dynamics that are used as feedback variables for the controller.

- **Output**: by the three command signals, namely the rudder command (*Rudder*), the left aileron command (*Ail_LH*) and the right aileron command (*Ail_RH*).
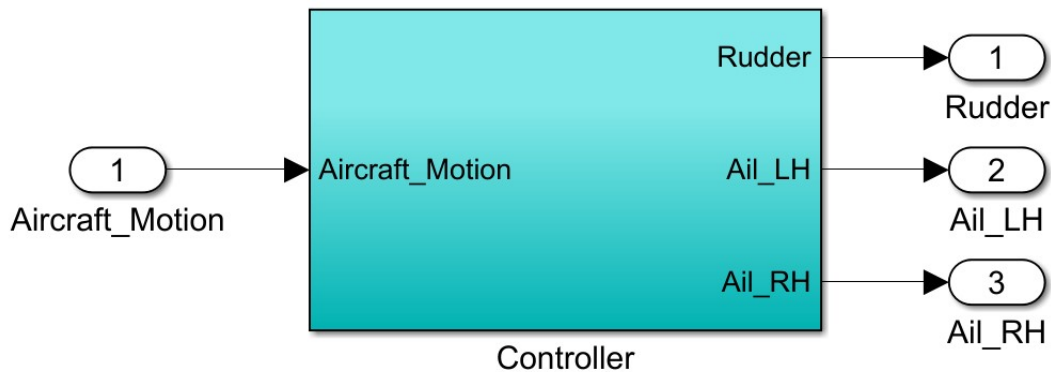
Figure 5.6: Basic controller sybsystem

Potentially, the three output signals are either carried as one mux signal or separated, depending on the input application. Image 5.7 shows actually the generic layout of the lateral landing controller subsystem, which is also integrated into the bigger general landing control subsystem.

Then, the three control surface commands are directly added to the other control surface commands named *Ctrl_Cmd*, which directly controls the deflections of each flight control surface by first passing through the actuators and then to their actual dynamics, rates and limits. In the bigger context of the overall landing controller, the lateral one is supported by the longitudinal one, already developed at DLR, which controls the longitudinal variables, and it produces a different command, made up of the stabiliser command, as well as propeller commands used in for the landing.

It is also due to say that, while this chapter is presenting the lateral controller, the final purpose of the Simulink model and all of the following subsystems is to use this controller for the simulation of the landing procedure, and this is why both the lateral and longitudinal controller are placed inside a bigger subsystem, which is the landing controller one.

5.4.2 Free responce

Before examining all the controllers, a free response is presented, in order to assess the general capabilities of the HAP. So, no controller is active and no command is applied in this case. The results will be always shown in different forms: the x-y plot showing the relative trajectory with respect to the starting point at (0,0), the $\chi - \beta$ plot (meaning the time histories of χ and β), for a better view of these two variables, a general plot with the most useful and important variables of interest.

First of all, the input for the system is constituted by a combination of different types of lateral winds, as in figure 5.2. The wind is defined in an Earth-fixed North-East-Down coordinate system and for the analyses performed here, the wind input is applied to the x-coordinate signifying a South-incoming wind.
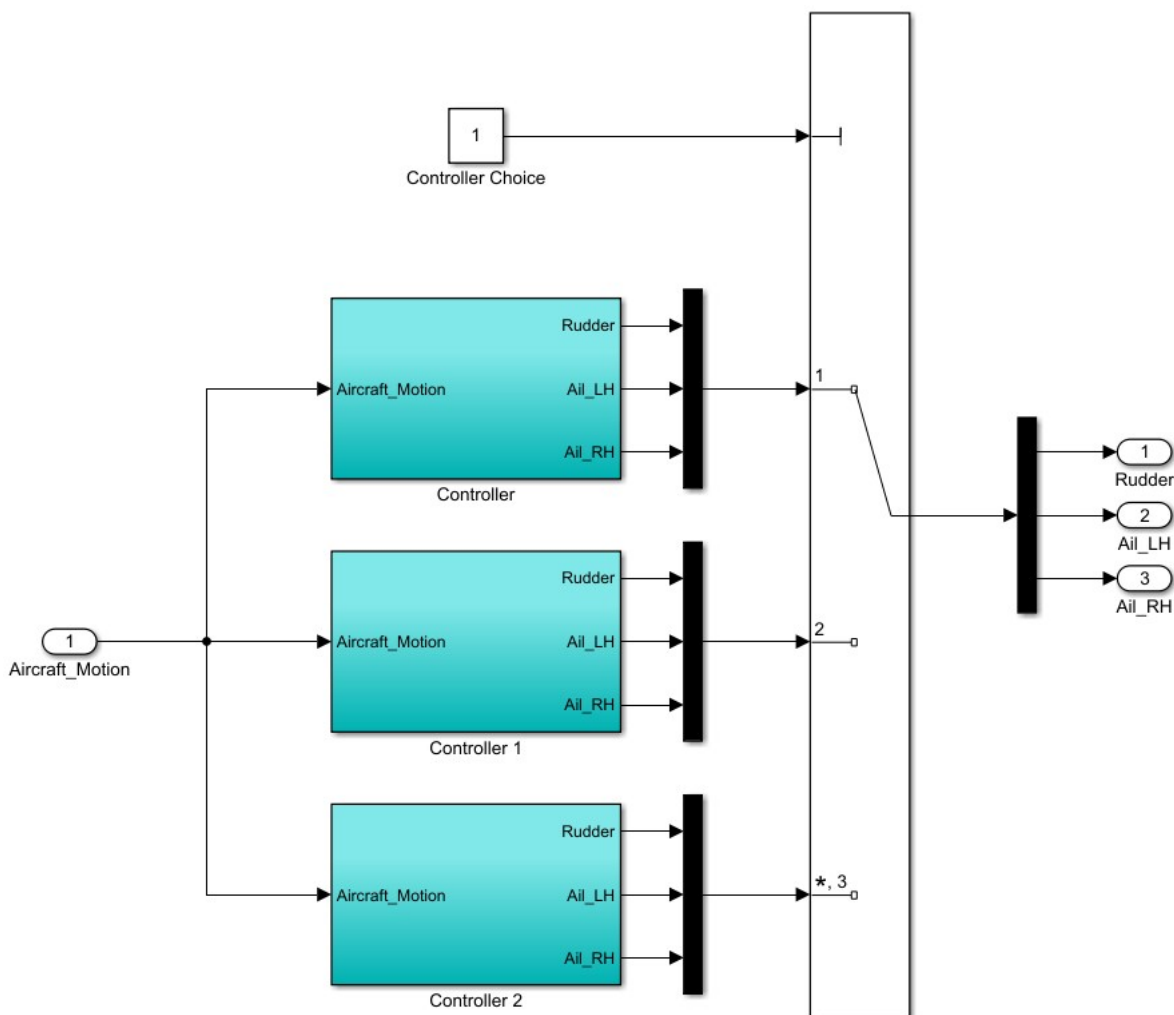
Figure 5.7: Multiport switch design

However, with the aircraft heading to the West, this wind is coming laterally. This is also represented by the wind component v_{W_b}, meaning that this is the y-component of the wind vector in the body frame, as visible from the third subplot of figure 5.10.

Again in the same figure, the last two subplots are the left aileron and the rudder command respectively, as proof that no input is given to counteract the lateral wind. Generally, the default condition for every simulation in this section is shown in table 5.1:

Table 5.1: Simulation initial conditions

Parameter	Value	Unit
χ & Ψ	$\frac{3}{2}\pi$	rad
V_{TAS}	9	m/s
$h_{o.G.}$	20	m

The first important consideration regards the sideslip angle β, shown in figure 5.9, which easily comes
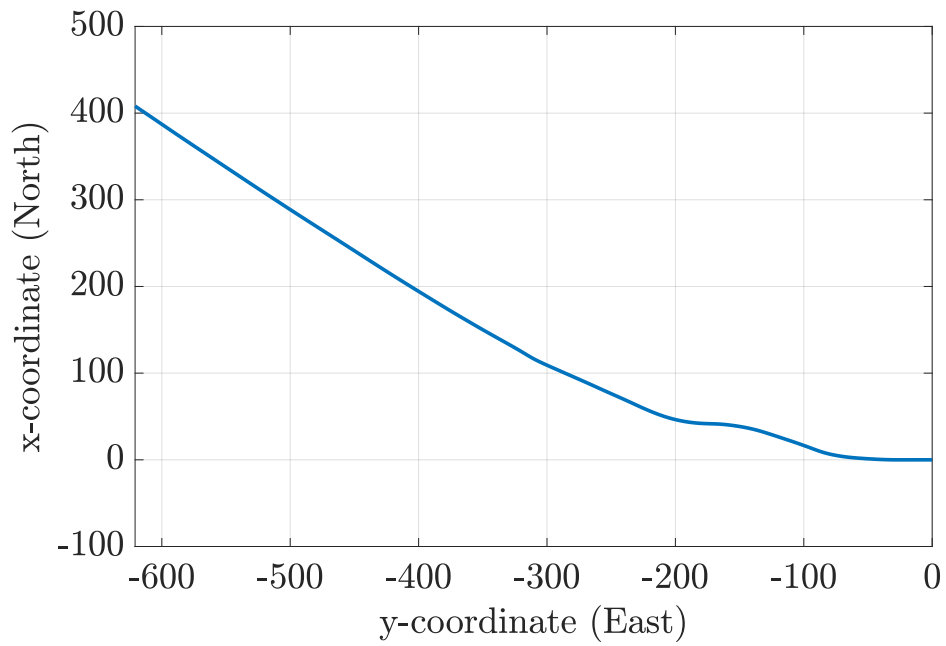
Figure 5.8: x-y trajectory (free response)
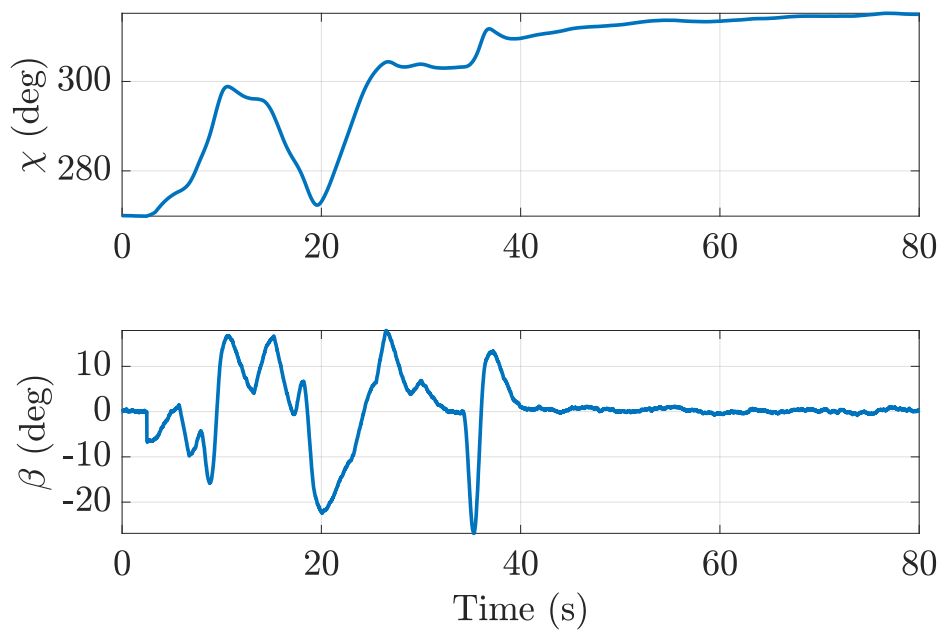
Figure 5.9: $\chi - \beta$ plot (free response)
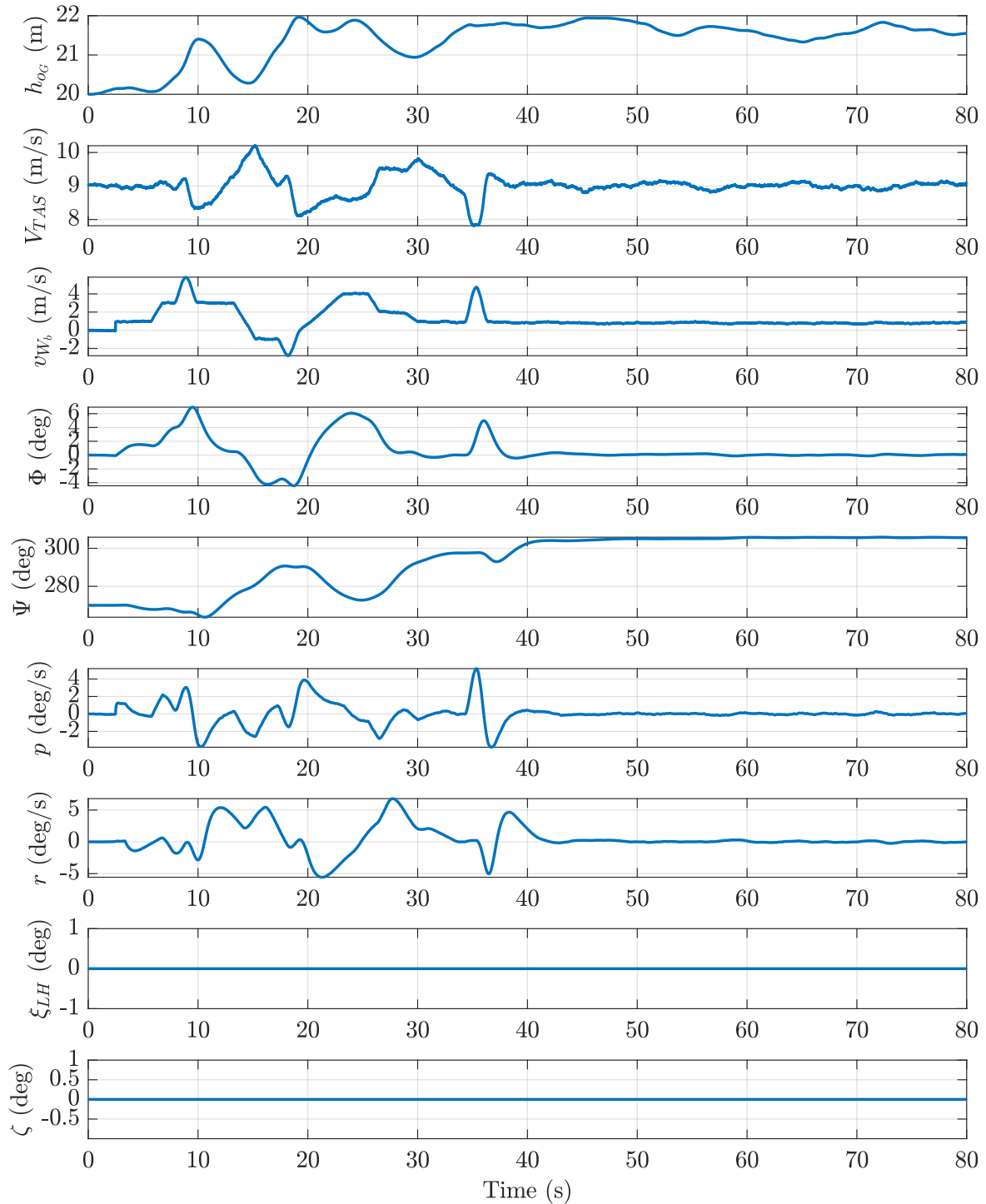
Figure 5.10: Time histories (free response)

back to zero after the perturbation. This is because the aircraft has weathercock stability. While the proposed approach may seem acceptable, it's essential to consider the inherent sluggishness of the HAP and its significant coupling between roll and yaw axes. Allowing complete freedom for such a critical variable could result in undesired consequences, potentially compromising the aircraft's controllability and inducing instability during flight. In this context, it's important to emphasize that the adjustment of β primarily aims at improving track following rather than stabilizing the aircraft. Hence, the current strategy suffices, as β control is required primarily for enhancing trajectory tracking rather than stabilizing the system.

Then, the χ plot gives a clear representation of the right lateral deviation from the runway. Indeed, since the lateral wind comes predominantly from the left (positive v_{W_b}) the aircraft tends to deviate to the right with respect to its reference system. This behaviour is completely normal for this case and also shows further interesting insights regarding some other key variables. For example, both the lateral-directional angular rates (p and r), respectively along the x-axis and the z-axis are perfectly coherent with these external disturbances, in the sense that the aircraft responds positively to inputs given to the system and then returns to a 0 condition. If this is not the case, i.e. if both the roll rate and yaw rate persist at a non-zero value even after the disturbance has ended, this could be a symptom of instability of the lateral-directional modes, particularly the Dutch roll, which employs both of the above variables in a coupled manner.

The last mention regards the altitude $h_{o.G.}$. As visible, its value is not constant for all the time history, instead it increases a bit. This is mainly due to the interaction between two factors. The first is that when the aircraft encounters an external wind disturbance, the latter introduces energy into the system. The second consists of the trim, which spends part of the energy in the system to keep the true speed constant, while the remaining energy from the wind goes into climbing.

5.4.3   Sideslip and roll control

The sideslip and roll control is the first automatic stabilisation attempt. It inherently cannot perform the required task, as the track angle is not controlled, and therefore unsatisfactory results are to be expected, but it is nevertheless useful to understand how the aircraft behaves and how it reacts to disturbances with the help of a first controller. A PD controller is directly applied to Φ and β, where the reference values are $\Phi_c = 0$ rad and $\beta_c = 0$ rad. The final command goes respectively to the ailerons and the rudder.

Structure and Parameters

The structure of this controller is shown in figure 5.11, while its main parameters are summarised in table 5.2. As already said it is constituted by a simple PD structure for both channels.
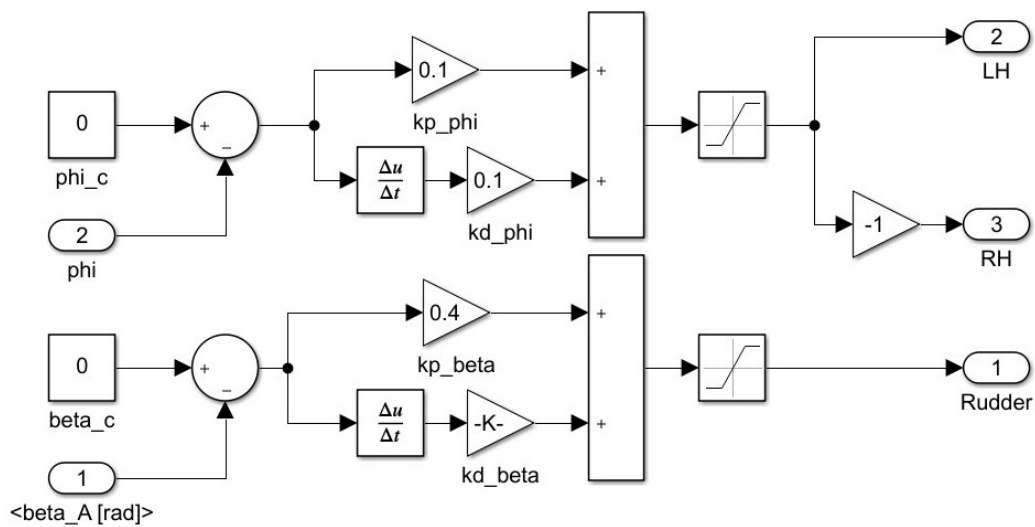
Figure 5.11: β and Φ controller structure

Table 5.2: β and Φ controller parameters

Channel	Symbol	Value	Unit
	K_{P_Φ}	0.1	-
Φ	K_{D_Φ}	0.1	s
	$\Delta\Phi_{sat}$	±0.2618	rad
	K_{P_β}	0.4	-
β	K_{D_β}	0.05	s
	$\Delta\beta_{sat}$	±0.2618	rad

Responses

Even if the controlled variables follow the commanded values, this controller is unable to ensure stability against lateral disturbances, as the track angle diverges (figure 5.13), and with it the aircraft's lateral deviation (figure 5.12).

In addition to this, the commanded values of aileron and rudder are as significant in amplitude (figure 5.14) as they are inefficient in terms of disturbance response, demonstrating that this type of controller is not suitable for the requirements imposed. So the performances are globally unsatisfactory, suggesting the use of a different strategy.

5.4.4   Track and roll control

The track and roll control is based on the same principle as the previous controller, but, in this case, the rudder control is driven by the track angle instead of the sideslip angle. The new reference value for it is freely chosen to be $\chi_c = \frac{3}{2}\pi$ rad.
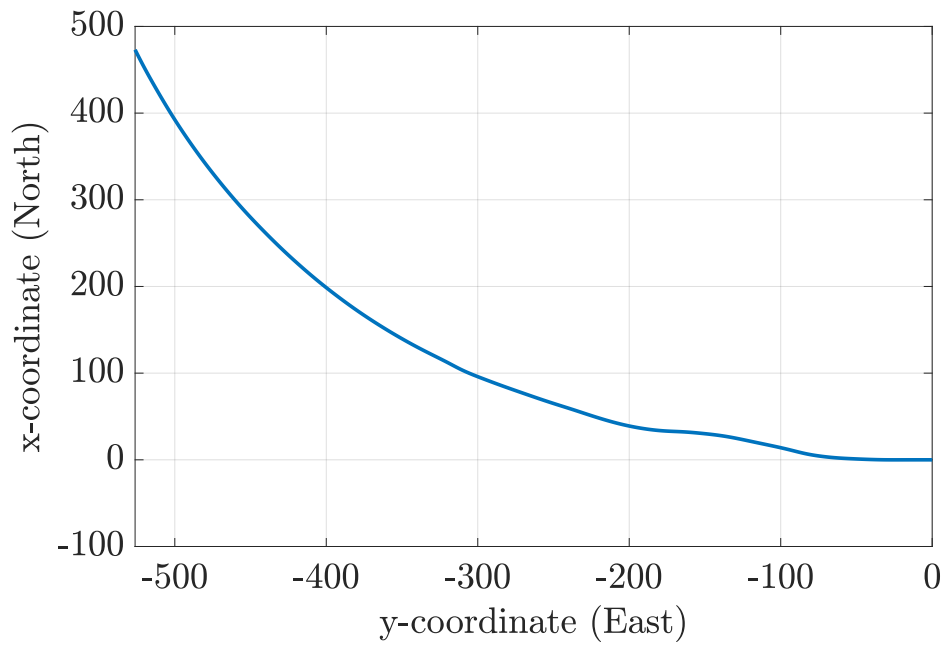
Figure 5.12: x-y trajectory (β and Φ controller)
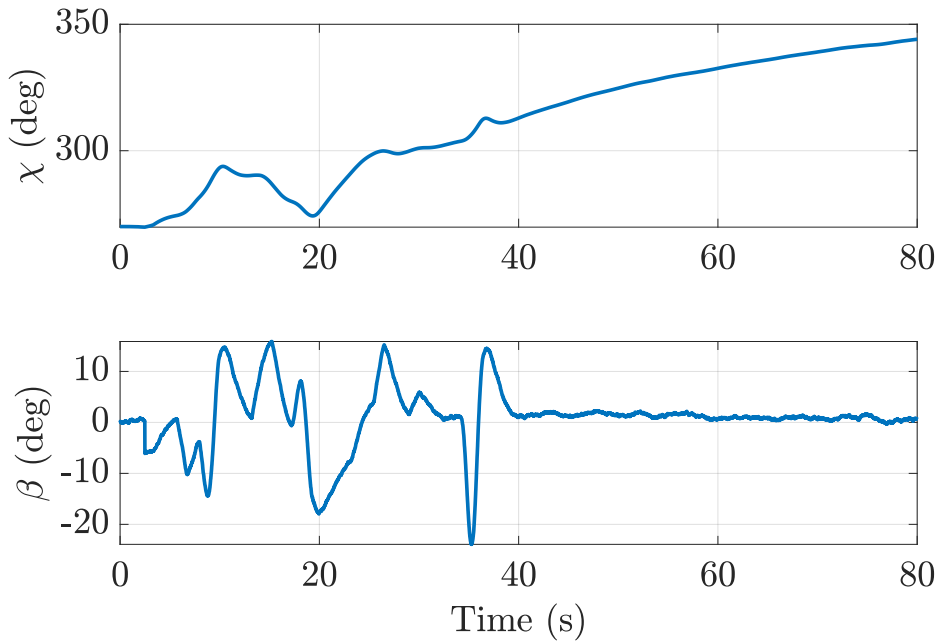
Figure 5.13: $\chi - \beta$ plot (β and Φ controller)
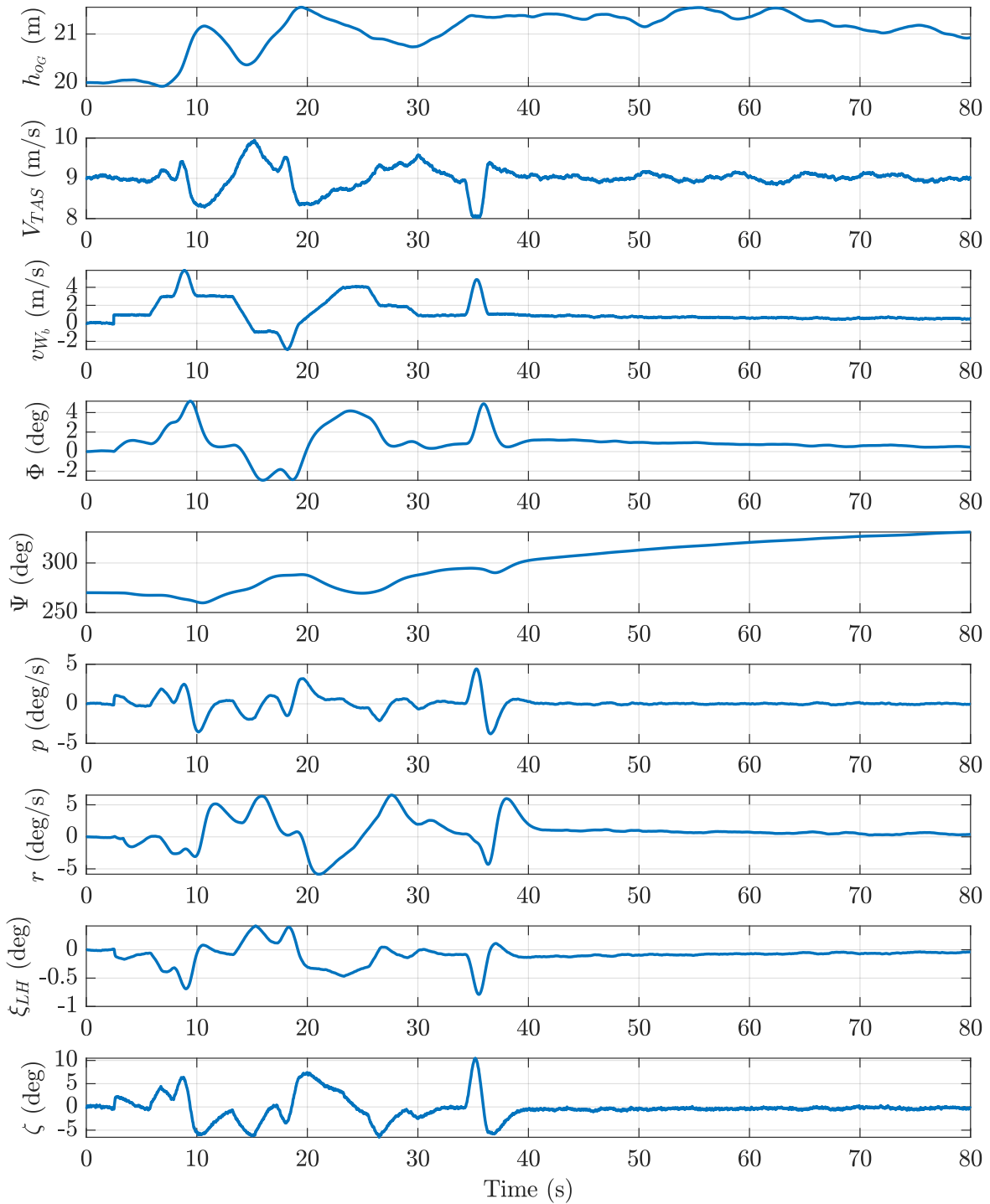
Figure 5.14: Time histories (β and Φ controller)

Structure and Parameters

The structure of this controller is shown in figure 5.15, while its main parameters are summarised in table 5.3. Again, it is constituted by a simple PD structure for both channels.
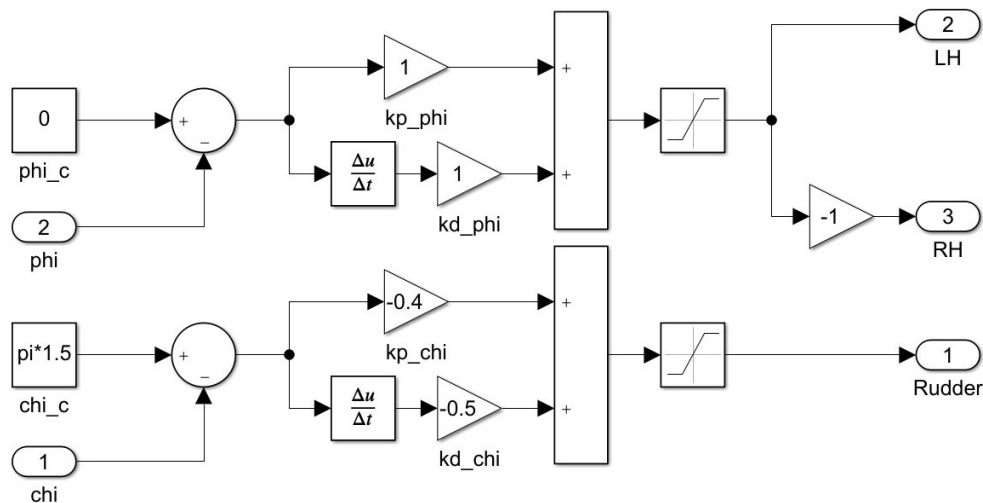
Figure 5.15: χ and Φ controller structure

Table 5.3: χ and Φ controller parameters

Channel	Symbol	Value	Unit
	K_{P_Φ}	1	-
Φ	K_{D_Φ}	1	s
	$\Delta\Phi_{sat}$	± 0.2618	rad
	K_{P_χ}	-0.4	-
χ	K_{D_χ}	-0.5	s
	$\Delta\chi_{sat}$	± 0.2618	rad

Responses

By analysing the results, which are very different from the previous controller, it is possible to highlight the main features of this new approach:

- The lateral deviation from the centerline is well below the previous one (figure 5.16). This emphasises how necessary it is to include the track angle among the controlled variables, since the main goal of this controller is to follow a specific track.

- The sideslip angle is stable also without any controller, as shown in figure 5.17, even if this does not mean that it does not need it.

- Although this result is much better than the previous one, the model is difficult to tune, as there is little freedom to choose in terms of parameters to be changed, namely, the gains of the PD
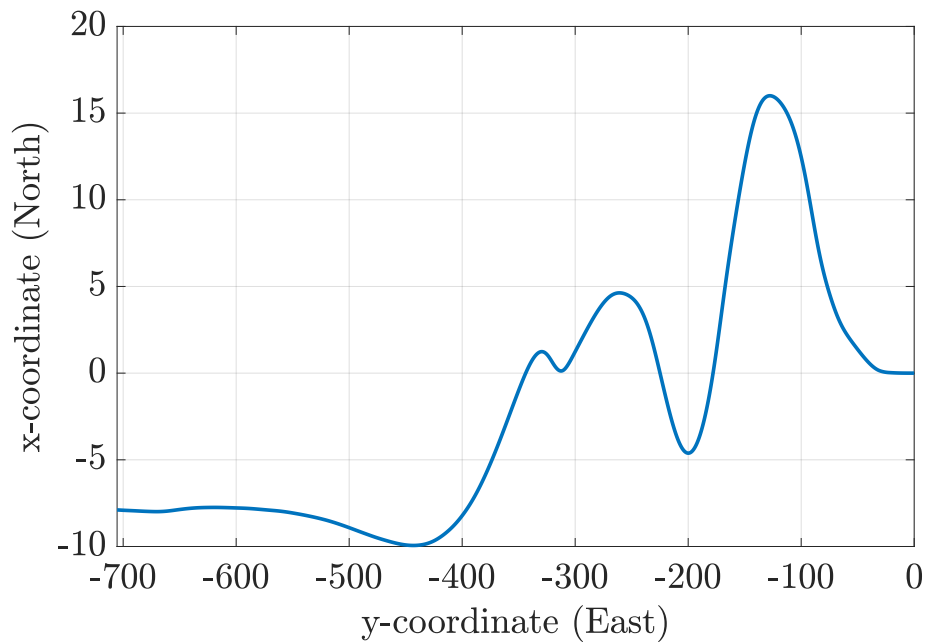
Figure 5.16: x-y trajectory (χ and Φ controller)
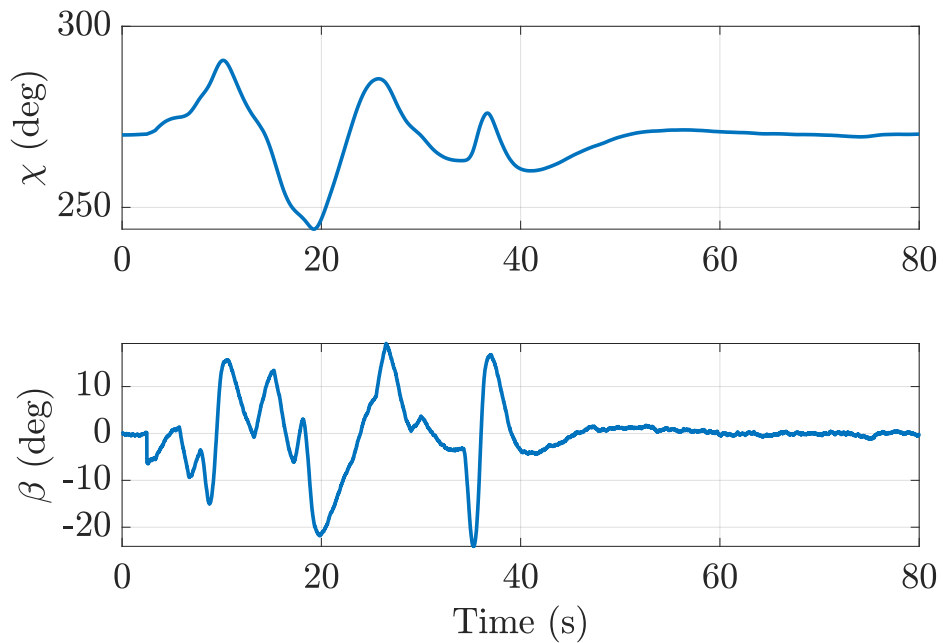
Figure 5.17: $\chi - \beta$ plot (χ and Φ controller)
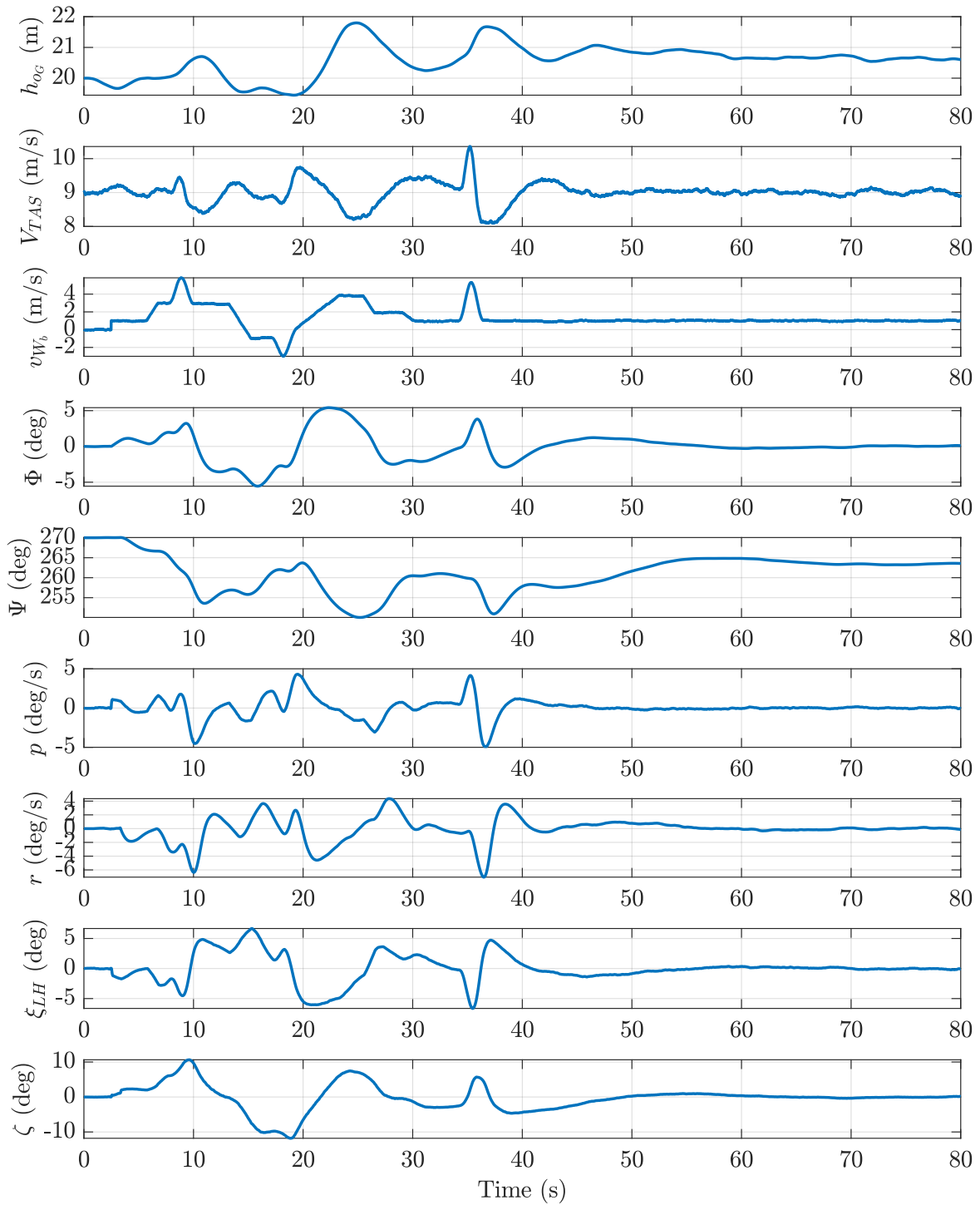
Figure 5.18: Time histories (χ and Φ controller)

controller, suggesting the need of a more sophisticated controller.

As pointed out by the latter point, this controller structure is neither organised according to an inner loop - outer loop configuration, nor has it great tuning possibilities, due to its simple structure. For these reasons, it was decided to use the last two examples given as a simple benchmark for the aircraft capabilities and to proceed with a more sophisticated controller, described in the next section.

5.5 Total heading control system

This section is entirely dedicated to the Total Heading Control System, named THCS from now for ease of use. It is the designated control strategy for this project, and will therefore be analysed in more detail than the previously presented algorithms. Starting with the historical background of its development, the mathematical model is explained in its original and simpler form, since many modifications and updates were proposed during the years. Then, the basic design is presented by using the Simulink implementation, and the first results are shown. From this point, a long series of improvements were made to adapt the controller to the needs of the project.

5.5.1 Background

The major problem of classical Automatic Flight Guidance and Control (FG&C) systems is that they rely on SISO (Single-Input, Single-Output) control strategies, leaving aircraft susceptible to Loss of Control (LOC). The majority of modes in FG&C systems are deemed non-flight critical, implying that the flight crew is expected to identify and handle any malfunctions in these modes safely. Unfortunately, this assumption has frequently proved to be unfounded. Consequently, there has been an excessive number of incidents and accidents related to automation failures. As a consequence, a MIMO (Multi-Input, Multi-Output) control strategy should be preferred in order to take advantage of flexibility, simultaneous control of multiple variables, improved precision, enhanced stability, adaptability to system changes, and effective interference management, which are crucial features of complex systems.

The THCS (and its longitudinal counterpart TECS - Total Energy Control System) is part of the Total Energy Based Control Systems, which are the result of the work carried out by NASA from the eighties, and patented [24] for the interest of The Boeing Company. All the development of this section is based on the work of A. A. Lambregts, who is the inventor of both TECS and THCS and more specifically on his main paper regarding the design of this control system [23].

5.5.2 Design objectives

As said in the reference paper [23], the objectives of the THCS are:

- Use of one pilot-like MIMO-based control strategy for all automatic and manual control modes.

- Full authority integrated lateral directional control, including automatic roll and yaw retrim, to prevent LOC due to engine out roll-yaw divergence.

- Generalized functionally integrated design, consistency of operation between modes.

- Elimination of Yaw Damper, Turn Coordinator and Thrust Asymmetry Compensator.

- Decoupled Mode Command responses, reduced controller activity.

- Reduced design complexity by using shared modular building blocks, elimination of mode overlap and simpler mode processing.

- Simpler, more intuitive Mode Control Panel (MCP), clearer Flight Mode Annunciation (FMA).

- Large cost reductions by generalized/reusable design, minimal application-specific development, reduction in laboratory and flight testing and shorter application development cycle.

Without considering all of them, because of the further implementations of the paper, the first 3 points are the most important in this work, mainly because:

- There is the possibility to easily tune the model as if a human was interacting with the system.

- It is completely independent of the longitudinal plane, and allows total control of the lateral-directional variables.

- Even if the structure is more sophisticated with respect to the classical inner-outer loop, it consists of an aeroplane-independent design part, which is the core of the THCS.

In the end, due to its numerous advantages, it is the final choice for this project, also in cooperation with the already designed TECS as the longitudinal (and landing) controller.

5.5.3   Mathematical derivation

The mathematical derivation of the THCS is going to be based on the work of Parente and Paglione [30], which follows an inductive approach to demonstrate the correlation between the action and the consequent control. Starting with the aeroplane-independent design, the outputs are:

$$
\begin{cases}
\Phi_c = K_{RI} \frac{V_{TAS}}{g} \int (\Delta\dot{\chi} + \Delta\dot{\beta})\, dt = K_{RI} \frac{V_{TAS}}{g} (\Delta\chi + \Delta\beta) \\
r_c = K_{YI} \int (\Delta\dot{\chi} - \Delta\dot{\beta})\, dt = K_{YI} (\Delta\chi - \Delta\beta)
\end{cases}
\tag{5.2}
$$

Here,

$$
\begin{cases}
\Delta\dot{\chi} = \dot{\chi}_c - \dot{\chi} = K_\chi \Delta\chi - \dot{\chi} = K_\chi(\chi_c - \chi) - \dot{\chi} \\
\Delta\dot{\beta} = \dot{\beta}_c - \dot{\beta} = K_\beta \Delta\beta - \dot{\beta} = K_\beta(\beta_c - \beta) - \dot{\beta}
\end{cases}
\tag{5.3}
$$

Table 5.4: THCS channels scheme

Channel	Variable	Action	Inner Loop	Outer Loop
Lateral Path Mode	χ or Ψ	Sum	p	$\xi_{aileron}$
Directional Control Mode	β	Difference	r	ζ

The final aim is to control the ailerons with the roll rate and the rudder with the yaw rate, as summarised in the table 5.4.

The most peculiar feature of this control system is the mixing structure, which behaves as the interface between the independent design and the tailored one. In fact, the aim is to control the sum of the errors $(\Delta\dot\chi + \Delta\dot\beta)$ to control the ailerons and the difference between them $(\Delta\dot\chi - \Delta\dot\beta)$ to control the rudder. This means that by controlling the sum and the difference between two variables, their individual values can also be controlled.

The demonstration of this is deducted from the equations of motion of an aircraft, with an additional note on Ψ and χ. In the derivation, the heading angle is the only one considered, even if in the general controller, it can be substituted by the track angle, since this channel represents the general lateral path. Starting with the second equation of translation (along the y-axis):

$$\dot v = -ru + pw + g\sin(\Phi)\cos(\Theta) + \frac{Y}{m} \tag{5.4}$$

And assuming that w, Θ are equal to zero (small angle of attack), Φ is small (levelled flight), Y only contains aerodynamic forces ($Y = Y_A$), the sideslip angle is small ($v = V\beta$, $u \propto V$) and the velocity V is constant ($\dot v = V\dot\beta \propto u\dot\beta$):

$$\Phi = \frac{u(\dot\beta + r)}{g} - \frac{Y_A}{mg} \tag{5.5}$$

Φ channel

Starting from equation (5.5), the derivation of the Φ components assumes a coordinated turn ($Y_A = 0$, $\dot\beta = 0$) and $r \propto \dot\Psi$:

$$\Phi \propto \frac{V}{g}\dot\Psi \tag{5.6}$$

Here, it is possible to note that a positive variation on the heading angle has a positive influence on the roll angle, which is quite intuitive. In the same way as the previous deduction, starting from equation (5.5), and by considering the case where the heading is constant ($r = 0$), the result is:

$$\Phi \propto \frac{V}{g}\dot\beta \tag{5.7}$$

63

This demonstrates that a positive variation of the sideslip angle has a positive influence on the roll angle. Then, from equations (5.6) and (5.7), it is reasonable to assume that:

$$\Phi \propto \frac{V}{g}(\dot{\Psi} + \dot{\beta}) = \frac{V}{g}f(\dot{\Psi} + \dot{\beta}) \tag{5.8}$$

As in the basic design, the function $f(\dot{\Psi} + \dot{\beta})$ is a simple sum, but it could be expanded more depending on the necessities.

Ψ channel

In this part, only a yaw rate is commanded, with a roll angle equal to zero. By this assumptions, in addition to the fact that the aerodynamic forces have a transient phase, the equation (5.4) becomes:

$$\dot{v} \propto -ru \tag{5.9}$$

Then, remembering that V is constant ($\dot{v} = V\dot{\beta} \propto u\dot{\beta}$), and substituting in eq. 5.9:

$$r \propto -\dot{\beta} \tag{5.10}$$

This demonstrates how a negative variation of the sideslip rate increases the yaw rate, while, as already assumed before, a positive variation of the heading rate linearly increases the yaw rate ($r \propto \dot{\Psi}$). These two statements can be summarised as:

$$r \propto \dot{\Psi} - \dot{\beta} = f(\dot{\Psi} - \dot{\beta}) \tag{5.11}$$

In conclusion, this latter equation, together with equation (5.8) demonstrates the basic design of the controller (equations (5.2)).

5.5.4 Interpretation

The main difference between a classical control approach and an Energy-Based FCS is that in the former, the control structures are virtual, whereas in the latter are physical. In fact, while a general PID structure is only present in the FCS, an energy-based FCS directly uses the equations of motion and the conservation of energy to create the new input for the system, as already demonstrated. The two different channels of the THCS can be considered as two throttles which allow the addition or subtraction of energy to the system, in terms of attitude variation, and this leads to a separate control over the two states.

The aircraft energy management concepts are considered vitals for enabling the vehicle (and the eventual pilot) to follow the desired path and to detect, correct, and prevent unintentional deviations from the original energy state [2]. The general energy management of an aircraft is a balance between

the net energy change and the stored energy variation. In the TECS case, those quantities are likened to the kinetic and potential energy, which, when added together, produce the total mechanical energy.

Instead, for the lateral case, and then the THCS, even if there is no explicit "lateral total energy", the two channels can be seen as throttles that put and rearrange some energy into the system. In particular, the roll channel represents the amount of bank put into the system, while the yaw channel manipulates it, controlling how much of that banking energy is split between turning or slipping flight conditions.

5.5.5   Basic design

From this point, all the evolutions and modifications made to the FCS will be discussed, starting from its original structure described in [23]. While the basic structure is always the same, various modifications have been made to adapt the controller to the desired performance, available parameters and operational limits.

The basic design of the controller is shown in figure 5.19. From the left, the aircraft independent design starts with the commanded track angle and sideslip (χ_c set per default at $\frac{3}{2}\pi$ which represents the runway heading, and β_c, always set to 0) up until the two integrators located in the middle of the channels, producing as system outputs respectively Φ_c and r_c.

The process starts with a parallel normalisation of the two errors in two standard commands. So, the lateral path control mode error is firstly converted to a $\dot{\chi_c}$ command, which gives the final track angle rate error $\Delta\dot{\chi}$, while the directional control mode error is normalised to a $\dot{\beta_c}$ command, which then gives the final sideslip angle rate error $\Delta\dot{\beta}$. These two signals are the input for the mixing structure of the THCS.

This, starting with the tailored design, takes the total sum of the two errors $(\dot{\chi} + \dot{\beta})$ to develop the roll control command through an inner loop roll angle command (Φ_c) and a conventional roll-error and roll rate feedback control loop, and the distribution of the two errors $(\dot{\chi} - \dot{\beta})$ to generate the yaw control command, by directly giving the yaw rate command r_c to the feedback control loop.

The response is way improved with respect to the previous attempts, when separate variables were controlling the highly coupled dynamics. In this case, which constitutes the most simple and basic design, there is a higher level of control over the interested variables, thanks to the more complex structure of the controller.

However, while it is a good starting point, it is still not satisfactory since:

- It is not possible to directly act on the final outputs since the inputs are mixed in the central part of the controller. Consequently, a subsequent guidance algorithm would not be able to command the appropriate inputs to achieve certain targets.

- For the previous reason, the tuning of the model is extremely onerous and far from intuitive. It is in fact quite difficult to act on a single variable without having unwanted repercussions on other variables since the structure of the model itself is intricate by nature.
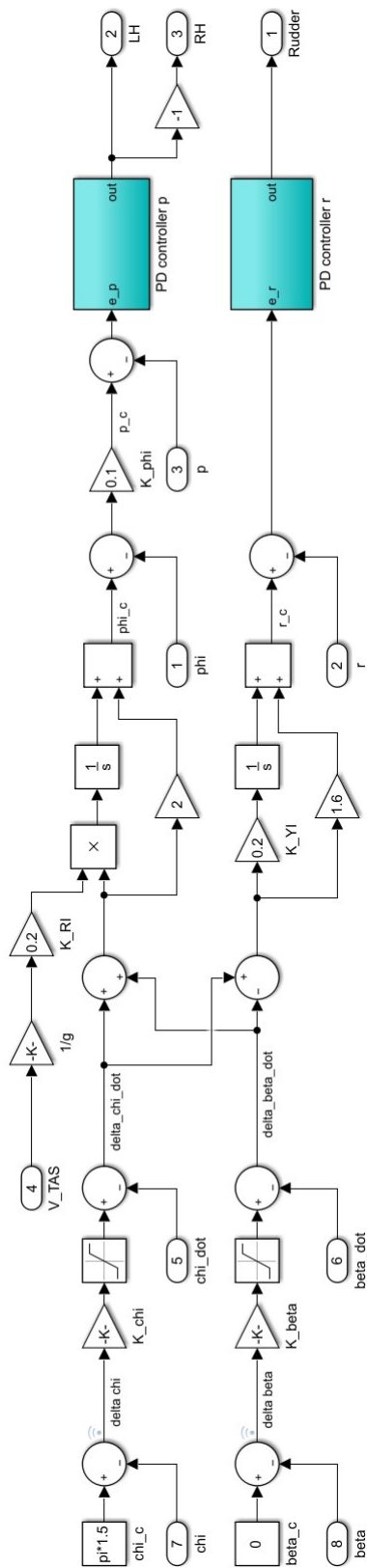
Figure 5.19: THCS basic design

To address the above-mentioned complexities, it is clear that a more advanced controller is essential. This would enable finer control over specific variables. To achieve this, there is a need to leverage the complexity of the system's structure to optimize interactions between its elements. Thus, a comprehensive review of the current model's issues and their resolution is presented below.

5.5.6   Filtering

The first modification of this model regards the two feedback signals $\dot{\chi}$ and $\dot{\beta}$. They are coming from the motion feedback, which should be replaced by sensors. In both cases, the raw signals present high noise, due to the atmospheric turbulence. For this reason, it is necessary to filter them, and, to do so, a spectrum analysis is the fastest tool to use to see which is the frequency content of each of them, to choose the correct filter.
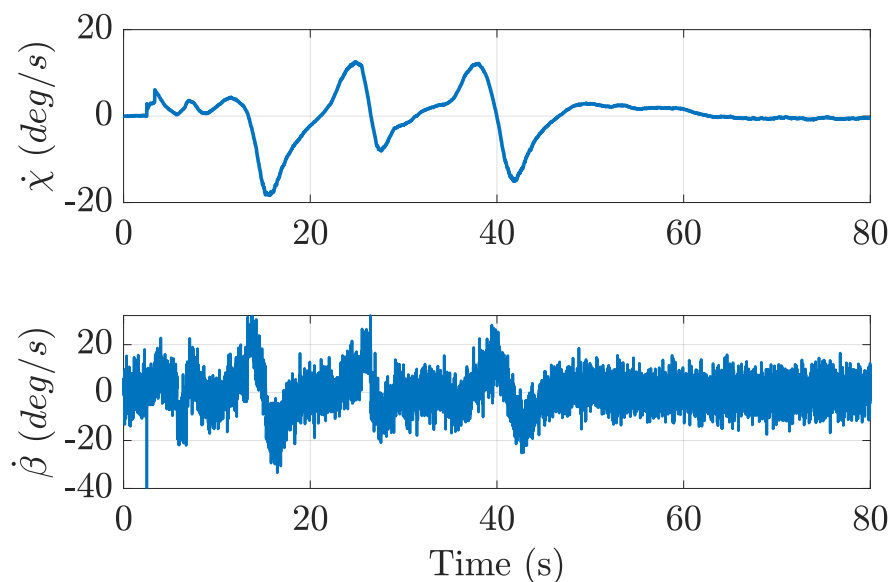
Figure 5.20: Raw $\dot{\chi}$ and $\dot{\beta}$ signals

As visible from the image 5.20, the two signals, and $\dot{\beta}$ more specifically, present a generalised noisy behaviour, but also a spike in correspondence of the beginning of the lateral wind. This trend must be filtered to improve the controller behaviour and to avoid numerical problems in the further part of the control system, especially for any case of derivative block (which is sometimes unavoidable for PD controllers).

There is also another major role played by the filter, which is the one of emulating human response when disturbances are applied. A human pilot would actually not be able to follow such high-frequency disturbances, instead, there could be a possibility of PIO (Pilot Induced Oscillations), which could be fatal for the vehicle. So, to avoid this, the filter will correct the two signals in such a way that rather

lower frequency inputs are applied, similar to the case in which a pilot is interacting with the FCS.

The following computations are mostly regarding $\dot{\beta}$, since it is the worst of the two signals, showing only its frequency spectrum.

Fast Fourier transform

The Fast Fourier Transform (FFT) is an optimised algorithm for computing the Discrete Fourier Transform (DFT) of a signal, which is the digital (discrete) version of the general (analogue/continuous) Fourier Transform (FT). For any discrete signal, the definition of the DFT is:

$$X_q = F_d(x_n) = \sum_{k=0}^{N-1} x_k \cdot e^{-i\frac{2\pi}{N}kq}, \ for \ q \ = 0, \ 1, 2, ..., N-1 \tag{5.12}$$

Where N is the total number of discrete data points taken, $e^{-i\frac{2\pi}{N}}$ is a primitive Nth root of 1, and x_k is the input discrete signal. The aim of the FT, which is a generalisation of the Fourier Series, is to determine the frequency content of a signal.

Frequency spectrum

The output of the FFT is then a vector of complex numbers, which can be used to extract the frequency spectrum. First, it is necessary to calculate the modulus of each complex coefficient, hence $A_k = |X_k|$, obtaining an indication of how incisive each coefficient is within the vector. Then calculate the frequency at which each point in the spectrum is located, via the relation $f_k = k\frac{f_{sampling}}{N}$. Finally, by plotting the modulus of each point against its frequency on a graph, the spectrum of the signal is obtained, showing how the amplitudes are distributed.

As visible from the image 5.21, the frequency content of the analysed signal is quite noisy along all its frequency ranges. In addition, two spikes are present, respectively at a very low frequency and at almost the maximum one. This latter represents the spike visible in figure 5.20, which is due to the beginning of the wind input. The specific value is $f = 99.85 \ Hz$. This data is going to be used for the filter design.

Filter design

The usual configuration for a filter could be either a first or a second-order one. In this case, the latter is preferred because it has two parameters (natural frequency and damping/quality factor) and then, it can be more precise. The general transfer function of a 2nd order low-pass filter is:

$$H(s) = H_0 \frac{\omega_0^2}{s^2 + \frac{\omega_0}{Q}s + \omega_0^2} \tag{5.13}$$

Where ω_0 is the cut frequency, Q is the quality factor (the inverse of the damping ratio ζ) and H_0 is an eventual coefficient. Once the spike coefficient from image 5.21 is evaluated, it is good practice to set
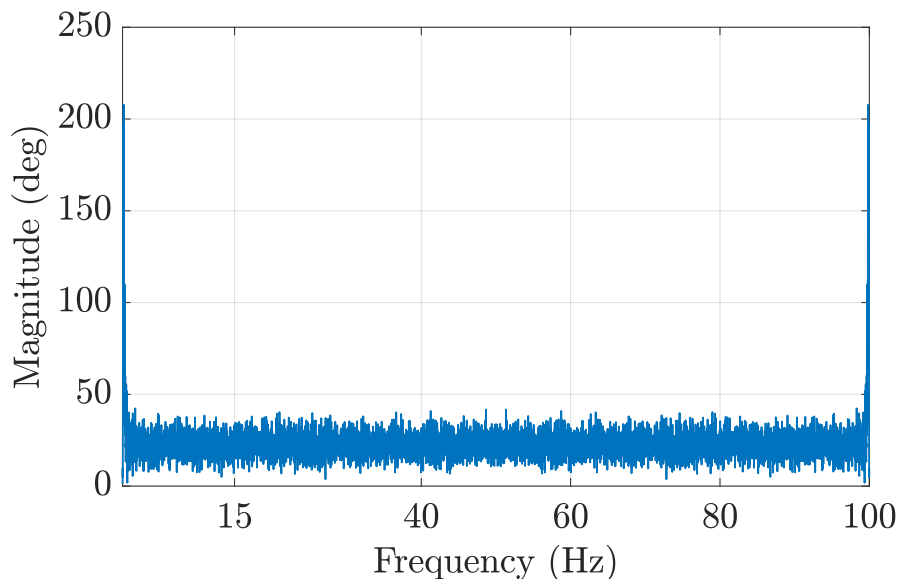
Figure 5.21: $\dot{\beta}$ frequency spectrum

the filter cutoff frequency to an order of magnitude lower than the desired one, which in this case leads to $f_{cut} = 9.985\ Hz$, and then $\omega_0 = 62.738\ rad/s$ (remembering that $\omega_0 = 2\pi f_{cut}$). The quality factor is usually chosen such that the damping ratio is the critical one ($Q = \sqrt{2}/2$). With these values ($H_0 = 1$ for simplicity), the result is the one in figure 5.22. The results are better than the original signal, mostly for the amplitude of the spike, which is reduced. However, the frequency content is still too noisy and rich, so different values are tested.

Based on the previous results, a manual filtering approach is attempted, in order to have a cleaner output. The final version of the signals has a transfer function of $H(s) = \frac{40}{s^2+9s+40}$ and it is shown in figure 5.23.

The so-obtained responses are way smoother than the original signals, with the cost of some detail loss, which is acceptable since the role of the filter is also to emulate human behaviour, which could not follow the highly noisy unfiltered signals. In the end, the properties of the filter are shown in table 5.5.

Table 5.5: Filter parameters

Parameter	Symbol	Value	Unit
Cut frequency	ω_0	6.325	rad/s
Quality factor	Q	0.703	-
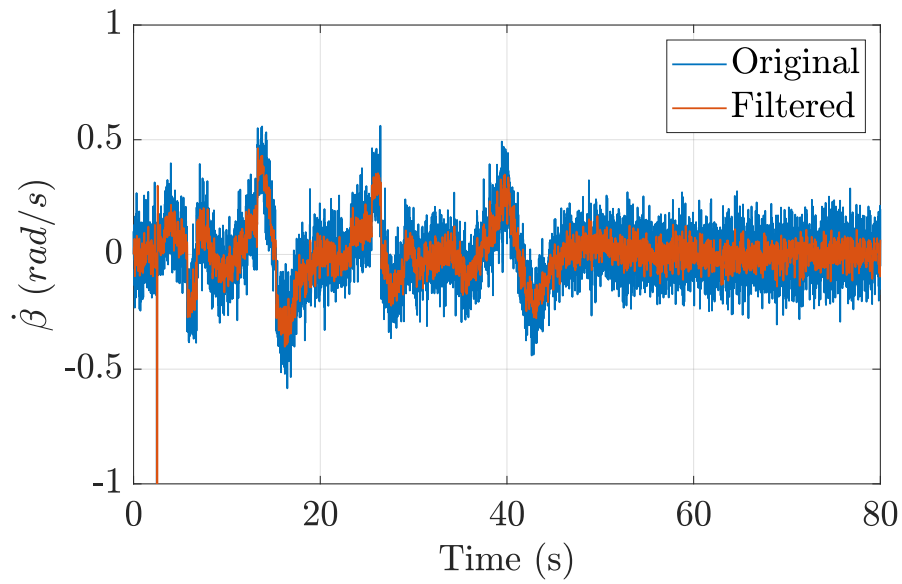
Figure 5.22: Signals comparison
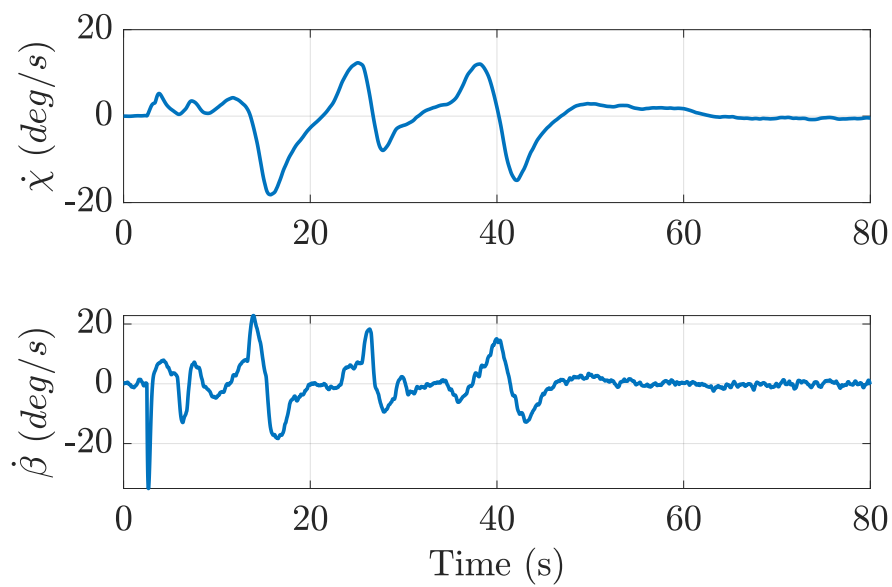
Figure 5.23: Filtered $\dot{\chi}$ and $\dot{\beta}$

5.5.7 Tuning

The tuning process represents a major task, which has to be carefully carried out keeping in mind the desired response of the system. In fact, even if usually performances are the main goal, here it could be different. Since the main role of the lateral controller is to follow the track prescribed by the guidance and navigation module and thereby align the aircraft with the runway and reduce lateral offsets due to wind as a pilot would do likewise, the most important variable is the final cross-track error/lateral deviation from the runway, in the landing context. To ensure appropriate control, several techniques are adopted and discussed in the following sections.

PD-PI controllers

The first part of every tuning process is the choice of the gains. Starting from the end of the plant, it is usually common to apply constant inputs to adjust the gains of the outer loop (PD controllers for ailerons and rudder deflections in this case), and then go backwards through the inner loop and the mixing structure. Whereas the aeroplane-tailored design (inner-outer loop) is tuned in a standard way, the mixing structure is modified to enable easier tuning.

The main idea of this new structure is to split every channel of the input variables ($\Delta\dot{\chi}$ and $\Delta\dot{\beta}$), to let both of them have their gain. In particular, the interested values are K_{RI} and K_{YI}, which by now will be just indicated with different names, as explained further. Also, they are moved before the sum blocks, so that they can be applied to every of the 4 different input channels, and then added or subtracted. This splitting operation would lead to 4 gains, two for the $\Delta\dot{\chi}$ and two others for the $\Delta\dot{\beta}$ signals, two of them referred to the upper channel (ailerons) and two which apply to the lower channel (rudder).

After this operation, some intermediate results are being analysed, showing the necessity of a higher control level, and suggesting further modification of the structure of these mixing blocks. In particular, the type of control action to be implemented in the external part of the mixing structure (i.e. the one comprising the variables to be controlled χ and β), can be integrated more compactly in the internal structure (the one operating with the temporal derivatives of the controlled variables), through a simple operation of swapping operators. For this purpose, the table 5.6 shows the correlation between the mentioned variables, and the equivalence in terms of control actions.

Table 5.6: Control actions equivalence

Control Operation ($\dot{\chi}$ and $\dot{\beta}$)	Effect to the Antiderivative Function (χ and β)
Integral	Proportional
Proportional	Derivative

Given this, a PI control is equivalent (proportional-integral) on a variable and a PD control (proportional-derivative) on its antiderivative. So, to increase the stability of the controlled variables, a derivative term would be necessary, but it is easier to embed its equivalent (proportional) in the mixing structure, along

with the integral.

Saturation and anti-windup

Another crucial aspect of enhancing the model involves safeguarding against integrator windup. This occurrence entails the excessive accumulation of errors within the integrator term of a PI/PID controller during the ascent phase (commonly known as windup). Subsequently, this results in overshooting during the descent phase, with the overshoot persisting and escalating as the accumulated error is addressed (counteracted by errors in the opposite direction). It is particularly common when there are saturations in the model (thus inherent nonlinearities), such as a maximum velocity or a physical limit to the displacement/rotation of an element.

The integral windup occurs in the $\Delta\dot{\chi}$ channel, especially when the target destinations commanded by the guidance logic are achieved in a time interval similar to that of the entire simulation. Even if the guidance description is explained in the next section, for now, it is only necessary to know that whenever the trim conditions are not very close to those commanded by the guidance algorithm, a persistent deviation of the lateral path leads to an excessive accumulation of the error, which then procures an excessive overshoot in the approach phase. This would happen, for example, if the trim conditions are changed to start with a heading of $\Psi = 90°$ (East), leading to a $180°$ turn with respect to the usual $270°$ aimed heading/track.

Different techniques can address the windup problem, two among the others:

- **Back-Calculation**: a feedback loop is used to unwind the integrator block when the controller hits specified saturation limits. The goal is to dynamically adjust the integral gain so that it does not allow excessive error accumulation during system boundary conditions.

- **Conditional Integration**: the processed variable is used to trigger a specific logic, which recognises the entering in the nonlinear region, and thus disables the integrator block. Here, the aim is to completely turn off the integral action to prevent an excessive command.

Both the mentioned techniques are quite effective, but they need a specific logic to be actuated, which cannot always be determined. For this reason, after trying the conditional integration, it was chosen to use a different and simpler method: the intrinsic saturation of the integral block. By directly limiting the integral action with a saturation block, it is easier to determine the correct limits without the use of any command logic, through a direct monitoring of the singular components of the controllers. In this way, a better and smoother result is achieved, which is never hitting the limits of each different channel and can ensure the desired performances.

5.5.8 Final controller

The final lateral controller is then presented separately in figure 5.25 and 5.26 and entirely in figure 5.24.
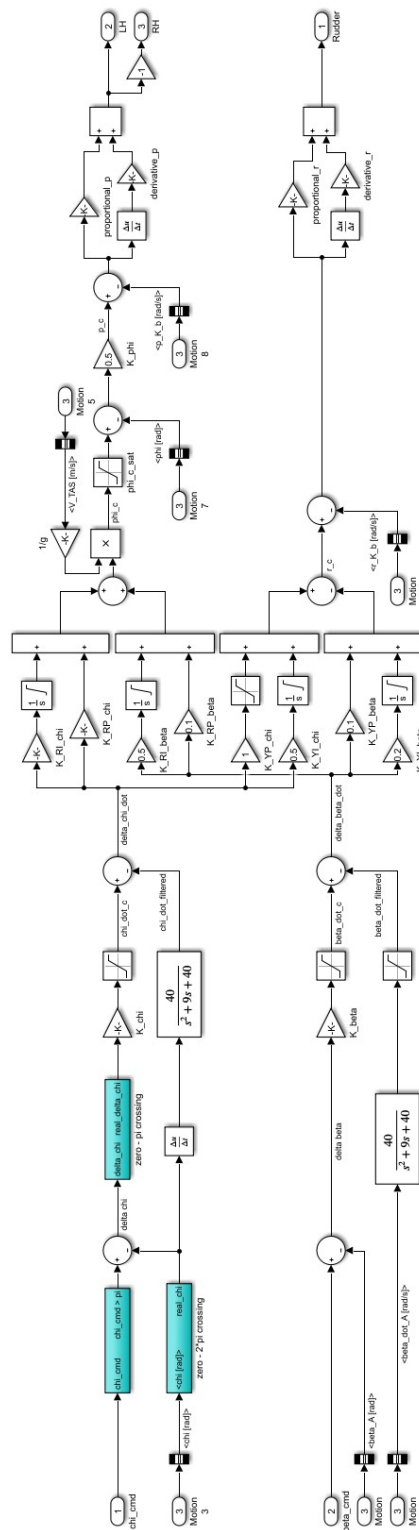
Figure 5.24: THCS final structure
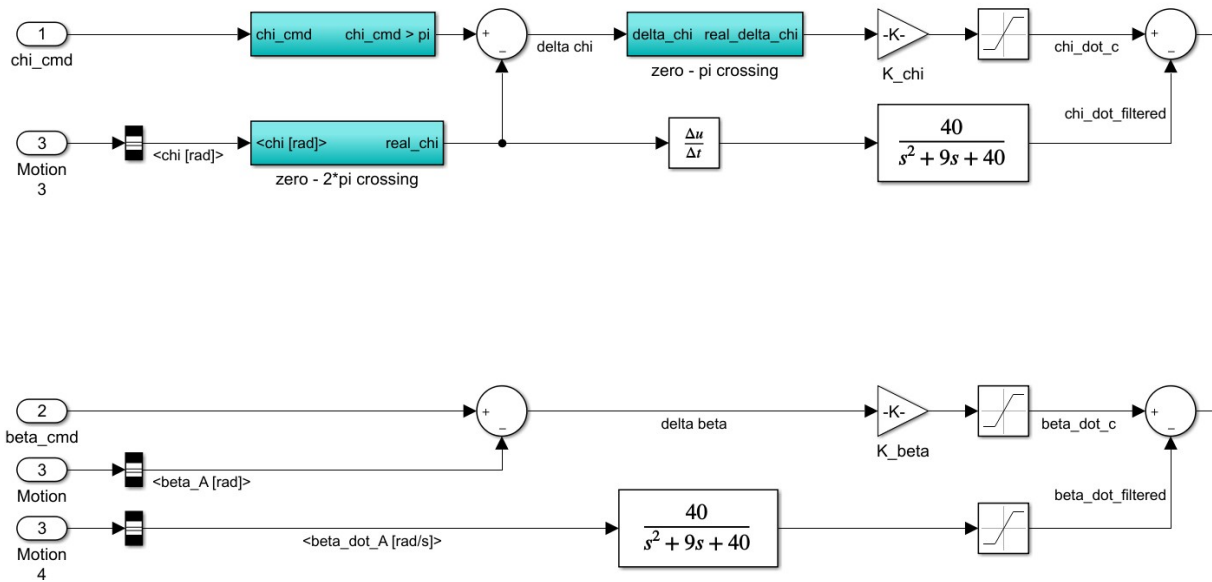
Figure 5.25: THCS final structure (first part)
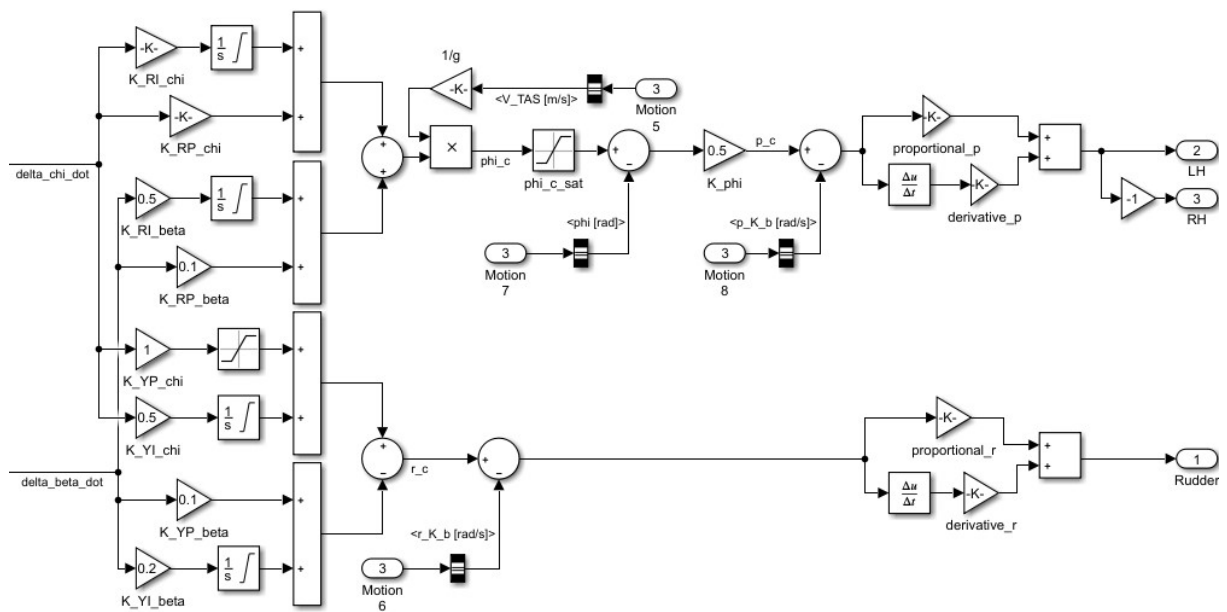
Figure 5.26: THCS final structure (second part)

5.6 Guidance

Even if the controller consists of a big part of the FCS, it cannot work without having an input generation capable of adapting to different external commands. For this reason, a guidance algorithm is needed to determine the desired path of travel towards the desired target. This allows the expansion of the FCS capabilities, by letting the HAP fly in every direction towards the target direction/point on the runway, in the landing context. Two algorithms are studied and tested, with further description on the second one, which resulted in fitting more for this case.

5.6.1 Inertial algorithm

The first proposed algorithm, designed as the inertial one, comes from the work of Park, Deys and How [31], and specifically, the linear analysis for the straight line following.

The initial setup is shown in figure 5.27. In the HAP case, and more specifically in this particular setup, the only different notation regards the variable d, which represents the cross-track lateral error, so the lateral coordinate x_o, which is directed to the positive North. It is important to note that, generally speaking, d is equal to x_o only when flying towards the runway in the West direction, but it could also assume different orientations.
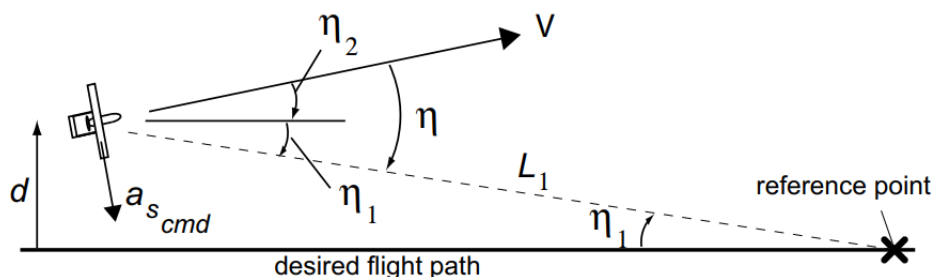
Figure 5.27: Straight line following model [31]

Then, the general notation expresses the two most important variables: $a_{s_{cmd}}$, which is the lateral (centripetal) commanded acceleration, and η, which is the angle by which to rotate the velocity vector (V) to align it with the segment (L_1) joining the aircraft with the reference point.

Starting with an initial evaluation of the vector L_1, the ideal motion is a general circular path of radius R, and the above-mentioned vector is the projection of the circumference arc between the initial and reference point. In fact:

$$L_1 = 2R\sin(\eta) \qquad (5.14)$$

So, since the centripetal acceleration is:

$$a_c = a_{s_{cmd}} = \frac{V^2}{R} = 2\frac{V^2}{L_1}\sin(\eta) \tag{5.15}$$

The last part of this latter equation is the angle η, considered with a small magnitude and constituted by two parts, so defined:

$$\begin{cases} \sin(\eta) \approx \eta = \eta_1 + \eta_2 \\ \eta_1 \approx \frac{d}{L_1} \\ \eta_2 \approx \frac{\dot{d}}{V} \end{cases} \tag{5.16}$$

This model results in a PD structure for the cross-track error (equation (5.17)),

$$a_{s_{cmd}} \approx 2\frac{V_{TAS}}{L_1}\left(\dot{d} + \frac{V_{TAS}}{L_1}d\right) \tag{5.17}$$

and has to be tuned according to the factor $\frac{L1}{V}$. In the case of a straight line, it is properly working, but it needs further modifications for any other case, like a more complex perturbed non-straight line or a circular path, increasing the number of necessary parameters for the tuning. For this reason, it was chosen to follow a different and more general approach, explained below.

5.6.2   Geometric algorithm

The final guidance algorithm is based on geometric relationships instead of physical equations and uses fewer parameters than the previous model.

Zero-crossing

Firstly, a notation remark needs to be done to avoid zero-crossing errors and to protect every variable which is defined in a limited range, such as angles between $[0\ 2\pi]$ rad. Every time variables such as χ and Ψ are going from a value next to 0 and below, they will jump and continue from 2π (and vice versa). To avoid this, a subsystem is applied to each of these signals to detect the trend of the signal (increasing or decreasing from 2π or 0 respectively), and depending on the case, it will add or subtract 2π (or π for the variations). Then, if the signal decreases from zero, it will become negative, otherwise, if it is increasing beyond 2π it will be extended. Wherever applicable, the numerical derivative building is then performed subsequently avoiding.

Model

The complete representation of the geometric configuration is shown in figure 5.28. As a beginning, the point O is the origin of the inertial axes (x_o and y_o), which is located at the initial position of the aircraft at simulation startup. The *North* and *East* directions are shown in the typical arrangement used for
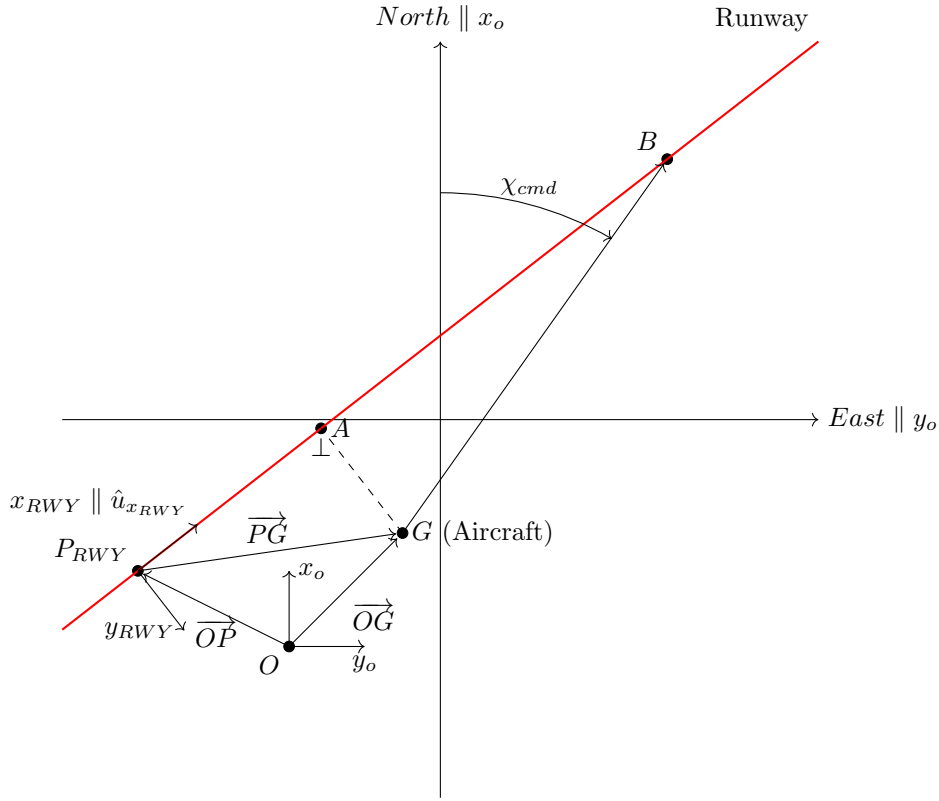
Figure 5.28: Geometric guidance scheme

the plots. Independently from these two latter, the runway has its centreline highlighted in red and its beginning point P_{RWY}. The main element is point G, representing the aircraft, and consequently its projection along the runway through point A.

Some relations are occurring between the different segments, among which:

$$
\begin{cases}
\overrightarrow{OG} = \overrightarrow{OP} + \overrightarrow{PG} \\
\overrightarrow{PA} = (\overrightarrow{PG} \cdot \hat{u}_{x_{RWY}}) \cdot \hat{u}_{x_{RWY}} \\
\overrightarrow{AB} \triangleq L_{ah}
\end{cases}
\tag{5.18}
$$

Following the order: $\overrightarrow{OP}$ represents the position of the runway in the inertial frame, $\overrightarrow{PG}$ represents the position of the HAP with respect to the runway frame, $\overrightarrow{OG}$ is the absolute position of the vehicle, x_{RWY} and y_{RWY} are the runway frame, $\hat{u}_{x_{RWY}}$ is the unit vector of the runway longitudinal axis and the vector $\overrightarrow{AB}$ is from now designed as L_{ah}, which stands for lookahead distance.

The algorithm is based on a simple comparison between the projection of the longitudinal coordinate A and the expected straight following coordinated B. So, by fixing the L_{ah}, it is possible to know the projection of the HAP along the runway (with respect to any desired reference frame) and translate it into a new track angle/heading command, by computing the angle between the $North$ axes and the $\overrightarrow{GB}$

vector, as shown in the figure with Ψ_{cmd}, which in this case will be χ_{cmd}. The process is:

$$
\begin{cases}
A = P_{RWY} + \overrightarrow{PA} = P_{RWY} + (\overrightarrow{PG} \cdot \hat{u}_{x_{RWY}}) \cdot \hat{u}_{x_{RWY}} \\
B = A + L_{ah} \cdot \hat{u}_{x_{RWY}} \\
\chi_{cmd} = \arccos\left(\frac{\overrightarrow{x_o} \cdot \overrightarrow{GB}}{||\overrightarrow{x_o}|| \cdot ||\overrightarrow{GB}||} \right)
\end{cases}
\tag{5.19}
$$

Here, the only parameter which needs to be chosen is L_{ah}, which can be easily assumed as an inverse proportional gain. In fact, the smaller it is the more aggressive the action will be while trying to reach a closer point. From this perspective, a clear limitation is imposed by the virtual limit value of L_{ah}, which is zero. In this case, the commanded input would not be followed by the HAP due to the high imposed rate of turn. On the other hand, a too-high value of the distance would result in a weak input, too slow to match with the updated position, because just a little increment would be added every iteration.

In this study, an infinite runway length is assumed for simplicity, enabling the maintenance of a constant lookahead distance. However, in practical scenarios, runways have finite lengths, necessitating a more flexible approach. When dealing with finite runways, adjusting the lookahead distance based on factors such as runway length, aircraft characteristics, and guidance requirements or expected performances becomes necessary. This ensures that the analyses accurately reflect real-world constraints and requirements, enhancing the reliability and relevance of the findings.

5.7   Final lateral controller

To summarise all the improvements made to the original controller, the table 5.7 shows all its features developed to address the major addressed challenges. Even if the lateral controller is not the main focus of this work, it plays a crucial role in the following parts, where it will be integrated into the landing controller, and many landing simulations will be executed.

Table 5.7: Features of the lateral controller

Issue	Solution
Noisy signals	2nd order filters
Stability	Derivative terms
Integral windup	Saturation
Zero crossing	Range extension

5.8   Parameters

To conclude this chapter, a summary of all the technical specifications of the guidance algorithm and the lateral controller is provided, showing the numerical values of the different parameters.

5.8.1 Guidance

Table 5.8 shows the few parameters of the guidance algorithm.

Table 5.8: Guidance algorithm summary table

Category	Origin Point	Coordinates	
Reference frames	O	$(0,0)$	
	P_{RWY}	$(0,0)$	
Category	Symbol	Value	Unit
Parameters	L_{ah}	200	m

5.8.2 Controller

For the controller, many parameters are part of it, and then they are divided by subparts to ease the reading, summarising all the values in table 5.9.

5.9 Responses

Before the extensive simulation campaign, an example of the obtained results is reported, where different initial conditions are set, in order to evaluate the response of a more complex manoeuvre, like the aircraft flying in the opposite direction of the runway.

Here, two cases are examined:

- **First**: straight flight, with the complete wind disturbance.

- **Second**: Guidance of the aircraft initially flying in the opposite direction, without the wind disturbance.

5.9.1 First example

This first example uses the same disturbances as for all the previous controllers, and it is shown to demonstrate the final achieved conditions of the updated lateral controller.

First of all, the trajectory of the vehicle is shown in figure 5.29, where at the very last point, the lateral offset is less than 1 m. Within this work the landing on a runway from a piloting point of view is aimed at, therefore this rather lengthy time until the steady-state error is completely eliminated, is acceptable.

To have a clearer vision of the complete trajectory, figure 5.30 shows the same trajectory with the equal axes option. Here, it is much more clear how well the controller is performing, keeping the vehicle almost in a straight line.

Table 5.9: Final controller summary table

Part	Channel	Symbol	Value	Unit
Feedback rates	χ	K_χ	0.22	1/s
		$\dot{\chi}_{c,sat}$	± 0.436	rad/s
	β	K_β	0.22	1/s
		$\dot{\beta}_{c,sat}$	± 0.175	rad/s
Part	Channel	Symbol	Value	Unit
Filters	χ	$\dot{\chi}_{sat}$	-	-
	β	$\dot{\beta}_{sat}$	± 0.75	rad/s
Part	Channel	Symbol	Value	Unit
Mixing structure	χ	K_{RP_χ}	0.75	-
		K_{RI_χ}	0.75	1/s
		$K_{RI,\chi_{sat}}$	± 0.1	rad
		K_{YP_χ}	1	-
		K_{YI_χ}	0.5	1/s
		$K_{YP,\chi_{sat}}$	± 0.1	rad/s
		$K_{YI,\chi_{sat}}$	± 0.02	rad
	β	K_{RP_β}	0.1	-
		K_{RI_β}	0.5	1/s
		$K_{RI,\beta_{sat}}$	± 0.1	rad
		K_{YP_β}	0.1	-
		K_{YI_β}	0.2	1/s
		$K_{YP,\beta_{sat}}$	± 0.02	rad
Part	Channel	Symbol	Value	Unit
Inner loop	χ	$\Phi_{c,sat}$	± 0.052	rad
		K_Φ	0.5	1/s
Part	Channel	Symbol	Value	Unit
Outer loop	χ	K_{P_p}	1.5	s
		K_{D_p}	0.025	s^2
	β	K_{P_r}	-1.5	s
		K_{D_r}	-0.025	s^2
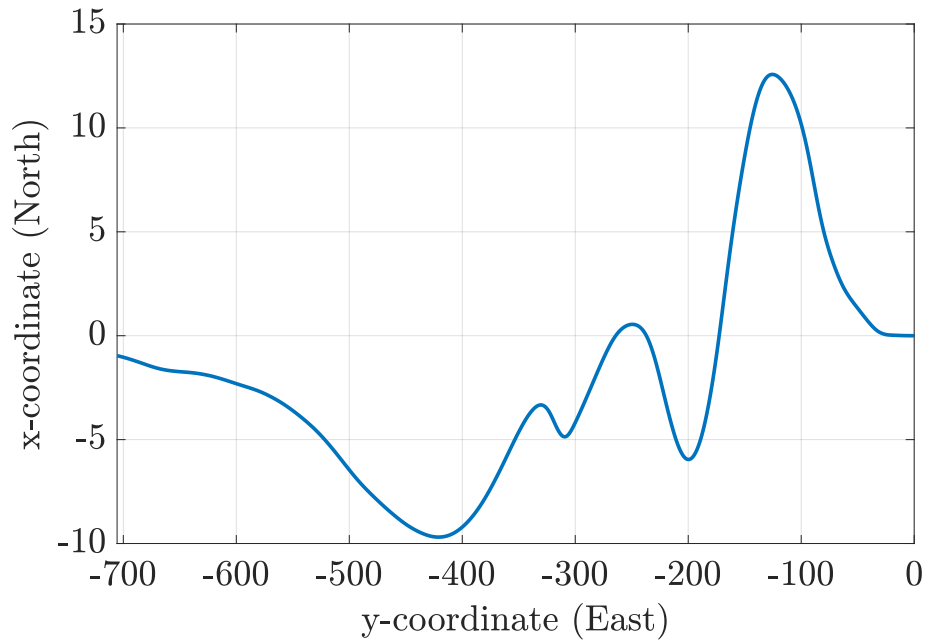
Figure 5.29: x-y trajectory (final controller)
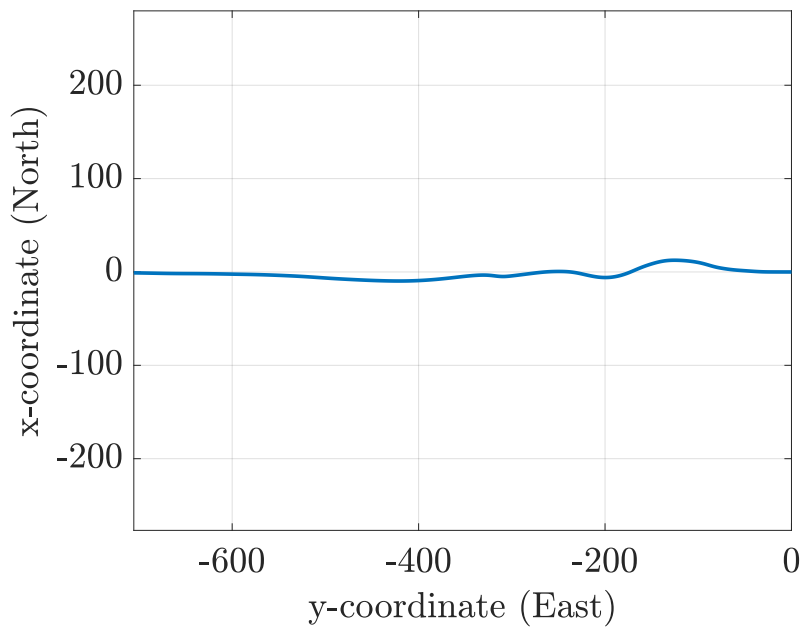
Figure 5.30: x-y trajectory (final controller), with the equal axes

Then, figure 5.31, displays the two controlled variables, which respond promptly to the disturbances and then return towards the commanded value.
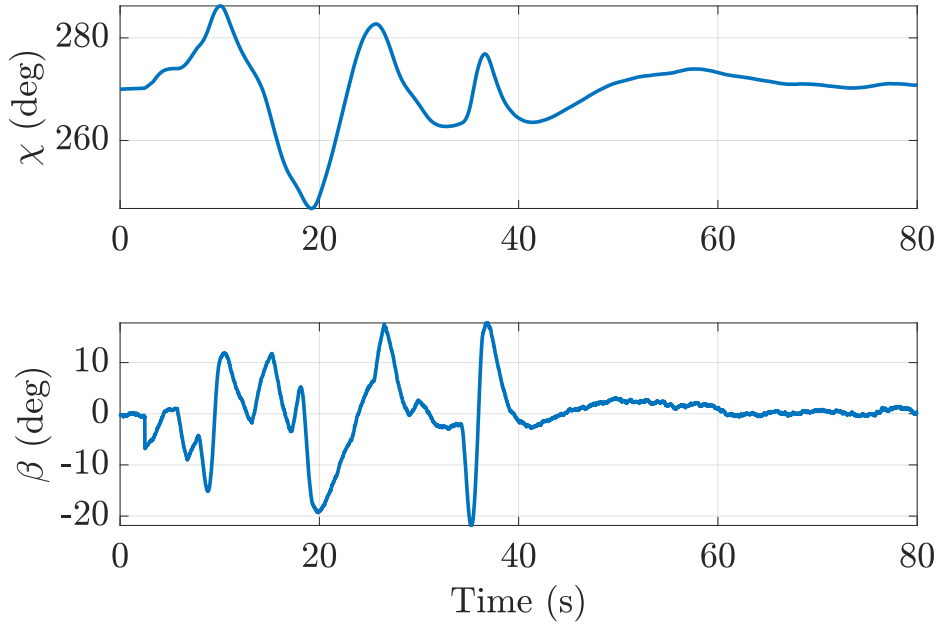
Figure 5.31: $\chi - \beta$ plot (final controller)

Finally, the variables plot (figure 5.32) shows very good behaviour for all of them, highlighting how the controller can keep the vehicle on track, even with severe disturbances. It is worth mentioning that the control surfaces never enter saturation and sideslip and rotational rates are, given the high magnitude of the wind disturbances, comparatively low.

5.9.2 Second example

For the second example, a different case is examined, namely, a guidance manoeuvre is commanded, starting from a different initial positioning of the vehicle. In particular, the Ψ_{trim} value is set to $100°$, instead of the usual $270°$. In addition, the time duration of the simulation is incremented to 120 s, since the manoeuvre requires a slow but total turn in the opposite direction.

As shown in figure 5.33, the vehicle is starting the simulation in the origin, with a different initial heading, and the guidance algorithm conducts it towards the aimed track angle. At the end of the simulation, the lateral cross-track error is around 3 m with respect to the centreline of the runway.

Figure 5.35 clearly shows the action of the driving algorithm on the variable χ. This starts from a value of $100°$, while it is commanded to reach $270°$. A slight overshoot characterises the reaching and exceeding of the designated value, but thanks to the saturation of the integrators in the controller, it is minimised and allows the final value to be reached stably.

Figure 5.34 shows the time histories of the most important variables, with a null wind input (only the
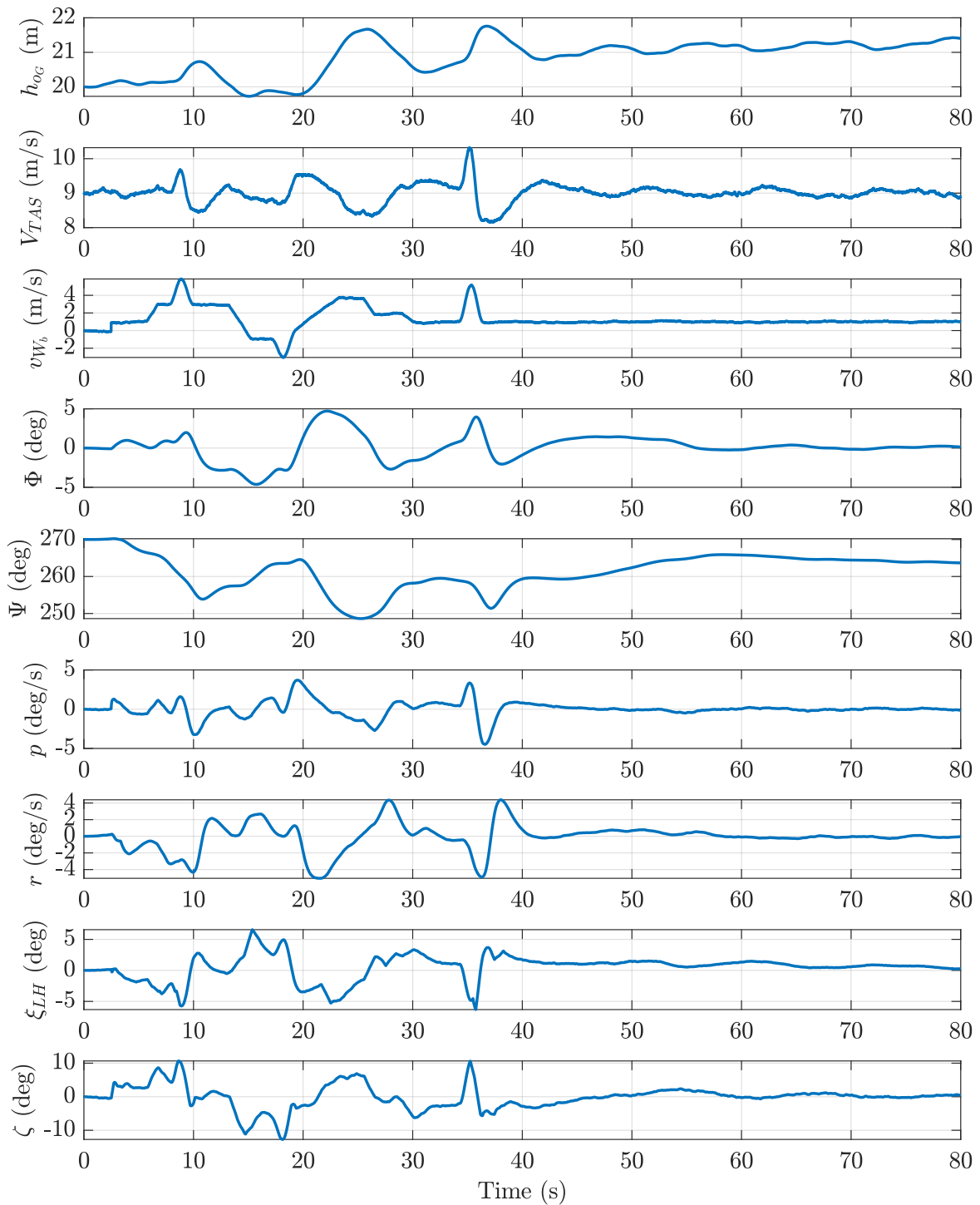
Figure 5.32: Time histories (final controller)
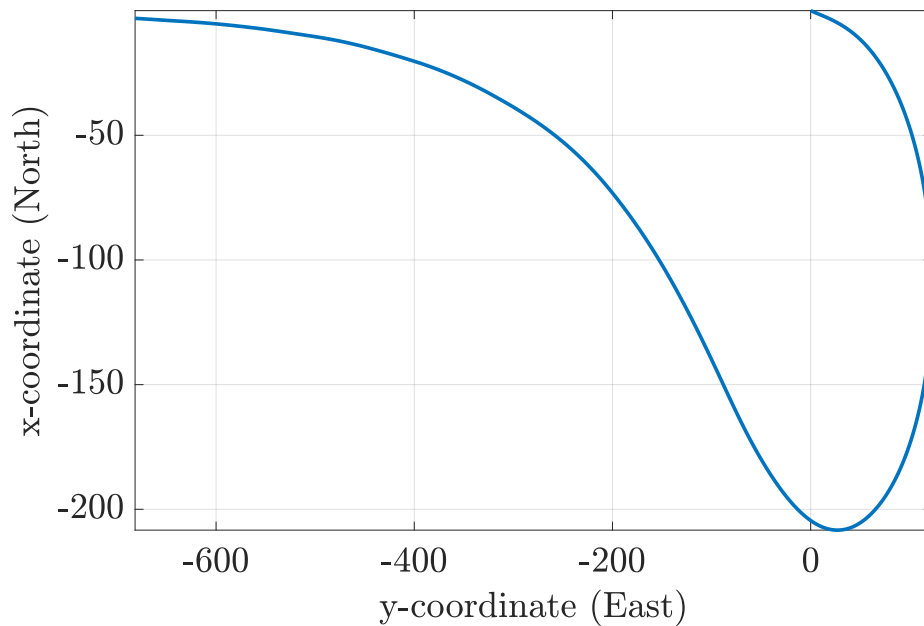
Figure 5.33: x-y trajectory (guidance manoeuvre)

turbulence is present).

Here, the Ψ angle follows the target track angle, stabilising to a correct final value, while the Φ angle reaches the maximum bank angle at 6 deg, and then it comes back to 0, showing that the commanded turn is not very steep, as desired for the HAP aircraft. This can also be seen in the control surface plots. The rudder deflection is mainly at around 5 deg during the turn, which is not a large value for the HAP aircraft.
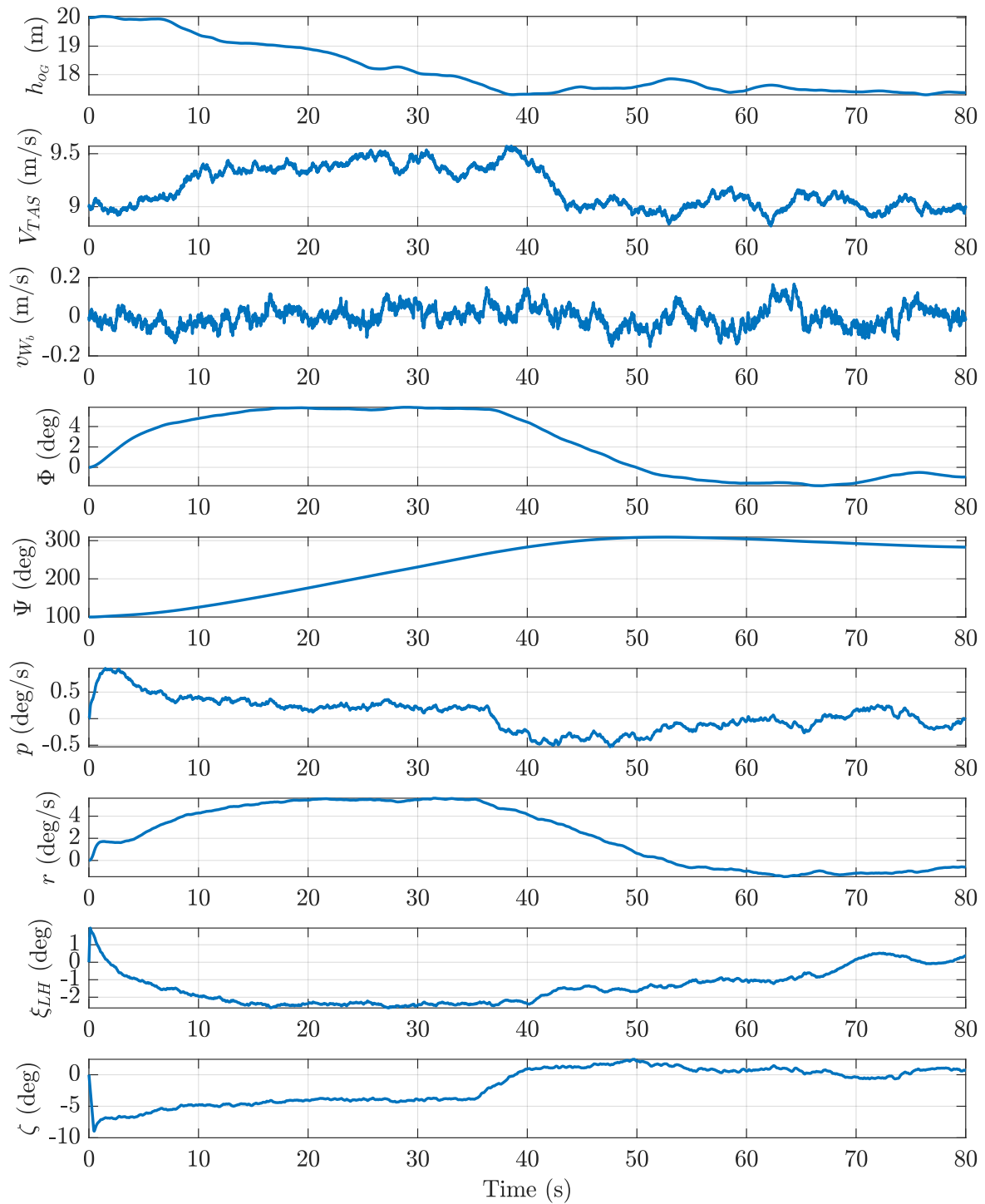
Figure 5.34: Time histories (guidance manoeuvre)
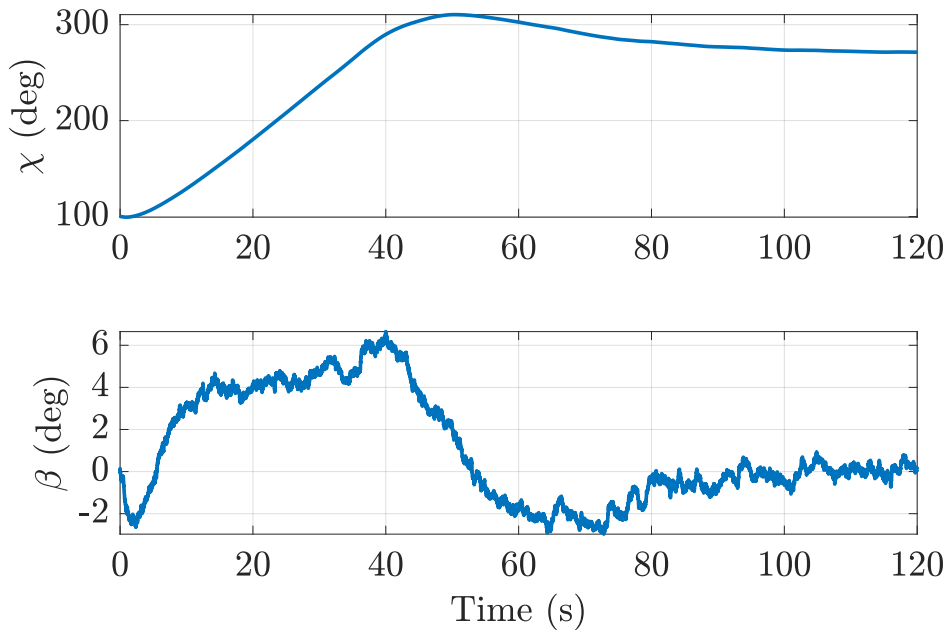
Figure 5.35: $\chi - \beta$ plot (guidance manoeuvre)

Chapter 6

Setup for the landing simulations

With this chapter, the second part of the work begins. Once all the technical data are computed, the actual simulation process can take place. To do this, which will be done in the next chapters, a setup process is necessary to have a solid basis for the correct progress of the work.

6.1 Purpose of the landing simulations

As already mentioned in section 1.1, the ultimate aim of this work is to evaluate the landing capabilities of the DLR HAP aircraft, also considering the limitations in different operating situations, consisting of different wind types. To summarise, different evaluations and studies will be needed to determine the limit cases for different types of wind. These will be proposed, used, analysed and evaluated to obtain a significant amount of data useful both for final evaluations and for future insights and improvements.

6.2 Turbulence model

The first part of the setup consists in describing the adopted turbulence model, which is not going to be used in the initial results, but directly in the batch simulation process.

The respective wind speeds are modelled for the translational wind components by passing white noise through a filter. The corresponding transfer functions are deducted for each of the three wind components, as well as this section about the turbulence, from [15], and are respectively equal to:

$$H_u(s) = \frac{\sigma_u \sqrt{\frac{L_u}{V_{TAS}}} \left(1 + 0.25 \frac{L_u}{V_{TAS}} s\right)}{1 + 1.357 \frac{L_u}{V_{TAS}} s + 0.1987 \left(\frac{L_u}{V_{TAS}}\right)^2 s^2} \tag{6.1}$$

$$H_v(s) = \frac{\sigma_v \sqrt{\frac{L_v}{V_{TAS}}} \left(1 + 2.7478 \frac{L_v}{V_{TAS}} s + 0.3398 \left(\frac{L_v}{V_{TAS}}\right)^2 s^2\right)}{1 + 2.9958 \frac{L_v}{V_{TAS}} s + 1.9754 \left(\frac{L_v}{V_{TAS}}\right)^2 s^2 + 0.1539 \left(\frac{L_v}{V_{TAS}}\right)^3 s^3} \tag{6.2}$$

$$H_w(s) = \frac{\sigma_w \sqrt{\frac{L_w}{V_{TAS}}} \left(1 + 2.7478 \frac{L_w}{V_{TAS}} s + 0.3398 \left(\frac{L_w}{V_{TAS}} \right)^2 s^2 \right)}{1 + 2.9958 \frac{L_w}{V_{TAS}} s + 1.9754 \left(\frac{L_w}{V_{TAS}} \right)^2 s^2 + 0.1539 \left(\frac{L_w}{V_{TAS}} \right)^3 s^3} \tag{6.3}$$

By following the approximate von Kármán velocity spectra, σ_u, σ_v and σ_w are the standard deviations of the wind velocity for the longitudinal, lateral, and vertical axes, while L_u, L_v and L_w are the corresponding scale lengths.

The resulting values are reported in table 6.1.

Table 6.1: Standard deviations and scale lengths used within this work to model turbulence

Range	Light turbulence			Moderate turbulence			Scale length		
h_{AGL}(m)	σ_u (m/s)	σ_v (m/s)	σ_w (m/s)	σ_u (m/s)	σ_v (m/s)	σ_w (m/s)	L_u (m)	L_v (m)	L_w (m)
$0 - 10$	0.129	0.093	0.065	0.259	0.187	0.129	21	11	5
$10 - 20$	0.144	0.111	0.082	0.289	0.222	0.164	33	19	11
$20 - 30$	0.154	0.123	0.096	0.308	0.246	0.192	43	28	17
$30 - 40$	0.167	0.139	0.115	0.322	0.264	0.212	52	35	23
$40 - 50$	0.172	0.146	0.123	0.334	0.279	0.230	61	42	29
$50 - 60$	0.176	0.152	0.130	0.344	0.292	0.246	68	49	35

6.3 Complete landing procedure

While up to now only the in-flight properties of the aircraft, and in particular the lateral controller, have been analysed, from this chapter onwards, the landing controller will be activated to carry out the actual simulations. This is a previously developed tool, which contemplates an integrated use of the longitudinal controller, which will therefore be briefly explained below. Subsequently, the entire landing procedure will also be described in full, as it is of fundamental importance for setting up future simulations and in particular certain fundamental wind parameters.

6.3.1 Longitudinal controller and landing controller

For this part, everything exposed here comes from [15], starting with the aim of the longitudinal controller, and ending up with the actual structure of the landing controller.

Since the HAP won't have a radar altimeter due to weight considerations, the HAP needs to be landed manually. In these simulations, however, the controller emulates a pilot controlling the aircraft remotely. Key considerations include applying lower frequency control inputs, simple commands, and utilizing flight parameters accessible to the pilot (such as airspeed, pitch angle, and height above ground). Then, the landing controller comprises two nested loops: an outer loop for energy management, inspired by the Total Energy Control System (TECS) philosophy ([25] and [22]), and an inner loop for pitch control combined

with an inverse thrust model, which converts thrust commands into propeller rotation speed command. While the TECS philosophy remains intact, modifications have been made to enhance performance.
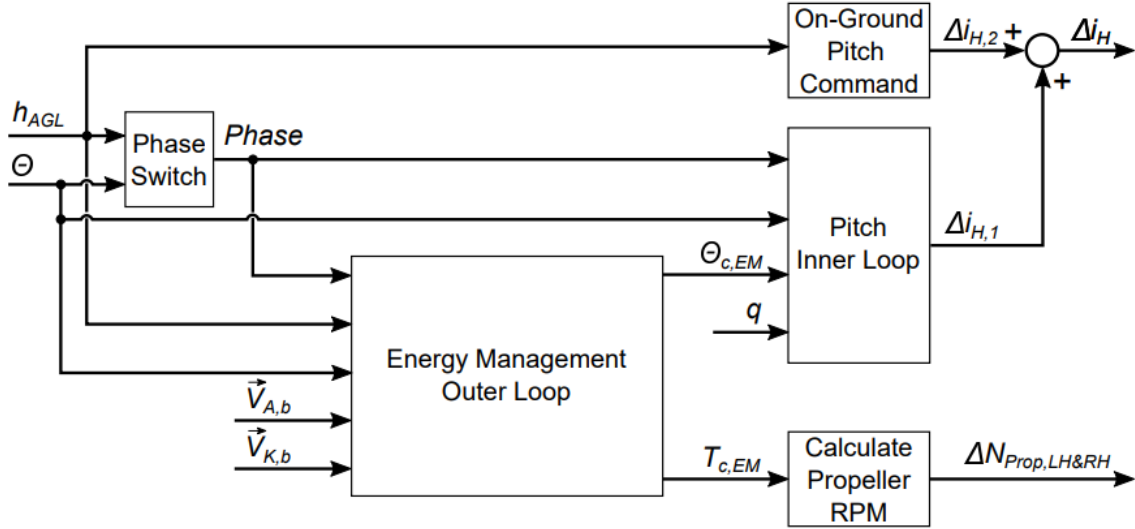
Figure 6.1: Block diagram of the landing controller [15]

Figure 6.1 shows the block diagram of the landing controller, highlighting the previously discussed features. The primary goal of the controller discussed here, as will be explained later (6.3.2), is to assist in creating a procedure that minimizes the overall risk of causing harm to the vehicle during the landing process. This includes mitigating the potential for issues like hard landings, the payload compartment making contact with the ground, or the initial touchdown occurring on a skid other than the main one.

6.3.2 Landing procedure

The landing of the DLR HAP aircraft poses challenges such as susceptibility to atmospheric disturbances, a low sink rate, skids as landing gear, a narrow pitch angle demand during touchdown, and the need to retract propellers before touchdown, precluding a go-around option post-retraction.

To address these difficulties, a landing procedure has been devised, dividing the process into different phases. A phase manager within the control system, comprising a state machine, determines the current phase of the landing procedure, enabling the control functions to adapt accordingly. This approach ensures that the controller follows reference inputs throughout the various stages of landing, facilitating a smooth transition through each phase.

$$Phase = \begin{cases} 0 & : t < t_{Start} \\ 1 & : t \geq t_{Start} \\ 2 & : |h_{AGL} - h_{``Flare"} \leq \Delta h_{max}| \text{ consecutively for duration } t_h \\ 3 & : |\Theta - \Theta_{Target,TD} \leq \Delta\Theta_{max}| \text{ consecutively for duration } t_\Theta \end{cases} \quad (6.4)$$

A detailed explanation of all the phases, summarised in equation 6.4, is provided below:

- **Phase 1 - Descent and capture of** $h_{"Flare"}$: The landing initiates with a descent to a pre-defined altitude, referred to as $h_{"Flare"}$. This altitude is strategically chosen to provide sufficient ground clearance for engine use and to prevent immediate ground contact due to light gusts. The aircraft maintains $h_{"Flare"}$ for a specified duration before transitioning to phase 2. The simulation begins in stabilised horizontal flight at 10 m above ground, with phase 0 ensuring this condition until $t = t_{Start}$, when phase 1 activates to commence the descent towards $h_{"Flare"}$.

- **Phase 2: Deceleration while maintaining** $h_{"Flare"}$ **and capture of safe pitch attitude** Θ_{Target}: This phase focuses on achieving a safe pitch angle, denoted as Θ_{Target}, to facilitate a smooth touchdown. The primary objective is to ensure the main skid touches down first, requiring precise control due to the narrow allowable pitch band at touchdown. Within this range, a target pitch angle, Θ_{Target}, is defined, favouring a softer limit closer to the maximum allowable pitch angle. This target pitch angle guides the aircraft during touchdown. Throughout this phase, the altitude $h_{"Flare"}$ is maintained as the aircraft decelerates, gradually increasing the angle of attack and pitch angle while maintaining a zero flight path angle. Once the target pitch angle Θ_{Target} is attained, the flight is stabilized and sustained for a specified duration.

- **Phase 3: Depletion of remaining kinetic and potential energy while keeping safe pitch attitude** Θ_{Target}: This critical phase begins with the shutdown of engines, retraction, and locking of propellers parallel to the wing leading edge before approaching the ground. Maintaining Θ_{Target} becomes crucial as the aircraft loses thrust capability, rendering control over the sink rate impossible. As airspeed decreases and the aircraft sinks, both kinetic and potential energies diminish. However, adherence to pitch angle constraints and propeller radius is essential to safely execute this phase, ensuring initiation at a low altitude and employing a suitable Θ_{Target} to prevent excessive sink rates. Despite its importance, this phase poses risks in gusty conditions or system faults, as a go-around maneuver is no longer viable. Upon touchdown of the main skid, a slight stabilizer adjustment prevents payload compartment contact with the ground.

- **Pitch up during slideout**: This concluding action, although not formally designated as a separate phase, plays a vital role in ensuring a safe landing. Upon touchdown, the controller initiates a pitch-up maneuver to mitigate the risk of the payload compartment contacting the ground. This pitch-up must be gentle enough to avoid re-airborne or excessive loads on the tail skid.

After describing the procedure, an example of a complete landing is provided in figure 6.2. Here, all the different controller phases are clearly visible from the specific plot, as well as the limited pitch range ($\Theta_{min,TD}$ and $\Theta_{max,TD}$).

This example provides a complete evaluation of the landing controller behaviour, in the presence of a general turbulence applied to a null wind input, and only with the longitudinal controller. At this point,
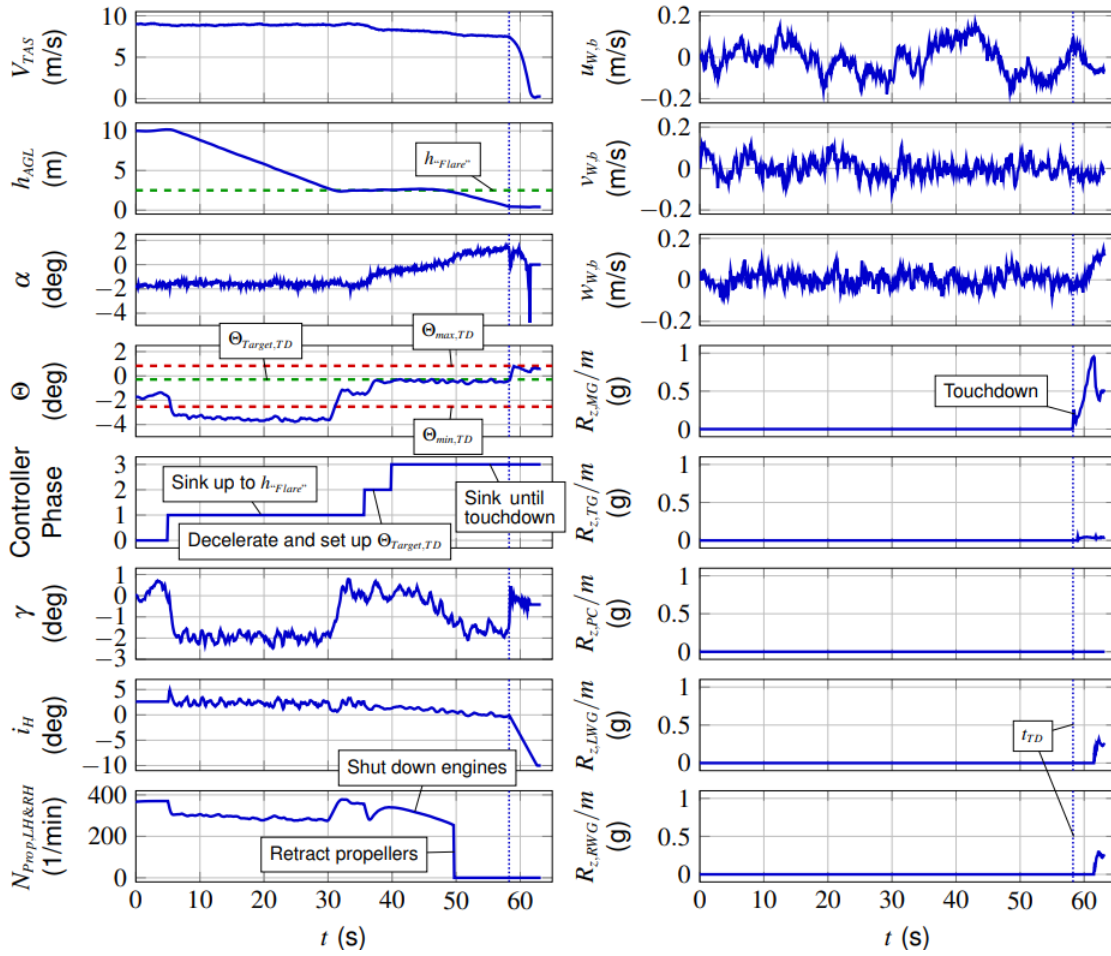
Figure 6.2: Example of landing [15]

after the completion of the lateral controller, this latter has been integrated into the model, and a new wind input generator was developed to test the model according to various features, whose details are presented below.

6.4 External disturbances

Also in this section, the external wind input is the main character, because it constitutes both the primary input to the system and the basis for the subsequent evaluation of the landing capabilities. In particular, a parametric evaluation process will be initiated to be submitted to the model to find out what the limits of the individual input configurations are. Subsequently, these can be combined to highlight the aircraft's capabilities against the worst external conditions. This process is going to be repeated for three singular wind conditions and only for the grass terrain (to adopt a conservative approach).
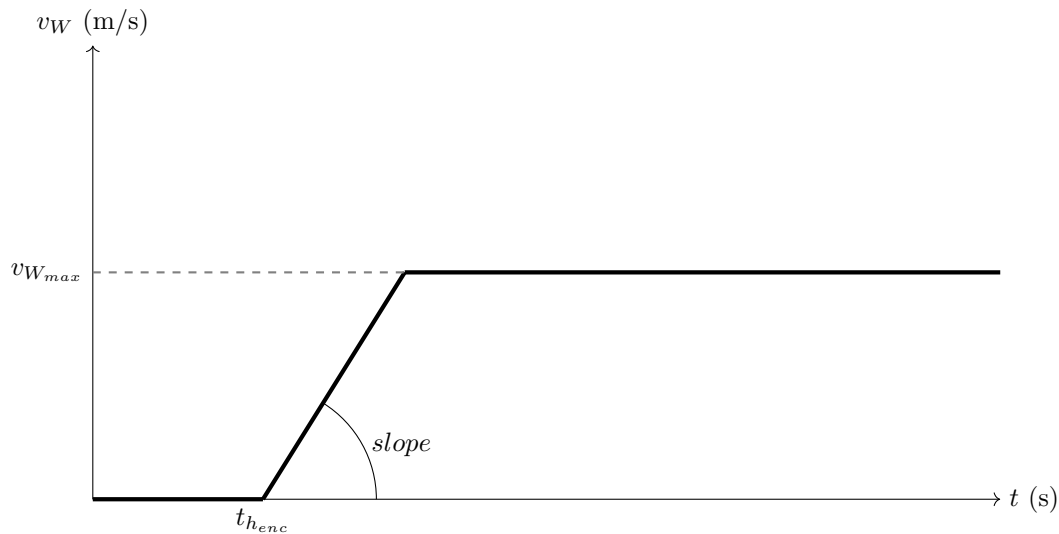
Figure 6.3: Ramp wind input

6.4.1   Height of phase 3

Before starting with the actual explanation, there is the need to explain a specific key parameter of each wind disturbance. It is the h_{enc}, always used to indicate the height of the encounter of the wind disturbance.

The usual default value for all three wind types is referred to as h_{phase_3}, which means that the disturbance hits the vehicle when the landing controller initiates phase 3. So, there is no fixed height (even if it usually is a little bit less than 5 m), but it corresponds to the beginning of the non-propelled flight, just after the flare.

6.4.2   Ramp input

The first wind type is made up of a simple wind ramp, having three specific parameters:

Table 6.2: Ramp parameters

Parameter	Unit	Default Value	Range
h_{enc}	m	h_{phase_3}	$(10, 1)$
$slope$	m/s^2	0.5	$(0.5, 2)$
$v_{W_{max}}$	m/s	1.5	$(0.5, 3)$

The table 6.2 shows the basic configuration of the ramp wind type. The three parameters are the height of encounter of the ramp (h_{enc}), the maximum wind magnitude $v_{W_{max}}$ and the slope of the ramp. To evaluate each of them separately, two are held constant at their default values, while the third varies according to the values in their range. A special value is the default h_{enc}, defined as that at which phase 3 of the landing controller is met.
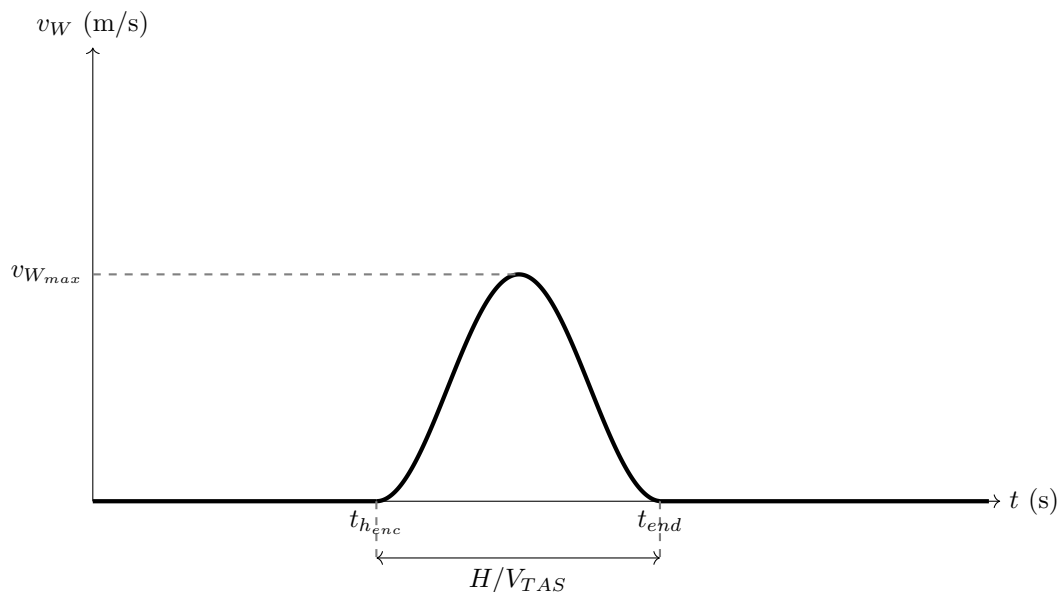
Figure 6.4: Gust wind input

The general shape of any ramp is displayed in figure 6.3, with evidence of all its parameters. The time instant $t_{h_{enc}}$ is the one corresponding to the encounter of the specific height.

6.4.3   Gust input

For the gust, the situation is similar to the previous one, with some differences in the characteristic parameters, shown in table 6.3. Furthermore, as discussed above, the gust is generated following the CS-25 standard.

Table 6.3: Gust parameters

Parameter	Unit	Default Value	Range
h_{enc}	m	h_{phase_3}	$(10, 1)$
H	m	10	$(1, 50)$
$v_{W_{max}}$	m/s	2	$(0.5, 3)$

The general gust input is shown in figure 6.4, with its starting time $t_{h_{enc}}$ (defined by the altitude), its peak value $v_{W_{max}}$ and the wavelength defined as:

$$H = V_{TAS} \cdot (t_{end} - t_{h_{enc}}) \tag{6.5}$$

6.4.4   Shear input

Lastly, the shear input is constituted by two following and symmetric ramps. Then, even if the total number of parameters is six, four of them are variable (the ones of the second ramp plus the magnitude
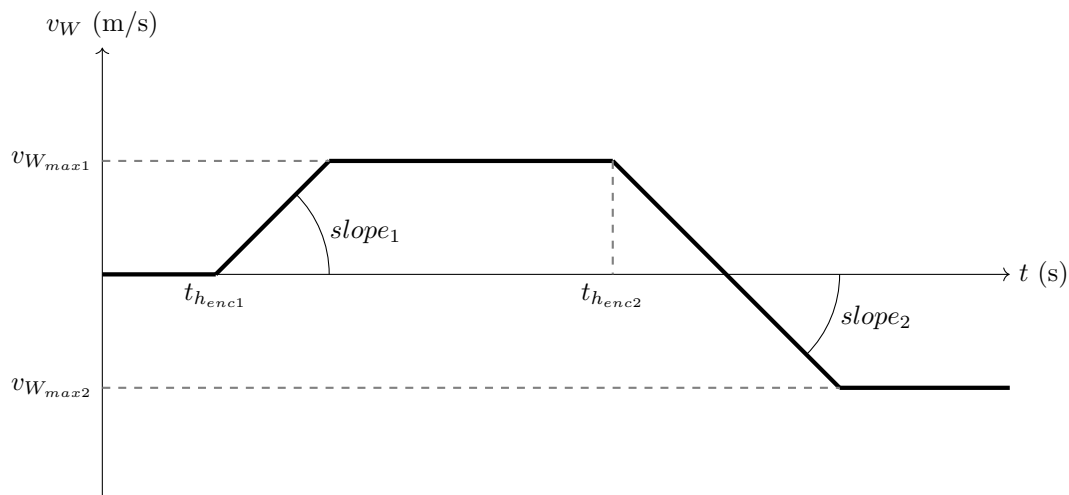
Figure 6.5: Shear wind input

of the first ramp, due to the symmetry of the shear), while the others are fixed. The table 6.4 summarises the different fixed and variable parameters, splitting the first ramp in the top part and the second ramp (the actual shear) in the bottom part of itself. In the end, the image 6.5 displays a general shear input.

Table 6.4: Shear parameters

Parameter	Unit	Default Value	Range
h_{enc1}	m	15	-
$slope_1$	m/s^2	0.5	-
$v_{W_{max1}}$	m/s	2	$(0.5, 3)$
h_{enc2}	m	h_{phase_3}	$(10, 1)$
$slope_2$	m/s^2	-0.5	$-(0.5, 2.5)$
$v_{W_{max2}}$	m/s	$-v_{W_{max1}}$	$-v_{W_{max1}}$

6.5   Setup for the test cases

Following the technical explanation of the new inputs for the model, a MATLAB script is created to execute a loop on the Simulink model, allowing one to choose which parameter to analyse.

In this way, it is possible to validate one type of wind each time, varying its parameters one by one, thus performing a complete parametric study that tests all possible combinations. Furthermore, it should be mentioned that all simulations in this part of the work are carried out without the effects of turbulence so that only the effect of the wind type is investigated. Later, the latter will also be introduced for a statistical evaluation of the overall landing capabilities.

6.6 Evaluation criteria and limits

Additionally, it is necessary to draw up a list of evaluation criteria to be used both to refine the simulative infrastructure and to proceed with evaluations of the landing capabilities.

6.6.1 Lateral deviation

The most obvious limit for the landing is the width of the runway. Without considering the terrain properties (like the composition of the asphalt) a general assumption of 30 m for the total width is made. Respecting that the wing skids are located at 8 m to each side from the aircraft centreline, a maximum offset of 7 m is acceptable. Including another 2 m as a safety margin yields 5 m of maximum allowable offset.

This means that the specific evaluation criterion for the lateral offset is satisfied when:

$$|x_o(t_{ldng})| \leq 5 \ m \tag{6.6}$$

Here, x_o is the absolute lateral offset from the runway which is assumed to be located at $y_o = 0m$ and pointing West, and t_{ldng} is the touchdown time instant.

6.6.2 Loads

Regarding the loads, the situation is diversified for each skid. Each of them has a different role, position and impact resistance capacity. In any case, after some engineering judgment, taking qualitative structural considerations into account, the proposed and adopted are the ones in table 6.5.

Table 6.5: Loads landing criteria

Skid	Maximum allowable value (g)
Left wing gear	0.5
Right wing gear	0.5
Main gear	1.5
Tail gear	0.5
Payload compartment	0

The most strict is constituted by the payload compartment, which cannot touch the ground due to the presence of the instrumentation.

An important clarification is necessary here. Due to the non-linear nature of the simulation model, particularly about the interaction between the wing skids and terrain, as well as the difficult definition of viscous element damping and the absence of distributed masses, it is difficult to assess the maximum value of each skid load.

In particular, given the low level of damping, it is not difficult to find time histories of accelerations

consisting of several rebounds, alternating with zero values (i.e. no ground contact). This situation is realistically implausible, which is why, rather than using the absolute maximum of the single acceleration as a comparison value, a function was developed to identify the most plausible maximum value, based on several parameters, and thus excludes e.g. cases in which one wing landing gear touches down, leading to an excess roll rate, which in turn causes the other wing gear to touch down with a higher load. These include the absolute value of the first spike, its relative distance from the absolute maximum and the time duration of the latter (in the case of a bell shape).

The final result allows to obtain the correct value of the maximum of each acceleration, and then compare it against the maximum allowed value. This function is used only for three different skids, namely the left wing gear (LWG), the right wing gear (RWG) and the tail gear (TG).

6.6.3   Main gear liftoff

The last criterion is a qualitative one, stating that the main gear (MG) should never lift off the ground after the touchdown. Since it is usually the main gear that makes the touchdown first, the occurrence of the above-mentioned condition is crucial.

One factor above all that could affect this condition is the ground effect, accentuated by the large wing surface in combination with a hard landing and rapid pitch-up motions leading to a re-increase of lift.

Chapter 7

Parameter study, simulation process, results analysis and landing capabilities assessment

This chapter firstly deals with the presentation of all the initial results, meaning the ones coming from the parameter analysis, as well as with the steady-state analysis, the determination of limiting cases and the evaluation of these with batch analyses

7.1 Steady-state maximum crab angle

To begin with, it is useful to express the results regarding the maximum crab angle allowed in steady-state conditions. This concerns the first real operational limit, as it constitutes the maximum angle with which the vehicle can approach the runway, starting from an already stabilised condition.

To do so, the search for this value was carried out with turbulence-free landing simulations, with a ramp-type disturbance of variable (increasing) intensity, encountered at an altitude of 25 metres, well before landing, to arrive there in a totally stabilised manner, and starting from an initial altitude of 30 metres. In addition, 3 different soil types were tested, summarised in the table 7.1

Table 7.1: Types of terrain for the steady-state maximum crab angle

Type #	Base	μ_x	μ_y
1	Grass	Model	
2	Tarmac	0.3	0.3
3	Tarmac	0.3	0.4

To better explain the developed process, figure 7.1 shows an example of a plot containing the different

values of the maximum loads in relation to the applied disturbance, as a function of the increasing intensity of the latter. In this case, the chosen terrain is number 3.
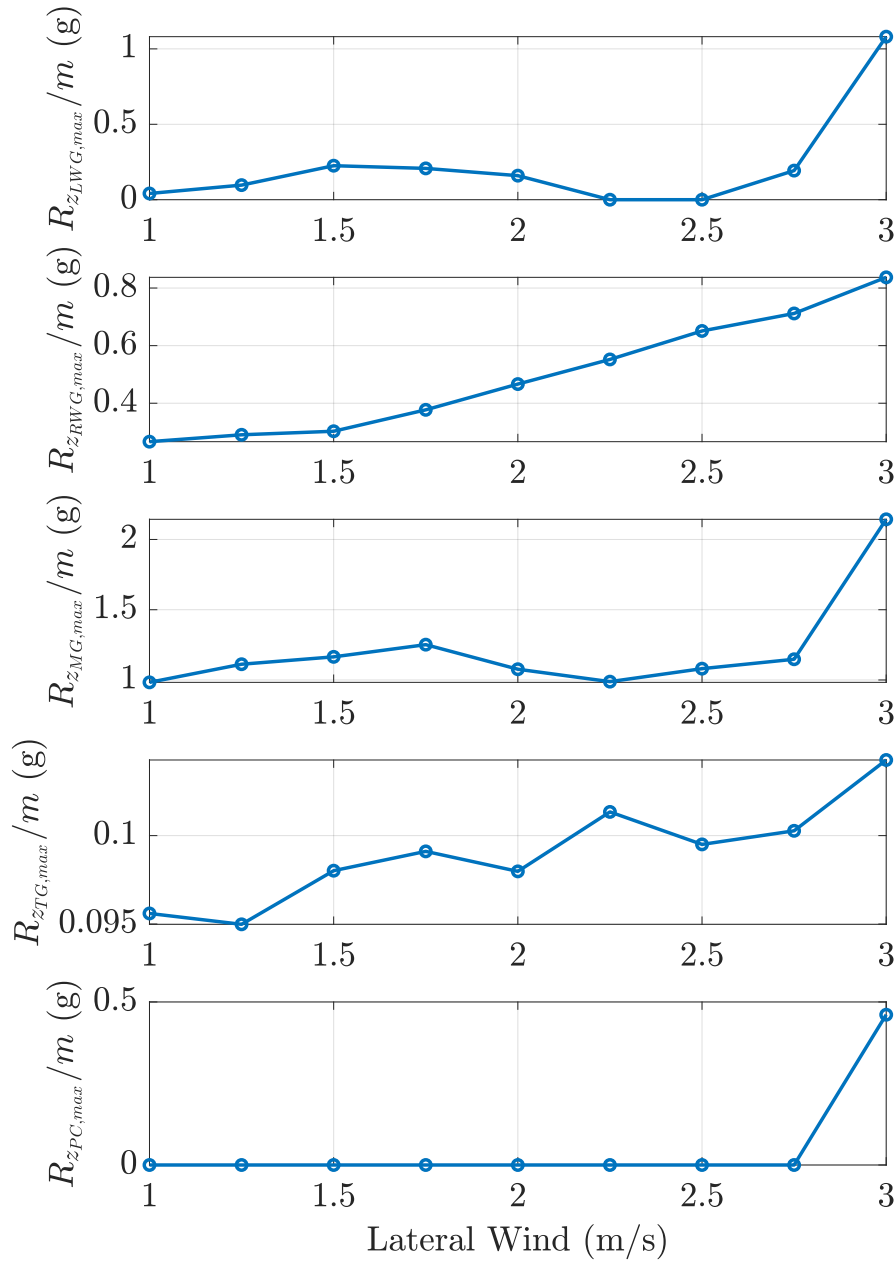
Figure 7.1: Loads with respect to the steady state ramp disturbance for the terrain type #3

It is easy to evaluate that the maximum allowable velocity in this case is 2 m/s. Then, by computing the crab angle, defined as in equation 7.1, it is possible to evaluate the maximum correspondent crab angle.

$$\text{crab} = \chi(t_{lndg}) - \Psi(t_{lndg}) \tag{7.1}$$

An example graph is shown in figure 7.2. Here we can see the crab angle calculated at the instant of touchdown, as a function of the maximum value of the disturbance. Thus, by intercepting the limiting value, which was previously identified as 2 m/s, the corresponding maximum crab angle is 15.44°.
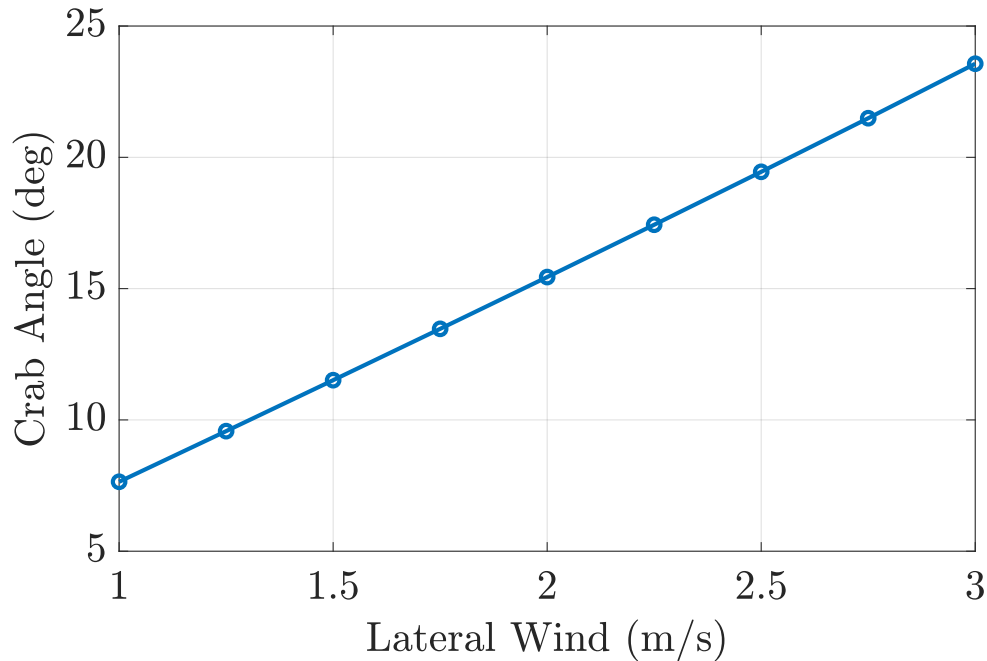
Figure 7.2: Crab angles with respect to the maximum magnitude of the lateral wind for the case #3

To summarise, the table 7.2 shows all three cases, with their corresponding maximum crab angle. This value is of crucial importance since, while in this work it has always been the ambition to cancel out the sideslip angle, it may be necessary to fly with a residual value of the latter to counteract the excessively strong wind disturbances.

Table 7.2: Maximum crab angle for the different terrains options

Type #	$v_{W_{max}}$ (m/s)	crab_{max} (deg)
1	1.75	13.47
2	2.25	17.43
3	2	15.44

It can be seen that the maximum crab values are inversely proportional to the amount of ground friction. While the grass presents the greatest amount of friction, and consequently a lower crab value is allowed to avoid the risk of rollover on the runway, the tarmac with a constant value of 0.3 for the two coefficients of friction is less stringent and allows for landings with acceptable loads even with higher values of crab angle.

7.2 Parameter study and results

From now on, an extensive parameter study will be conducted, to parameterise each wind type according to its characteristic quantities, in order to obtain a complete evaluation of the results (both trajectories and landing loads) for all combinations within the variation ranges of the individual parameters, expressed in 6.2, 6.3 and 6.4.

For every wind type, different visualisations are reported in the following sections:

- **xy plot**: Globally, three graphs (one for each wind input) were made to show the trend of the xy spatial coordinates.

- **Loads plot**: In total, five plots are created for each of the three wind types (15 in total for each input) to show the vertical accelerations of every skid (left wing gear, right wing gear, main gear, tail gear) and payload compartment from the touchdown to the ending time instant of the simulation.

It is important to note that since there are several, only the most important figures will be shown, as each one of them follows the same structure.

7.2.1 Ramp

Some indications for a better reading of the following plots include: the h_{enc} parameter is always indicated in meters, except for the h_{phase_3}, which is always different, the slope is always in m/s^2, while the maximum value is in m/s. Also, every plot presents some peculiar points marked with different symbols:

- **First circle from the right**: beginning of the ramp.

- **Second circle from the right**: ending of the ramp, meaning the linear part of it.

- **Cross**: touchdown.

The figure 7.3 shows that there is a major difference between the h_{enc} above 5 m and those below. In fact, due to the particular flight profile (and in particular to phase 3 of the landing), the aircraft starts with a controlled descent within h_{phase_1}, then stabilises at the specific Θ_{target} within h_{phase_2} and then glides towards the ground. Consequently, a disturbance encountered before 5 m altitude (or in any case before the altitude at which phase 3 of the landing is activated) can be handled without particular difficulty, whereas if it is encountered afterwards, there is the risk that there will not be enough time to return towards the centre of the runway, as happens for example with h_{enc} of 3 and 4 m.

On the other hand, both the the two other ramp parameters have a more linear influence on the lateral trajectory, as expected. From figure 7.4 it is clear that the slope has quite weak conditioning concerning the touchdown lateral offset, while the maximum value can be discerned between a safe landing and a missed runway, as visible from figure 7.5.

Figure 7.3: x-y trajectory with respect to the height of encounter of the ramp

Figure 7.4: x-y trajectory with respect to the slope of the ramp

Figure 7.5: x-y trajectory with respect to the maximum value of the ramp

7.2.2 Gust

Here again, the indications for a better reading of the following plots include: the h_{enc} parameter is always indicated in meters, except for the h_{phase_3}, which is always different, the wavelength (H) is always in m, and the maximum value is in m/s. Also, every plot presents some peculiar points marked with different symbols:

- **First circle from the right**: beginning of the gust.

- **Second circle from the right**: peak of the gust.

- **Third circle from the right**: ending of the gust.

- **Cross**: touchdown.

As previously discussed for the ramp, the gust has a similar trend regarding the h_{enc}. There is a clear window where the disturbance hits the most on the final output, ranging from 2 to 4 m as in figure 7.6. Also for the two other parameters, in figures 7.7 and 7.8, the dependence is mostly linear, and particularly weak for the peak of the gust.

Altogether, the lateral gust perturbation only has a minor influence on the lateral offset during touchdown since it rather leads to a dynamic excitation of the aircraft than to a substantial drift due to the short time the wind is present.
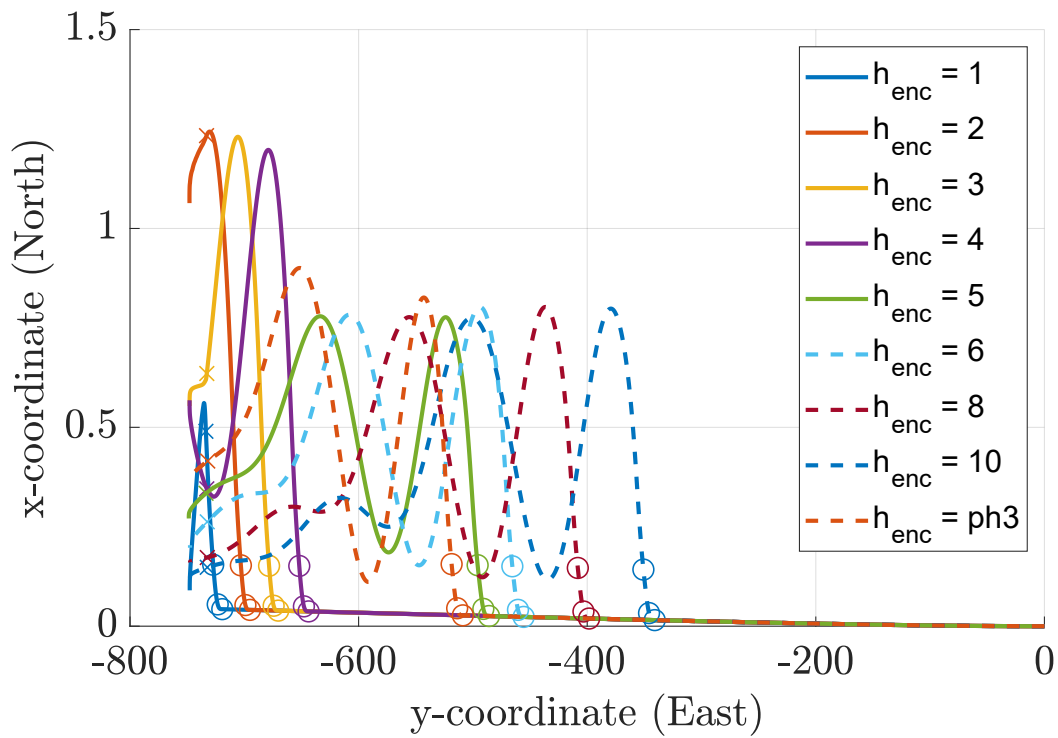
Figure 7.6: x-y trajectory with respect to the height of encounter of the gust
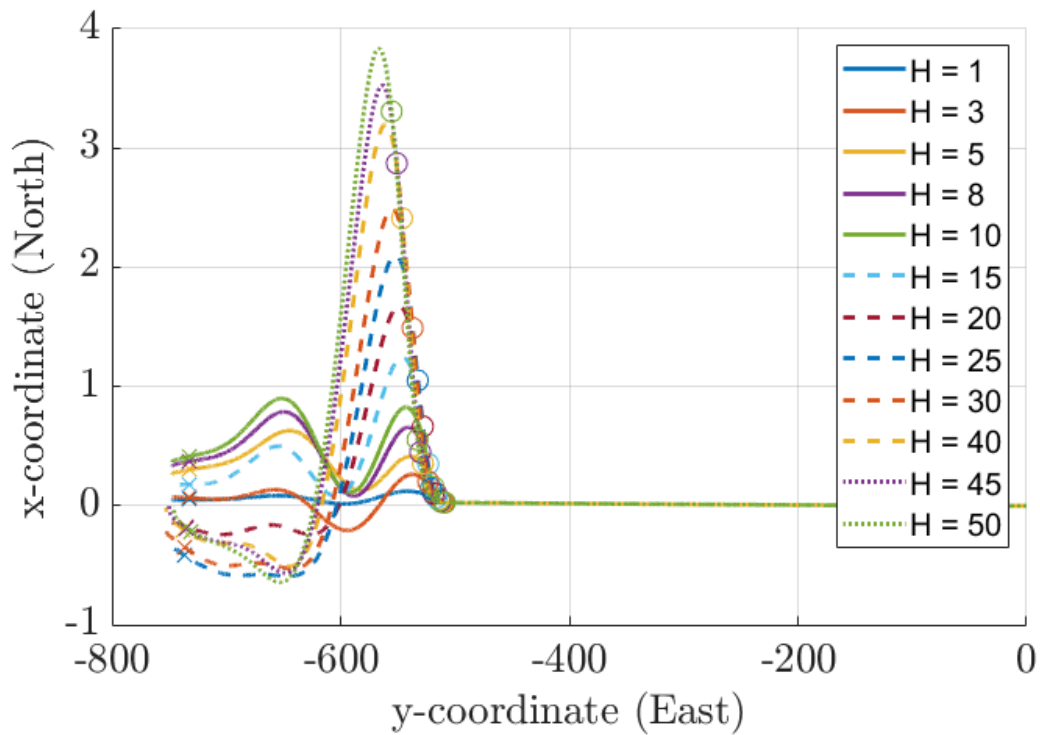
Figure 7.7: x-y trajectory with respect to the wavelength of the gust
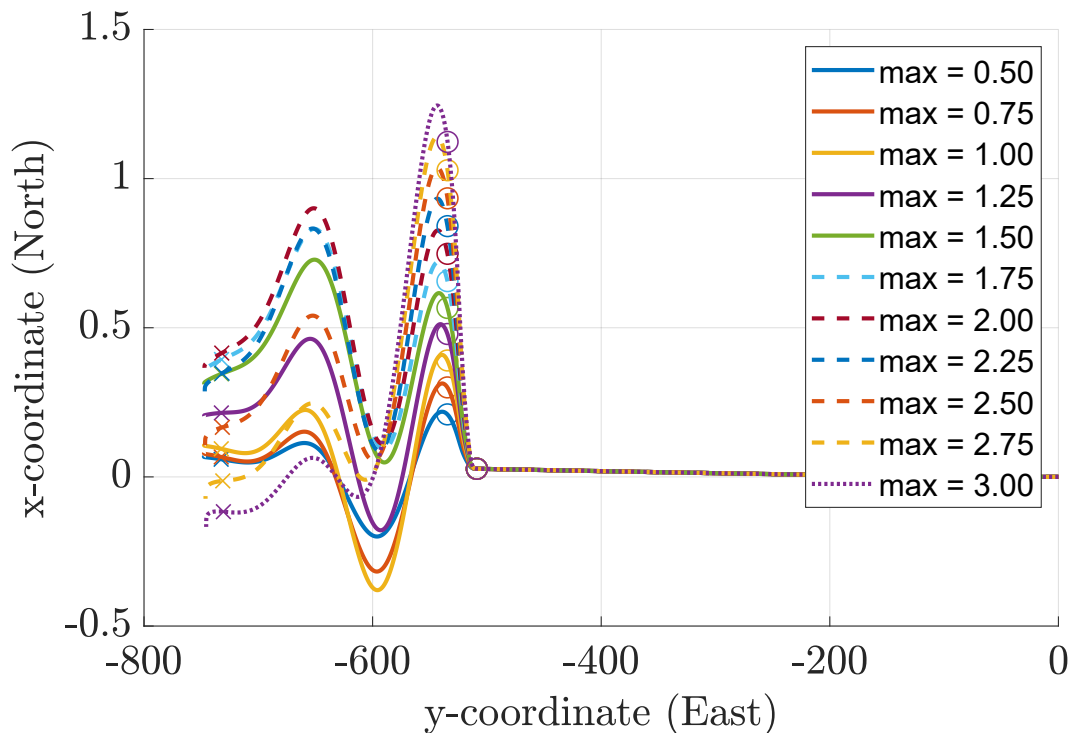
Figure 7.8: x-y trajectory with respect to the maximum value of the gust

7.2.3 Shear

Lastly, for the shear input: the h_{enc} parameter is always indicated in meters, except for the h_{phase_3}, which is always different, while the maximum value is in m/s, and the slope is in m/s^2. For all the cases where the shear is the interested wind type, its parameters are always referred to as the second part of the shear (for the height of the encounter and the slope), while the maximum value is symmetrical (opposite in sign) to the one of the first ramp of the shear. The specific points represent:

- **First circle from the right**: beginning of the shear (second ramp).

- **Second circle from the right**: ending of the shear (second ramp).

- **Cross**: touchdown.

The shear demonstrates to be the most concerning wind type regarding the landing lateral offset. Even if the trend is the same as the previous one (discontinuous for the h_{enc} - figure 7.9 - and linear for slope - figure 7.10 - and maximum value - 7.11), the overall touchdown lateral offsets are way greater than the ones shown in with the ramp or the gust. Even if the shear has the same shape as the ramp, it appears to be way more influential and critical. This is mainly due to two factors:

- **Overall magnitude**: while the first part of the shear is identical to a regular ramp, the second part of it has a double magnitude, referred to the prior wind condition. If for example, the set
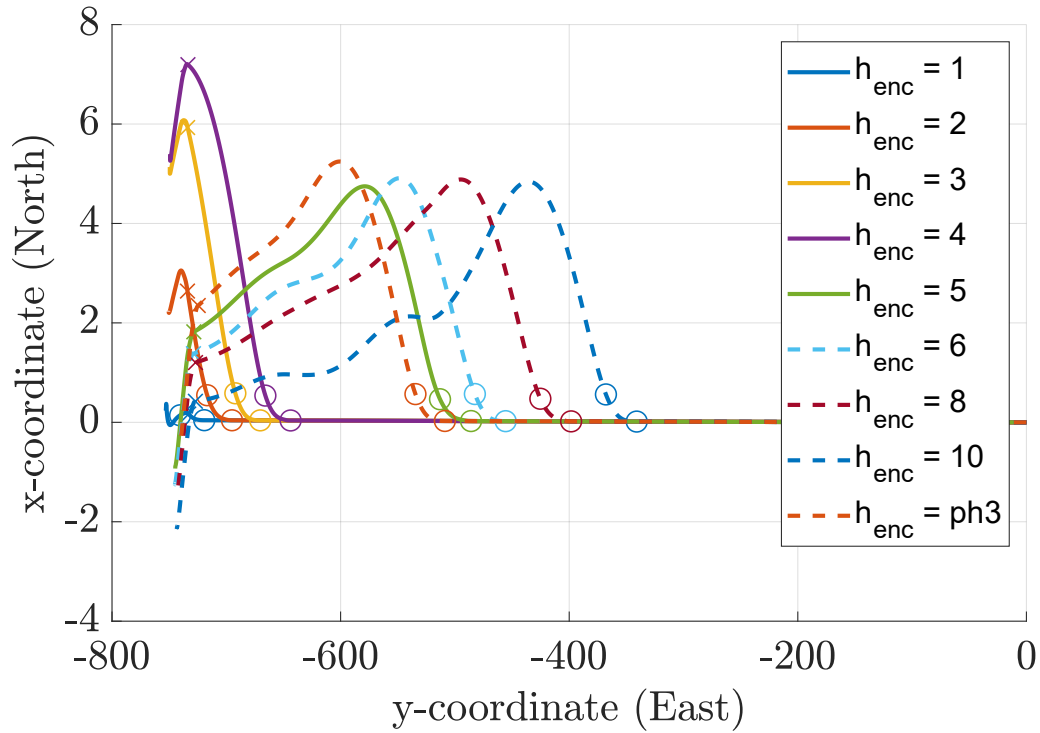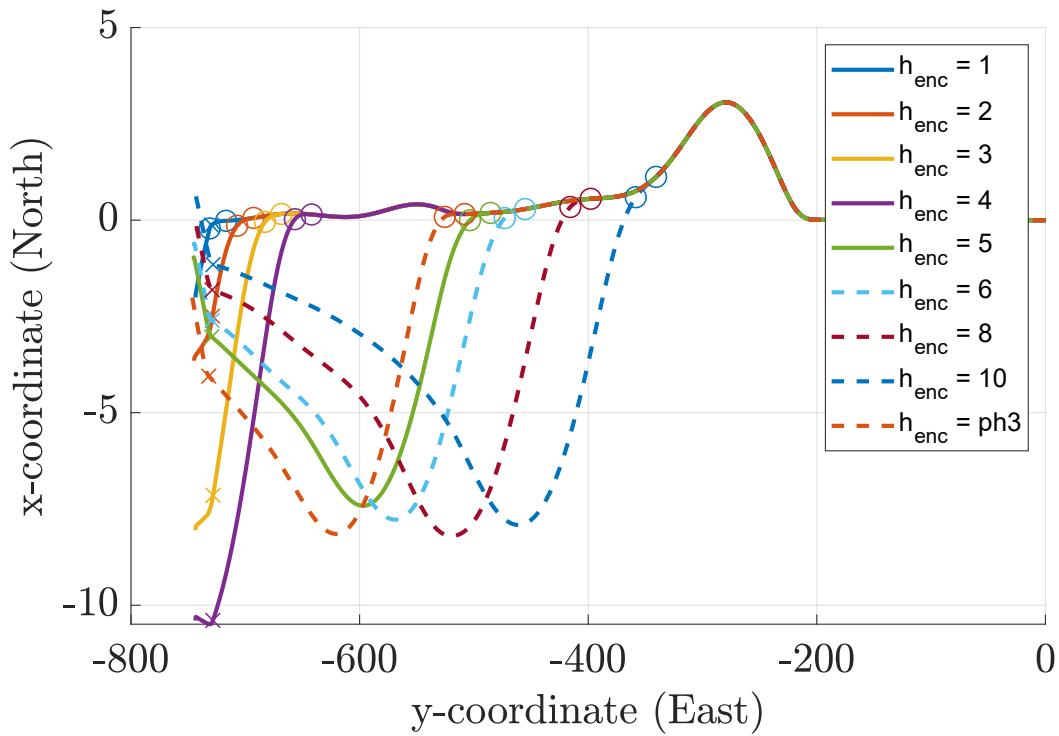
Figure 7.9: x-y trajectory with respect to the height of encounter of the shear
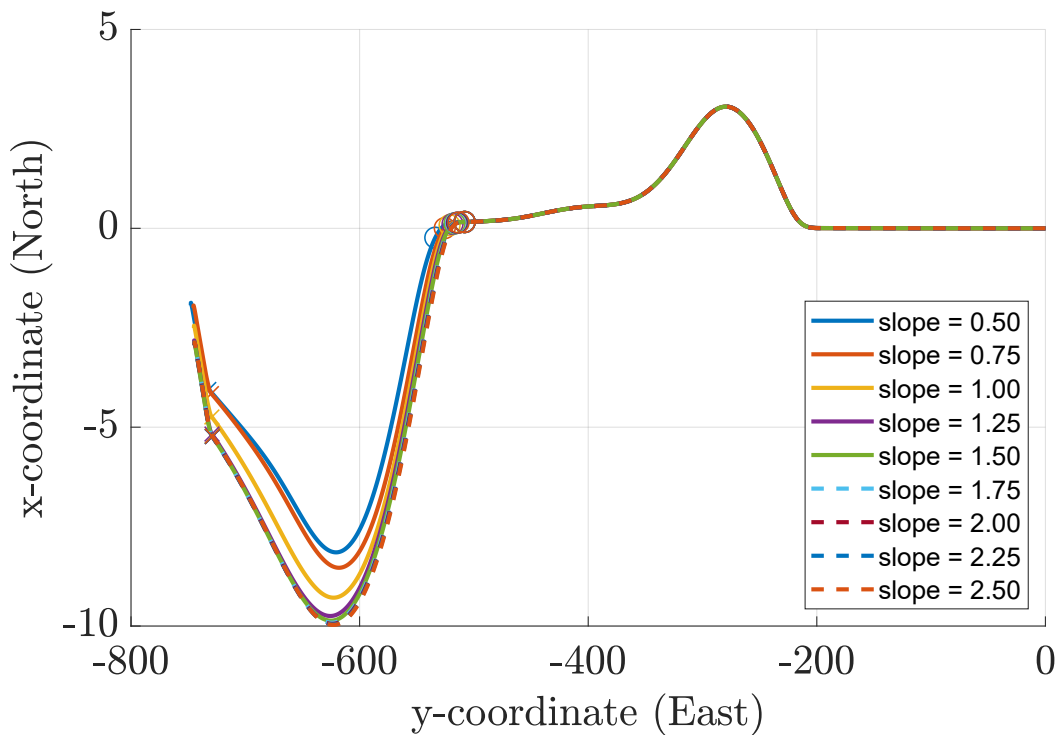
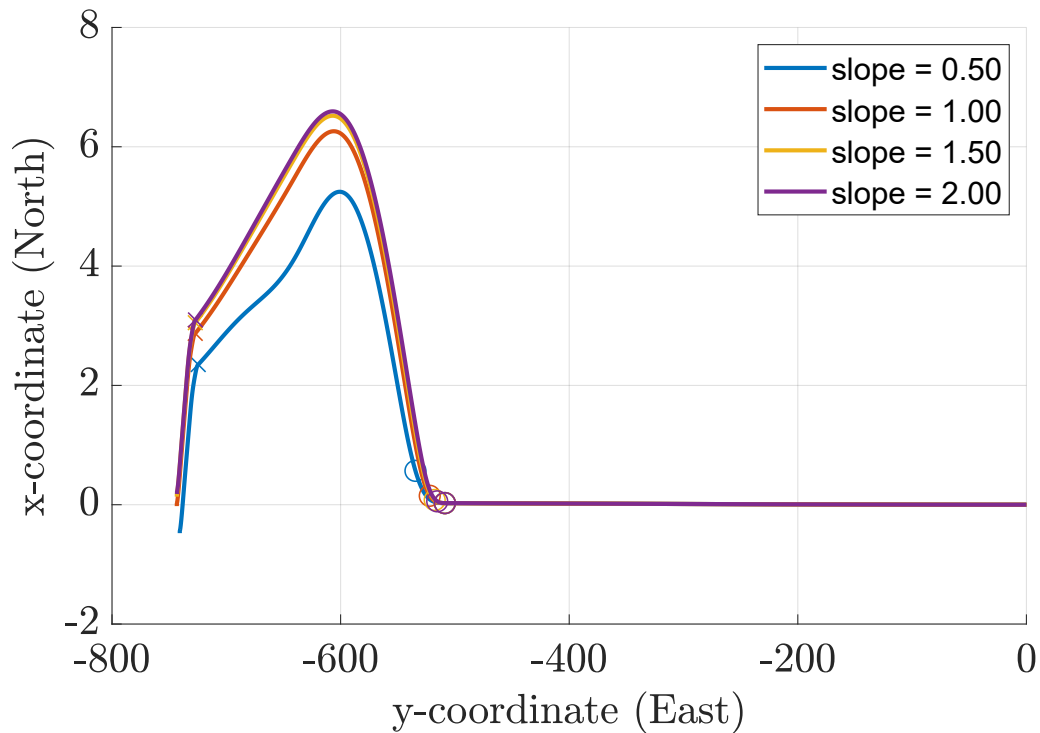
Figure 7.10: x-y trajectory with respect to the slope of the shear
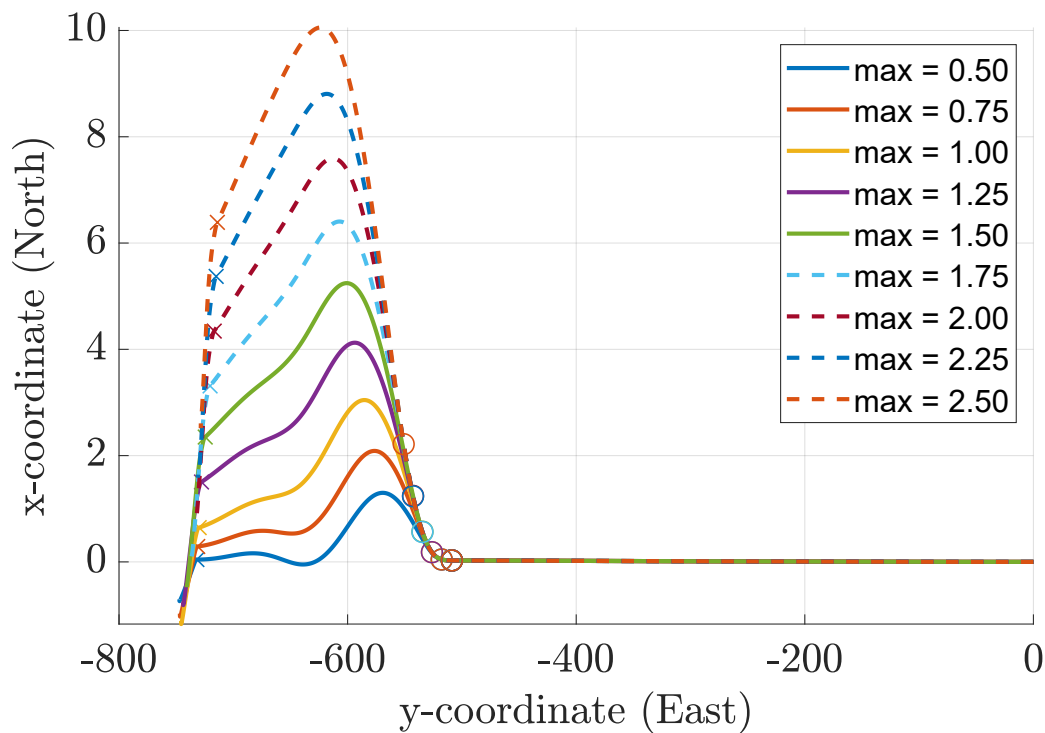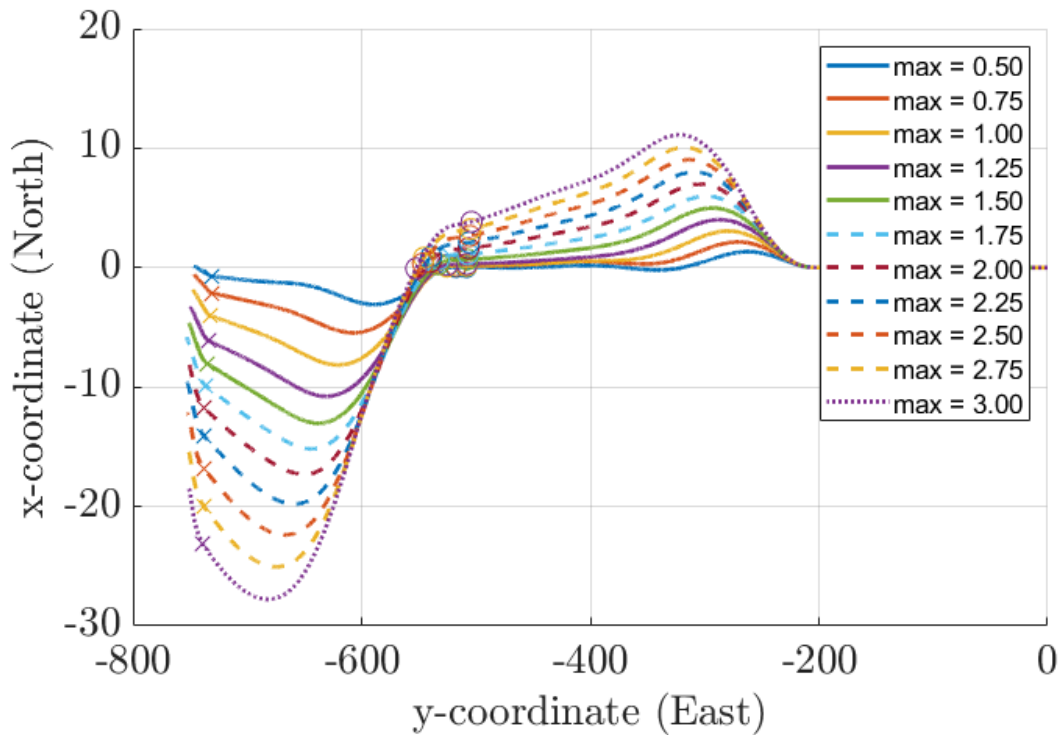
Figure 7.11: x-y trajectory with respect to the maximum value of the shear

magnitude is 2 m/s, the first part of the shear will rise from 0 to 2 m/s, while the second one will go from 2 to -2 m/s, constituting a global change of 4 m/s.

- **Attitude and orientation**: concerning this point, further analysis is needed to better explain this specific case.

Attitude and orientation considerations for the shear

The purpose of this small paragraph is to set out some specific considerations for the wind shear case, particularly about the attitude of the aircraft in this condition. To verify these considerations, a comparison is made between two different but equivalent wind disturbances, as expressed in table 7.3:

Table 7.3: Ramp-shear comparison

Wind disturbance	h_{enc} (m)	$slope$ (m/s^2)	$v_{W_{max}}$ (m/s)
Ramp	default (h_{phase_3})	default (0.5)	1.5
Shear	default (h_{phase_3})	default (0.5)	1.5

In the comparison plots, the blue lines refer to the ramp disturbance, while the orange ones refer to the wind shear.

As a first step, through figure 7.12 it can be seen that, once the disturbance has been addressed and the aircraft has moved into a stable configuration, the longitudinal component of the crosswind is

negative, constituting a headwind. It is important to note here that u_{W_b} decreases for both wind types as soon as the wind is encountered, meaning that a headwind is only present in the adapted configuration (the one that is fully stabilised with respect to the disturbance).
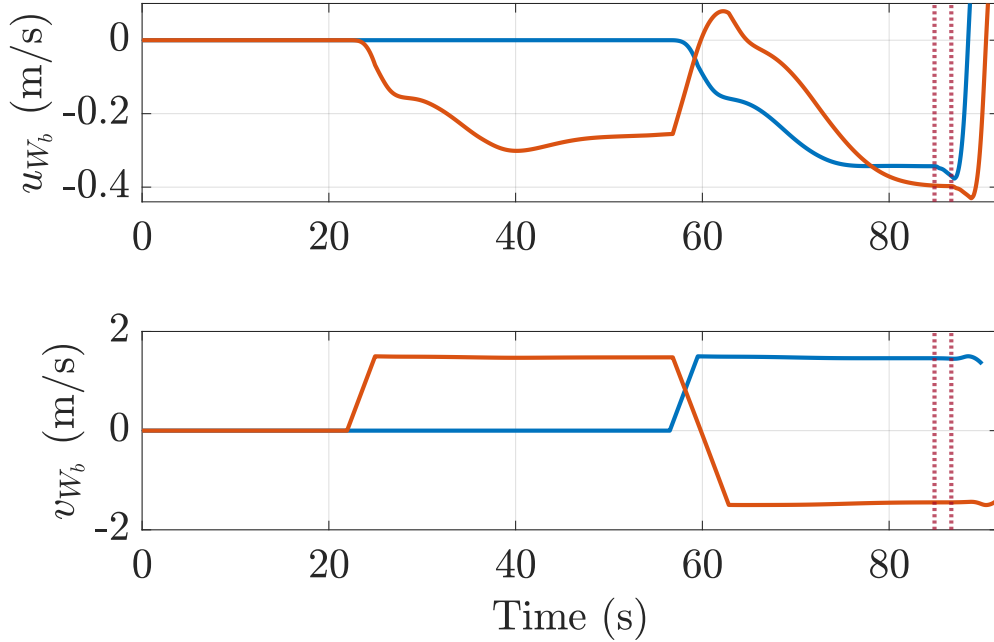
Figure 7.12: $x - y$ components of the wind vector for the ramp-shear comparison

Even if in both cases, as soon as the (first) disturbance manifests itself, the variable goes to a negative value (stabilised at about 50 s for the shear, as also demonstrated by the corresponding value of 60 s in figure 7.13, and at about 80 s for the ramp), only in the case of the wind shear a transient exists (from 55 s to 75 s). With transient, the process is meant that the aircraft takes to adapt to the wind changing directions from one side to the opposite.

Here, the x-component of the wind vector is inverted in sign, to then stabilise again at a negative value. In this transient lies an explanation for the greater effectiveness of the wind shear, which will be better explained using figure 7.14.

Figure 7.14 shows two conditions of the aircraft, ideally made to coincide for ease of explanation. The first, indicated by the subscript 'a', indicates the adapted condition, i.e. before the second part of the wind shear occurs, while the second, indicated by the subscript 't', concerns the transient situation, immediately after the encounter of the aforementioned disturbance. In both cases, the velocity expressed in the air-path reference frame $\overrightarrow{V'}_A$ is the same, while the wind velocity vector and the kinetic one are different.

In the adapted case, the kinetic velocity vector $\overrightarrow{V'}_{K_a}$ is pointing to the runway, as the vehicle is
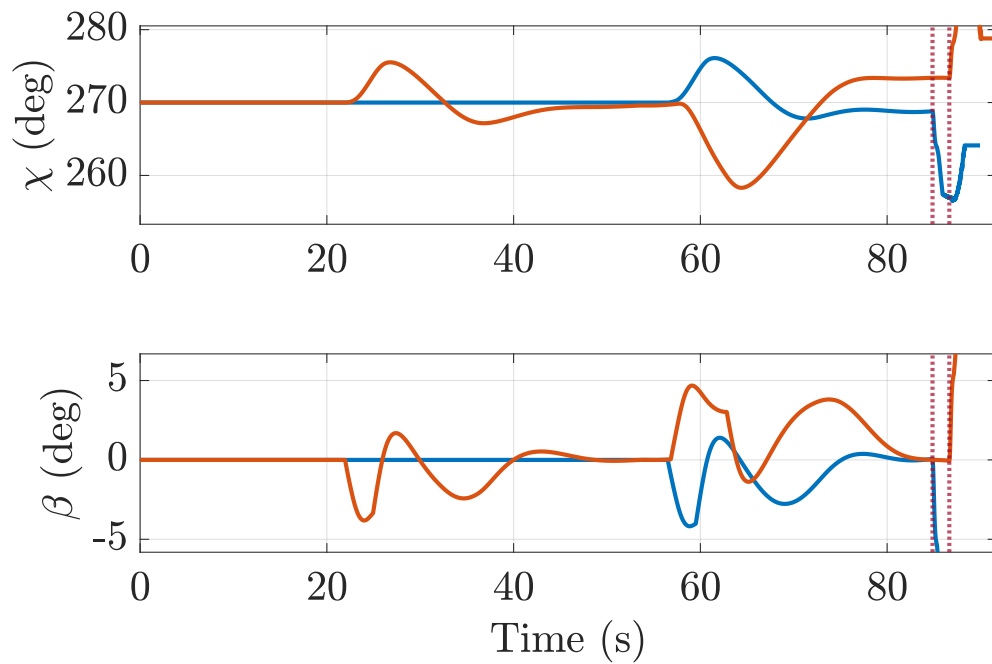
Figure 7.13: χ - β plot for the ramp-shear comparison
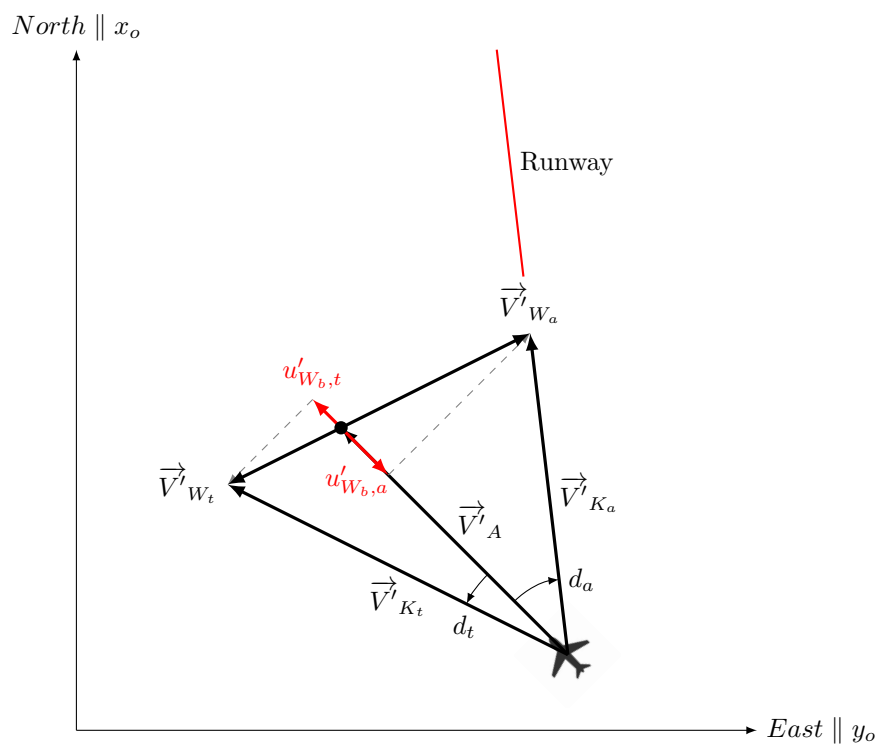
Figure 7.14: Transient u_{W_b} and drift angle visualisation

adapted to the constant wind expressed by $\overrightarrow{V'}_{W_a}$. As a confirmation of the time histories in figure 7.12, the red vector (constituting the x component of the wind velocity vector, with respect to the body reference frame) is negative.

In the other case, the overall wind vector $\overrightarrow{V'}_{W_t}$, is switched in verse with respect to the adapted one, with an inverse longitudinal component, indicated by $u'_{W_b,t} > 0$, which is actually (temporarily) positive. Even if the change of the wind velocity vector is permanent, the longitudinal component is only temporarily positive, and in this configuration, the consequent drift angle d_t changes sign with respect to the adapted one (d_a). In the time interval between the configuration indicated as transient here, and the following adapted condition (where the vehicle is pointing to the right, opposite to the one shown in the picture), the vehicle receives a temporary additional tailwind (the positive component of the wind vector) which is another cause of the amplification of the effect of the shear. The additional tailwind increases the inertial velocity while the aircraft is already flying in the wrong direction. As a consequence, the offset to the runway is setup faster.

7.2.4   Loads

As mentioned before, some load plots are going to be shown here, as complementary for the general evaluation of every landing process. All of them follow the same structure of the xy plots, by showing the trend of the specific vertical normalised load for each skid (expressed in g), according to the different wind parameters.

For example, figure 7.15 shows the right wing gear vertical force, normalised by the mass acting on it, parametrised as a function of the height of encounter of the ramp. In this case, only the h_{enc} of 1 m leads to an unsatisfactory result, in terms of maximum allowable acceleration. This case is explained in more detail below (7.2.5).

For the ramp specifically, since the wind is always coming from the left of the aircraft, the right wing load is the most important one.

In the case of the gust, figure 7.16, the loads on the right wing gear are quite similar for all the cases, and always below the limit.

As already seen in the xy plots, the shear is the most influencing disturbance, clearly showing in figure 7.17 that there is a limit for the magnitude of the shear, here for the left wing gear, which among all the others, is the most stressed of the two side gears, since the wind disturbance comes from the right of the aircraft. The fact that the wind shear is particularly varied in terms of the output produced on the different gears makes it the perfect candidate for further studies on the influence of its parameters on the model, as carried out in the following sections
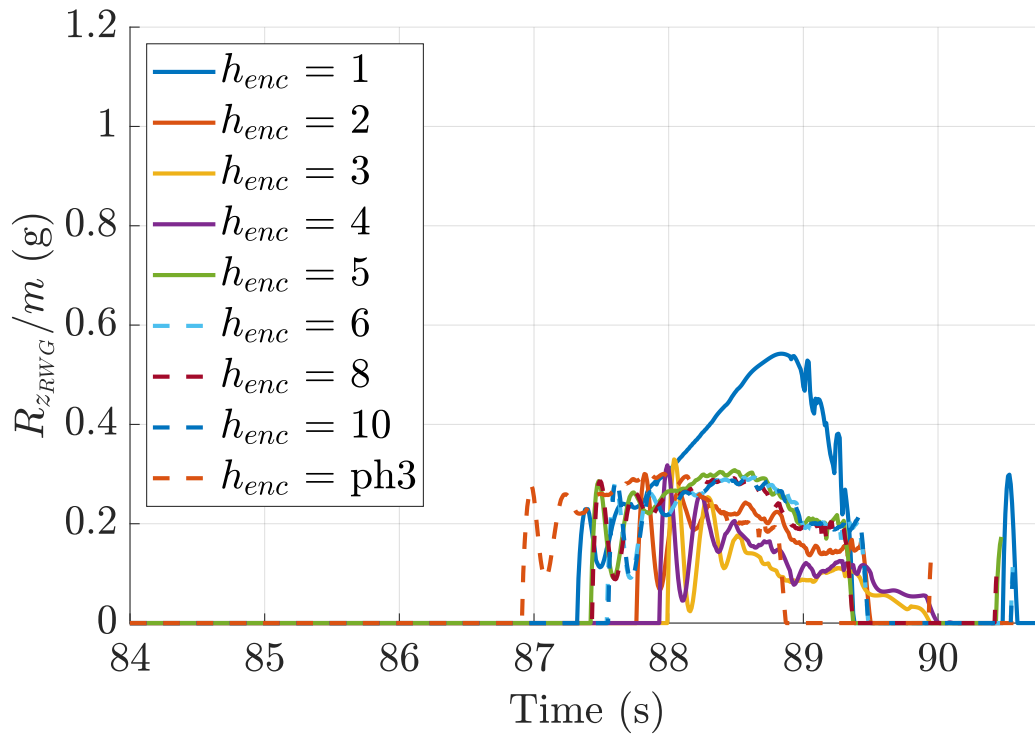
Figure 7.15: Vertical RWG load with respect to the height of encounter of the ramp
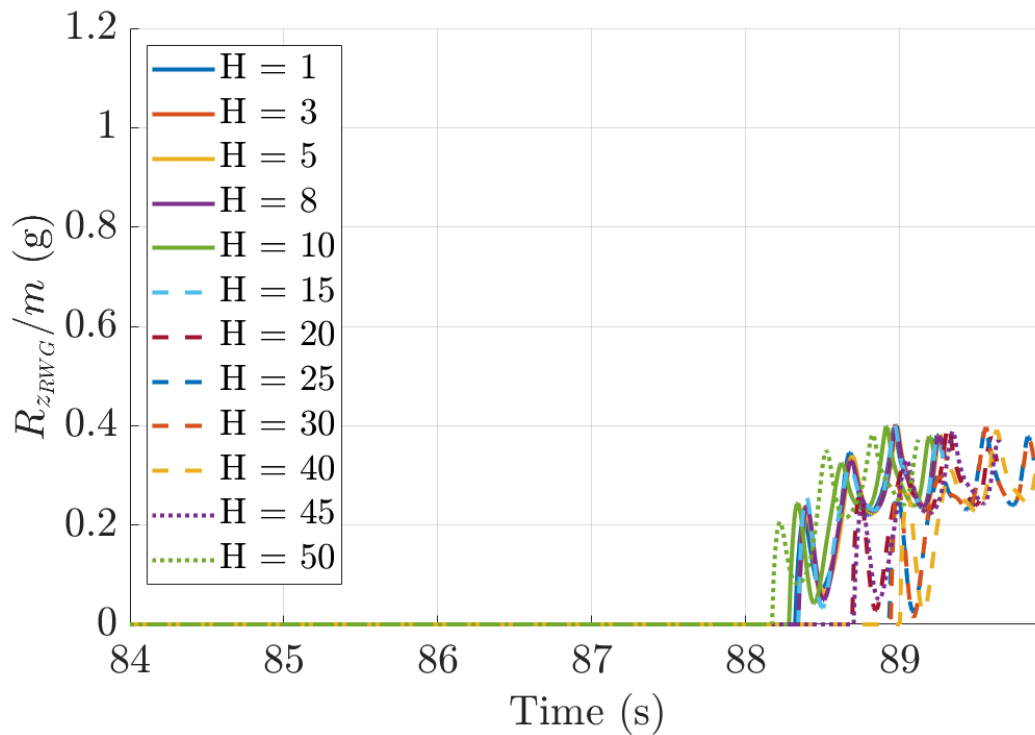
Figure 7.16: Vertical RWG load with respect to the wavelength of the gust
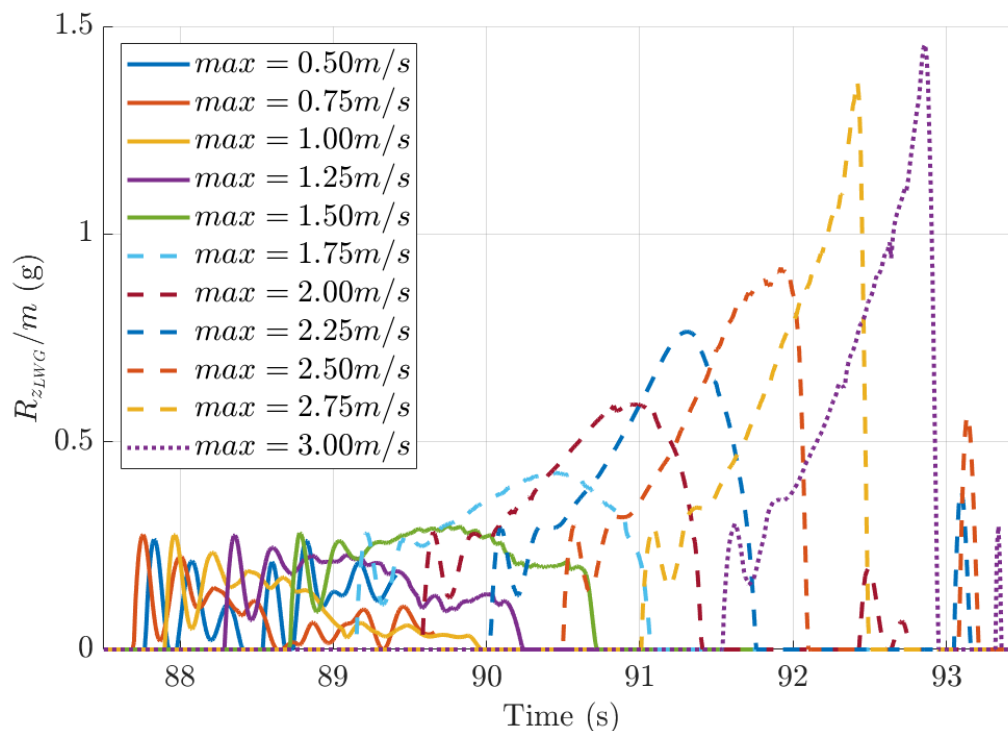
Figure 7.17: Vertical LWG load with respect to the maximum value of the shear

7.2.5 Influence of bank angle

In the following, a specific case is anlysed in more depth in order to show the influence the bank angle has on the occurring skid forces.

As visible from figure 7.15, the case of $h_{enc} = 1$ is not satisfied concerning the RWG load. The explanation for this is to be found in the time histories of the single case, in comparison with that for $h_{enc} = 2$. Consequently, in all subsequent graphs, the blue lines represent $h_{enc} = 1$, while the orange ones refer to the 2 m case, and they will also be referred to as, respectively, the first and the second disturbance.

Given that, the maximum value of the ramp and its slope are the same, the two disturbances are coming one after the other, as visible from the third plot of figure 7.19. The main difference, then, is represented by the touchdown attitude of the vehicle, and among all, the bank angle (fourth plot of the same figure). While for the case of $h_{enc} = 2$, the bank angle at the touchdown instant is equal to $0.05°$, for the other case it is equal to $0.77°$.

This difference is due to the different timing of the disturbances, indeed, while the second disturbance can be faced and repositioning to an adapted configuration (by yawing into the direction of the oncoming flow and reducing bank angle at the same time) is possible before touchdown, the first disturbance reaches the aircraft shortly before the actual landing, continuing even afterwards, and thus further stressing the right skid. This is aggravated by the latter's unfavourable position since the aforementioned bank angle

111
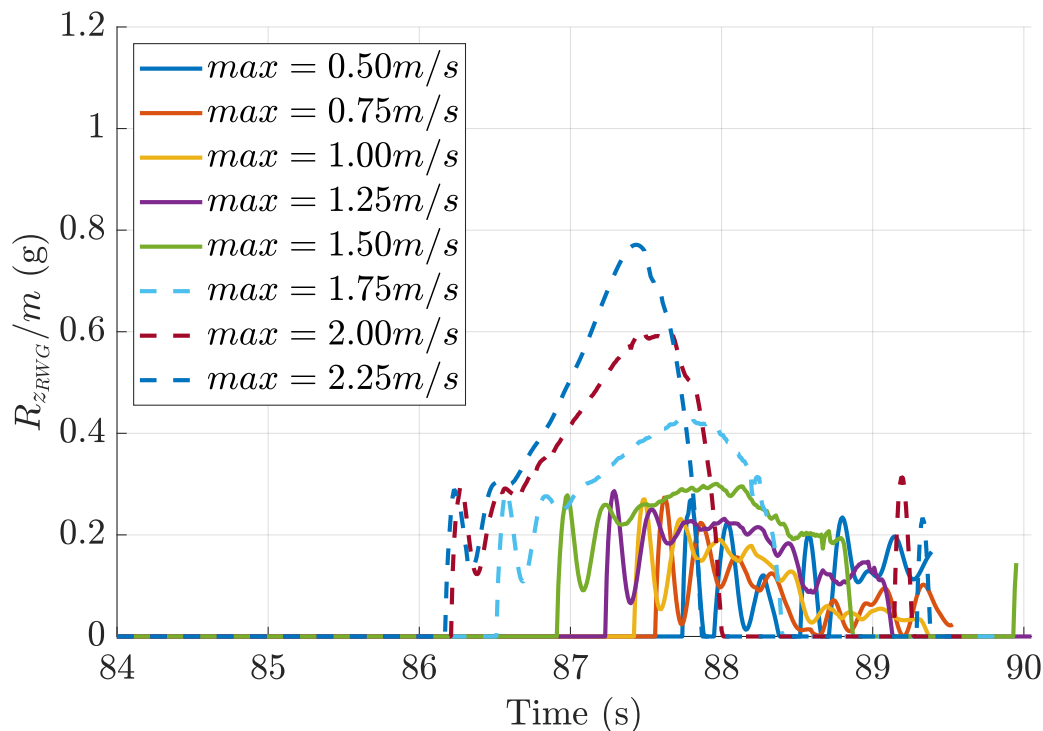
Figure 7.18: Vertical RWG load with respect to the maximum value of the ramp

makes it much closer to the ground than it is in the case of $h_{enc} = 2$ m. Therefore, the rolling motion induced by the main skid due to touchdown with a crab angle leads to higher impact velocities and forces for the case of $h_{enc} = 1$ m.

This situation would seem to contradict what was previously discussed in section 7.1 for the steady-state analysis, given that 1.75 m/s was found as the maximum possible disturbance. However, the mere fact that the disturbance is encountered in the initial instants of the simulation makes the aircraft fully adapted to the disturbance well before touchdown occurs. This is in agreement with the result of the previous comparison, i.e. that reaching full stabilisation (meaning a zero or even negative value - generally opposite to where the disturbance would bring it - of bank angle) before touchdown helps to reduce the lateral loads on the interested lateral skid, especially when the wind is still acting on the vehicle after the touchdown.

Regarding the *stabilised* condition, it would usually refer to an undisturbed flight, like before the wind disturbance, but here it is meant as *adapted* situation, regarding the incoming wind, whichever it is. So, being in a stabilised condition refers to the fact that the vehicle's flight path is aiming towards the centre of the runway , the flight is not accelerated and there are no rotational rates and sideslip.

To summarise these considerations, the table 7.4 shows the different cases, and their bank angle at the touchdown instant.
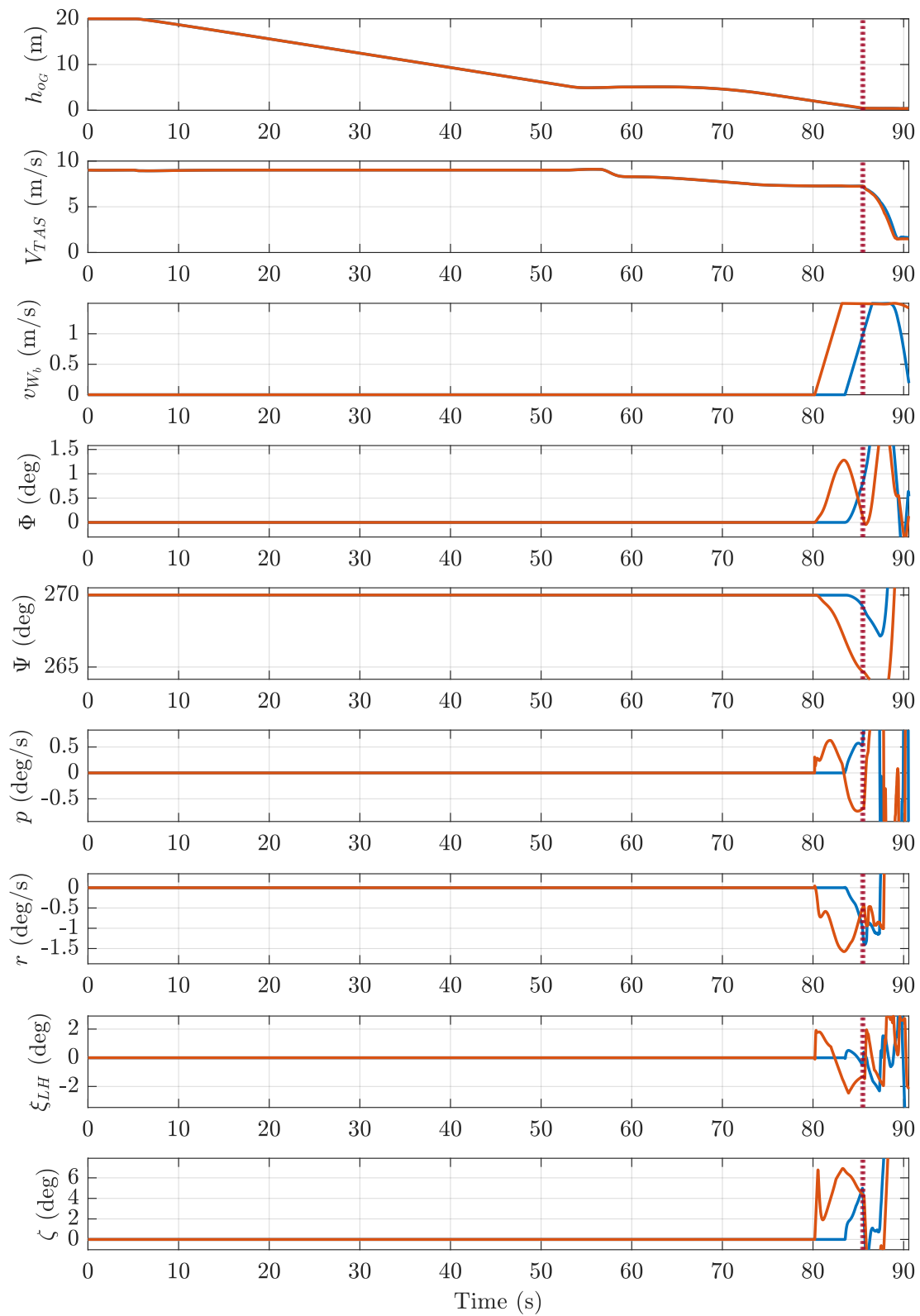
Figure 7.19: Time histories (ramp variables comparison)
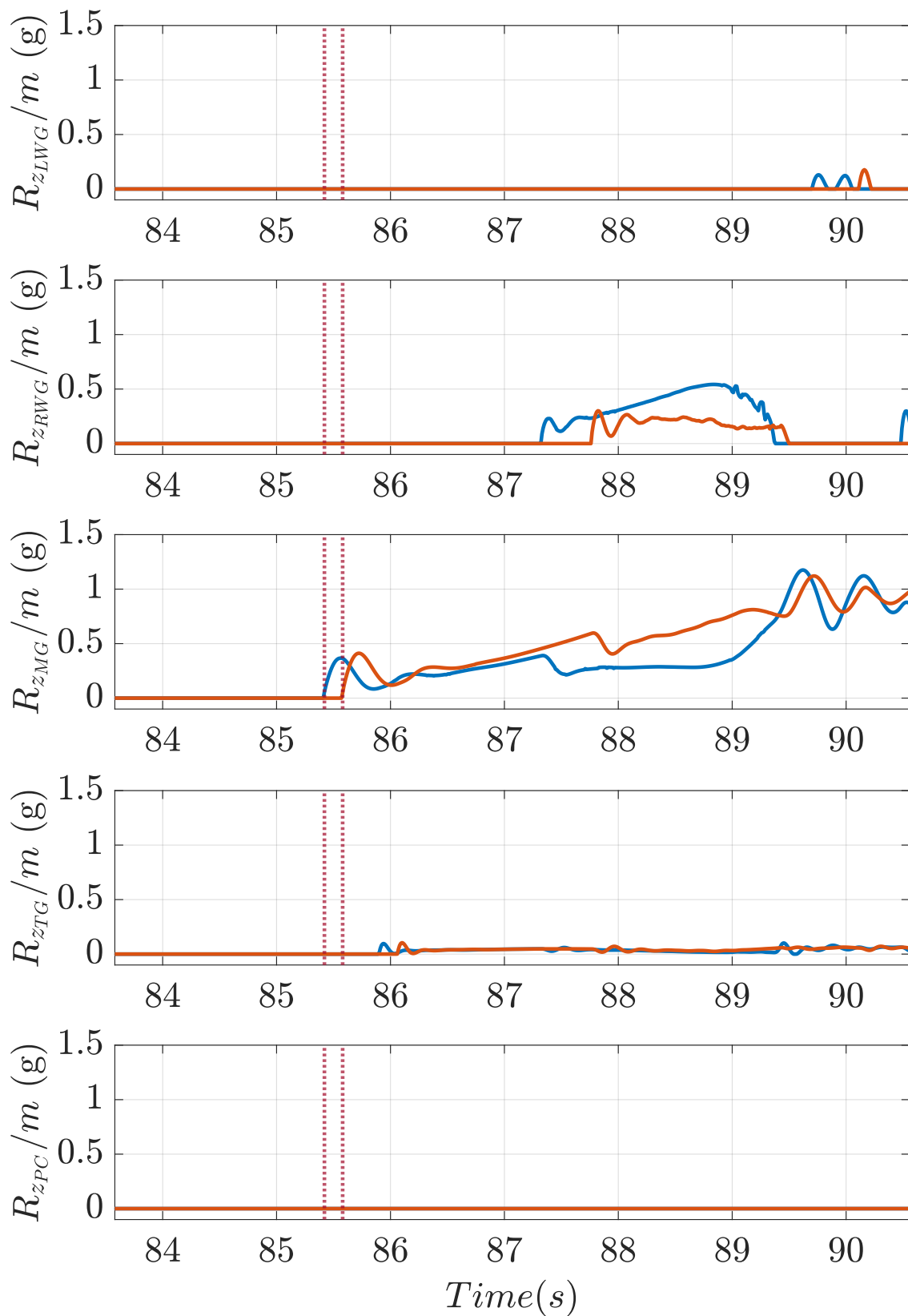
Figure 7.20: Time histories (ramp loads comparison)

Table 7.4: Relation between bank angle and RWG loads, for three examined cases

	Steady-state case	Default (h_{enc} = 1 m)	Default (h_{enc} = 2 m)
h_{enc} (m)	25	1	2
$v_{W_{max}}$ (m/s)	1.75	1.5	1.5
$\Phi(t_{TD})$ (deg)	−0.15	0.77	0.05
$R_{z_{RWG_{max}}}/m$ (g)	0.41	0.54	0.3
Successful	yes	no	yes

7.2.6 Evaluation matrices

To have a simple but effective visualisation tool, some evaluation matrices are being developed to give an immediate idea of the accordance between the results of the parameter study and the evaluation criteria.

These matrices are made for every wind type and can be read as if they were tables. So, each of the three inputs will have its table, showing a zero if the condition is not satisfied, or a one if the requirement is met. By simply looking at them, some immediate conclusions can be drawn.

Ramp

Starting with the ramp wind type, the tables 7.5, 7.6 and 7.7 respectively show the evaluation matrix for the height of encounter, for the slope and the maximum of the wind disturbance. it is possible to assume that if a ramp hits the plane, the landing will always be possible, both for the xy criteria and the loads, except for the case when h_{enc} is 1 m, and when $v_{W_{max}}$ is greater than 2 m/s. For all cases, the MG criterion is satisfied.

Table 7.5: Ramp evaluation matrix parametrised with h_{enc}

Criterion \ h_{enc}	1	2	3	4	h_{ph3}	5	6	8	10
xy	1	1	0	0	1	1	1	1	1
$R_{z_{LWG}}/m$	1	1	1	1	1	1	1	1	1
$R_{z_{RWG}}/m$	0	1	1	1	1	1	1	1	1
$R_{z_{MG}}/m$	1	1	1	1	1	1	1	1	1
$R_{z_{TG}}/m$	1	1	1	1	1	1	1	1	1
$R_{z_{PC}}/m$	1	1	1	1	1	1	1	1	1
MG	1	1	1	1	1	1	1	1	1
All	0	1	0	0	1	1	1	1	1

Gust

Concerning the gust, tables 7.8, 7.9 and 7.10 show that any maximum value of the disturbance produces an acceptable result, giving an idea that this parameter has little influence on the final result. Again, in

Table 7.6: Ramp evaluation matrix parameterised with *slope*

Criterion $v_{W_{max}}$	0.5	1.0	1.5	2
xy	1	1	1	1
$R_{z_{LWG}}/m$	1	1	1	1
$R_{z_{RWG}}/m$	1	1	1	1
$R_{z_{MG}}/m$	1	1	1	1
$R_{z_{TG}}/m$	1	1	1	1
$R_{z_{PC}}/m$	1	1	1	1
MG	1	1	1	1
All	1	1	1	1

Table 7.7: Ramp evaluation matrix parametrised with $v_{W_{max}}$

Criterion $v_{W_{max}}$	0.5	0.75	1.0	1.25	1.5	1.75	2.0	2.25
xy	1	1	1	1	1	1	1	0
$R_{z_{LWG}}/m$	1	1	1	1	1	1	1	1
$R_{z_{RWG}}/m$	1	1	1	1	1	1	0	0
$R_{z_{MG}}/m$	1	1	1	1	1	1	1	1
$R_{z_{TG}}/m$	1	1	1	1	1	1	1	1
$R_{z_{PC}}/m$	1	1	1	1	1	1	1	1
MG	1	1	1	1	1	1	1	1
All	1	1	1	1	1	1	0	0

this case, all the landings are successful with also the consideration of the MG criterion.

Table 7.8: Gust evaluation matrix parametrised with h_{enc}

Criterion h_{enc}	1	2	3	4	h_{ph3}	5	6	8	10
xy	1	1	1	1	1	1	1	1	1
$R_{z_{LWG}}/m$	1	1	1	1	1	1	1	1	1
$R_{z_{RWG}}/m$	1	1	1	1	1	1	1	1	1
$R_{z_{MG}}/m$	1	1	1	1	1	1	1	1	1
$R_{z_{TG}}/m$	1	1	1	1	1	1	1	1	1
$R_{z_{PC}}/m$	1	1	1	1	1	1	1	1	1
MG	1	1	1	1	1	1	1	1	1
All	1	1	1	1	1	1	1	1	1

Shear

Lastly, for the shear, tables 7.11, 7.12 and 7.13 deal with the more complex situation for this wind input.

Table 7.9: Gust evaluation matrix parametrised with H

Criterion \ H	1	3	5	8	10	15	20	25	30	40	45	50
xy	1	1	1	1	1	1	1	1	1	1	1	1
$R_{z_{LWG}}/m$	1	1	1	1	1	1	1	1	1	1	1	1
$R_{z_{RWG}}/m$	1	1	1	1	1	1	1	1	1	1	1	1
$R_{z_{MG}}/m$	1	1	1	1	1	1	1	1	1	1	1	1
$R_{z_{TG}}/m$	1	1	1	1	1	1	1	1	1	1	1	1
$R_{z_{PC}}/m$	1	1	1	1	1	1	1	1	1	1	1	1
MG	1	1	1	1	1	1	1	1	1	1	1	1
All	1	1	1	1	1	1	1	1	1	1	1	1

Table 7.10: Gust evaluation matrix parametrised with $v_{W_{max}}$

Criterion \ $v_{W_{max}}$	0.5	0.75	1	1.25	1.5	1.75	2	2.25	2.5	2.75	3
xy	1	1	1	1	1	1	1	1	1	1	1
$R_{z_{LWG}}/m$	1	1	1	1	1	1	1	1	1	1	1
$R_{z_{RWG}}/m$	1	1	1	1	1	1	1	1	1	1	1
$R_{z_{MG}}/m$	1	1	1	1	1	1	1	1	1	1	1
$R_{z_{TG}}/m$	1	1	1	1	1	1	1	1	1	1	1
$R_{z_{PC}}/m$	1	1	1	1	1	1	1	1	1	1	1
MG	1	1	1	1	1	1	1	1	1	1	1
All	1	1	1	1	1	1	1	1	1	1	1

Table 7.11: Shear evaluation matrix parametrised with h_{enc}

Criterion \ h_{enc}	1	2	3	4	h_{ph3}	5	6	8	10
xy	1	1	0	0	1	1	1	1	1
$R_{z_{LWG}}/m$	1	1	1	1	1	1	1	1	1
$R_{z_{RWG}}/m$	1	1	1	1	1	1	1	1	1
$R_{z_{MG}}/m$	1	1	1	1	1	1	1	1	1
$R_{z_{TG}}/m$	1	1	1	1	1	1	1	1	1
$R_{z_{PC}}/m$	1	1	1	1	1	1	1	1	1
MG	1	1	1	1	1	1	1	1	1
All	1	1	0	0	1	1	1	1	1

Table 7.12: Shear evaluation matrix parametrised with $slope_2$

Criterion \ h_{enc}	0.5	0.75	1.0	1.25	1.5	1.75	2.0	2.25	2.5
xy	1	1	1	0	0	0	0	0	0
$R_{z_{LWG}}/m$	1	1	1	1	1	1	1	1	1
$R_{z_{RWG}}/m$	1	1	1	1	1	1	1	1	1
$R_{z_{MG}}/m$	1	1	1	1	1	1	1	1	1
$R_{z_{TG}}/m$	1	1	1	1	1	1	1	1	1
$R_{z_{PC}}/m$	1	1	1	1	1	1	1	1	1
MG	1	1	1	1	1	1	1	1	1
All	1	1	1	0	0	0	0	0	0

In the case of the shear, the height of the encounter and the slope (both of the second ramp of the shear) do not influence either the loads or the MG liftoff, but they have a significant impact on the lateral offset, making this criterion difficult to meet. On the other hand, regarding the maximum value of the shear, both the loads and the lateral offset criteria are not always met. In addition, for values greater than 2.5 m/s, the MG liftoff criterion is not satisfied either.

Table 7.13: Shear evaluation matrix parametrised with $v_{W_{max2}}$

Criterion \ $v_{W_{max}}$	0.5	0.75	1	1.25	1.5	1.75	2	2.25	2.5	2.75	3
xy	1	1	1	0	0	0	0	0	0	0	0
$R_{z_{LWG}}/m$	1	1	1	1	1	1	0	0	0	0	0
$R_{z_{RWG}}/m$	1	1	1	1	1	1	1	1	1	0	0
$R_{z_{MG}}/m$	1	1	1	1	1	1	1	1	0	0	0
$R_{z_{TG}}/m$	1	1	1	1	1	1	1	1	1	1	1
$R_{z_{PC}}/m$	1	1	1	1	1	1	1	1	1	0	0
MG	1	1	1	1	1	1	1	1	0	0	0
All	1	1	1	0	0	0	0	0	0	0	0

7.3 Limiting cases

Starting from the results of the previous section, only certain combinations of parameters are acceptable when compared to the current criteria. In particular, while for the gust any result is acceptable, only a few of the shear are so. Also, some parameters are way more influential than others on the final considered output (both the lateral offset and the different loads), and this suggests that further investigations should be carried out to find the actual most critical combinations.

In fact, during the previous analyses, the parameters were varied according to their ranges, and one

by one. Now, the aim is to discover further unsatisfactory combinations, in order to define which are the actual operational limits of every wind type, so that the results will give a deeper insight into the capabilities of the model when excited with borderline external conditions.

7.3.1   Sensitivity analysis

While for the gust (as an example) the initial results are always compliant with the requirements, the shear gives much more problems, other than having a huge impact on the landing capabilities. Coming to the point of discovering which wind type, and more specifically, which combination of parameters is the most crucial, it is necessary to use specific tools being able to predict the impact of the initial conditions on the chosen outputs.

For this reason, different approaches are now presented:

- **Brute force**: used for the gust and the ramp, where not many parameters are too influential on the outputs.

- **Sensitivity analysis**: used for the shear, to predict which value of every parameter has the biggest influence, better discussed below.

The first step of the sensitivity analysis is to identify the outputs and the parameters. In our case, by fixing the wind type, three parameters are the ones among which to choose. On the other hand, the output can be the lateral coordinate or one of the five skid loads. To simplify, a basic configuration is explained in table 7.14.

Table 7.14: Sensitivity analysis scheme

Variable	Role	Symbol
x_o	*Output*	Y
h_{enc2}	*Parameter #1*	A
$v_{W_{max2}}$	*Parameter #2*	B
$slope_2$	*Parameter #3*	C

After this formal rename process, the relations between the variables are:

$$\begin{cases} S_A = \frac{\partial Y}{\partial A} \rightarrow S_{A_n} = \frac{\partial Y/\partial A}{A} \\[2ex] S_B = \frac{\partial Y}{\partial B} \rightarrow S_{B_n} = \frac{\partial Y/\partial B}{B} \\[2ex] S_C = \frac{\partial Y}{\partial C} \rightarrow S_{C_n} = \frac{\partial Y/\partial C}{C} \end{cases} \qquad (7.2)$$

Where, a generic S_X is the sensitivity of X, while S_{X_n} is the normalised sensitivity, useful for comparing the sensitivity of different parameters. When the data are function-based or continuous, this can be applied without any further modification, instead, when the data are in a more common discrete dataset,

like this case, a simple interpolation is needed to compute the different "partial derivatives", which become discrete increments with respect to each parameter, as in the generalised, finite differences version of equation 7.3, where ΔX represents a small variation in the X parameter.

$$S_X = \frac{Y(X + \Delta X) - Y(X - \Delta X)}{2 \cdot \Delta X} \tag{7.3}$$

By computing this it is possible to evaluate to what extent the variation of a single parameter will affect the final output, meaning that a great global or normalised sensitivity is evaluated with a great change in the lateral offset if performed with that specific parameter.

Below some examples are reported, particularly for the sensitivity of the shear with respect to its three parameters, with a focus on the left wing gear, being the most significant for this specific wind disturbance.
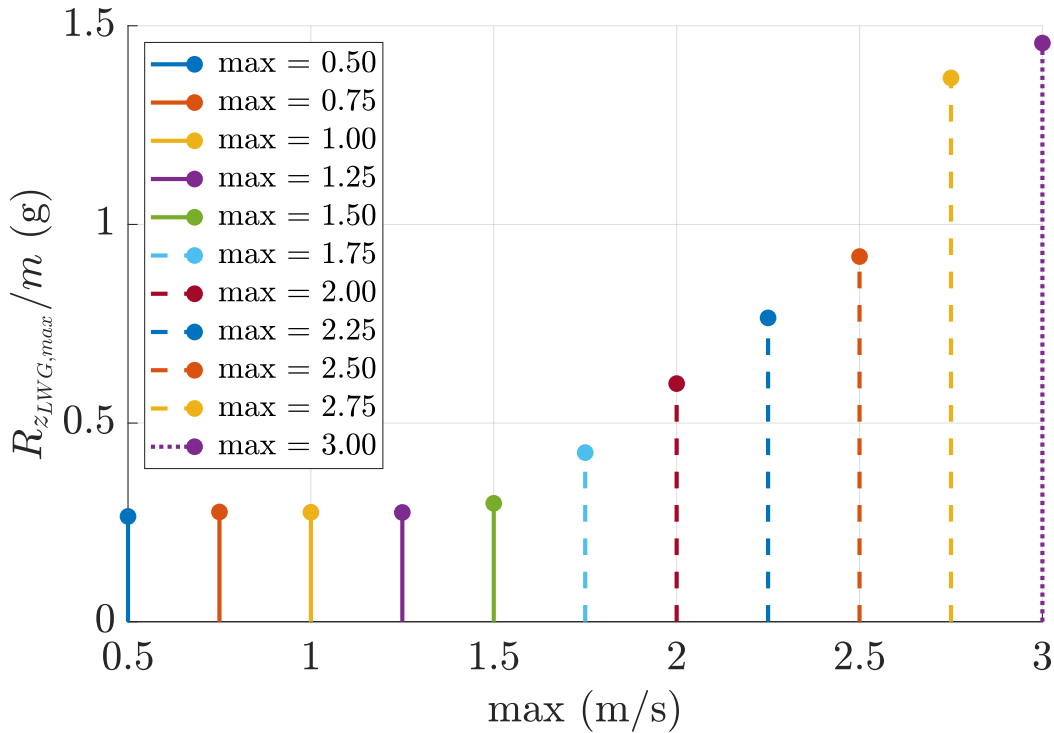
Figure 7.21: LWG load with respect to the maximum value of the shear

Figure 7.21 shows a clear connection between the resulting normalised load and the correspondent maximum of the shear. In fact, while until 1.5 m/s the load is more or less stationary, it starts to increase almost linearly for higher wind magnitudes, reaching the allowable limit for 1.75 m/s.

Then, by performing the above-mentioned sensitivity analysis, figure 7.22 shows the resulting sensitivity values, as well as the normalised ones, to have an easier value to manage. In both cases, a high sensitivity value indicates how that particular input value (wind maximum) has a large effect on the final measured result (load on the skids). In this case, values from 1.75 m/s onwards are particularly
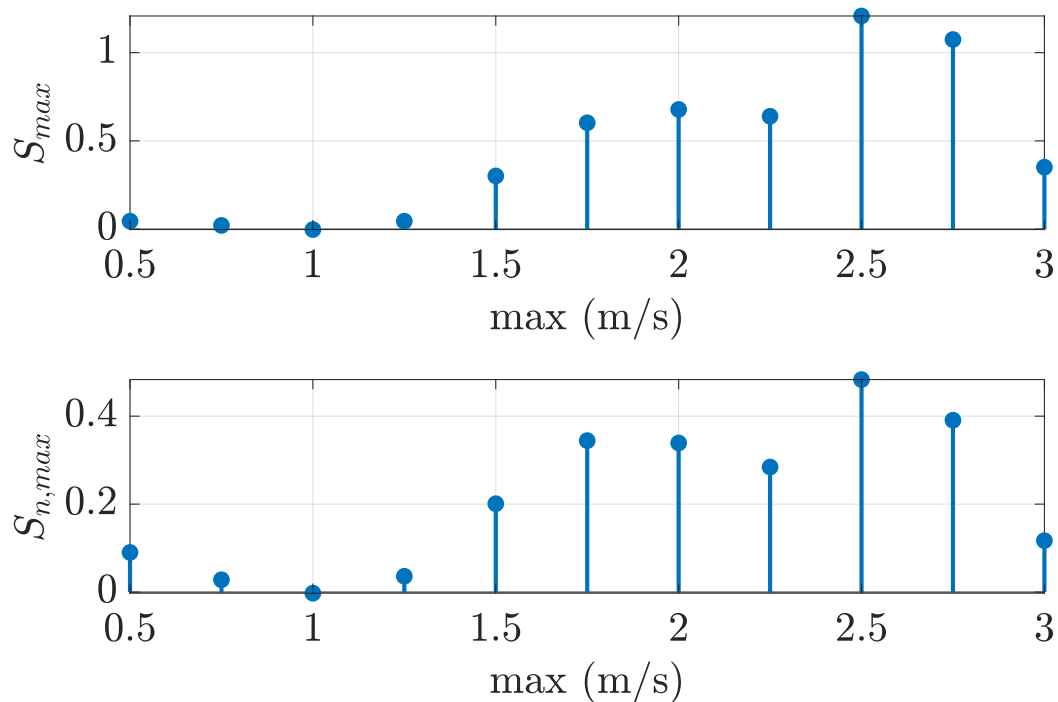
Figure 7.22: Sensitivity and normalised sensitivity for the LWG with respect to the maximum value of the shear

influential, and it is therefore convenient to analyse only these, to the exclusion of earlier values.

By doing so, it is easier to identify what the critical values of each parameter are, without necessarily having to go through all the possible combinations.

It is important to say that, even if this analysis allows to skim through the possible combinations, several parameters are involved and thus, it is also necessary to realistically assess the feasibility of certain combinations.

For example, for low heights of encounter, a value of $v_{W_{max}}$ lower than the one with the highest sensitivity will suffice to generate a critical point, as the sensitive values are deducted from the preliminary simulations, which utilise default values for the other parameters.

7.3.2   Critical combinations

After the different tests, several specific configurations are identified as borderline, meaning that any variation of any parameter would lead to an unacceptable result. The majority of them are beyond the initial results previously analysed, but a few are met at smaller values than the already tested, particularly for the shear, where already the default values were giving critical results.

In the table 7.15 is possible to see all the points, divided by wind type. All of them are the values towards the majority of effort is going to go in the next chapter, starting with the real simulation process.

Table 7.15: Critical identified points

Wind type	Point #	h_{enc} (m)	$slope$ (m/s^2)	$v_{W_{max}}$ (m/s)
	2	2	2	1.75
Ramp	3	3	1	1
	4	4	1	1
Wind type	Point #	h_{enc} (m)	H (m)	$v_{W_{max}}$ (m/s)
	1	1	50	1.5
	2	2	50	2.5
Gust	3	3	50	2
	4	4	50	3.25
Wind type	Point #	h_{enc2} (m)	$slope_2$ (m/s^2)	$v_{W_{max2}}$ (m/s)
	1	1	1.5	1.25
	2	2	1.25	1.5
Shear	3	3	0.5	0.5
	4	4	0.5	0.5
	5	4	1.25	1

7.4 Batch simulation

The purpose of this section is to present the simulations used to evaluate the aforementioned limits. Once all the parameters have been set it is due and important to search what the operational limits are in situations as close as possible to real conditions, meaning flight tests, and then actual operational life.

For these reasons, a batch simulation process is set up, focusing on each of the critical combinations identified in the last chapter. 1000 runs will be performed for each of these critical points, with the addition of continuous turbulence in the atmospheric model, to collect data from each simulation.

The process consists of a simple cycle over single simulations, controlled by the base MATLAB script used to evaluate every combination.

The MATLAB code has the role of setting up the parameters by calling all the external functions, storing the external values in in-built structures - one for every subsystem (like environment, atmosphere and flight dynamics) - run the initialisation process through the trim functions to find the equilibrium starting point, and then run the associated Simulink model with the above mentioned initial condition. This latter is then exporting the majority of the interesting variables to the workspace, marking the end of the simulation.

Regarding the time duration, the MATLAB script also contains the necessary instructions like the t_{final} and the time interval dt. However, it is due to say that the setting of the simulation time is mostly important when the landing controller is disabled, giving a precise duration of the steady simulation. In fact, in the other case (the landing controller is on) the time duration of the simulation is basically dictated by the landing process, so once the standstill logic makes the HAP stationary, the simulation automatically stops.

To have a sufficient and significant number of cases, 1000 runs are performed for each of the different critical points in table 7.15. Each point takes about 24 hours to be completed, so the workstation is left to work every night to optimise the time.

7.4.1 Batch success rates

In order to analyse the large amount of data produced with the batch simulation, it is necessary to prepare a code capable of automating the results evaluation procedure, flexible to variations and additions of any other critical points analysed and optimised to reduce the usage of computational power. To do so the designed script opens the indicated folder, sorts every workspace alphabetically, then loads some particular variables (namely, the loads of every skid) and, directly inside this loop, processes and extracts the needed information to draw up the results, without saving all the variables.

While the criteria are the same described in section 6.6, a new basic statistical evaluation is performed, based on the rate of success of lateral offset requirements and structural limits restrictions, summarised in equations 7.4 and expressed as a probability, then in percentage units. Regarding the MG liftoff, it was always satisfied.

$$
\begin{cases}
p_{xy} = \frac{1}{N_{run}} \sum_{i=1}^{N_{run}} s_{xy,i} \\[2mm]
p_{R_z} = \frac{1}{N_{run}} \sum_{i=1}^{N_{run}} s_{R_z,i}
\end{cases}
\tag{7.4}
$$

Where, p_{xy} and p_{a_z} are the success rates for the xy criteria and the loads, N_{run} is the number of iterations (1000 in this case), and s_{xy} and s_{R_z} are the single success for the xy criteria and the loads. By considering this, and referring to the same notation of table 7.15, the results are shown in table 7.16. The column referred to as p_{MG} shows the always satisfied MG criterion success rate, while the last column refers to the combined total success rate, computed as:

$$
\begin{cases}
s_{ALL} = s_{xy} \wedge s_{R_z} \\[2mm]
p_{ALL} = \frac{1}{N_{run}} \sum_{i=1}^{N_{run}} s_{ALL}
\end{cases}
\tag{7.5}
$$

7.4.2 Batch quantitative analysis

From now on, different types of results will be displayed and detailed, to have an overview of all the data collected in the various phases of the project, and then finalise with a complete example as a test under examination.

Whereas a qualitative analysis of the batch simulations was carried out in subsection 7.4.1, a quantitative version is now proposed, to validate the success rates more directly and to visualise the previously obtained results with appropriate plots.

Table 7.16: Success rates

Wind type	Point #	p_{xy} %	p_{MG} %	p_{R_z} %	p_{ALL} %
Ramp	2	61	100	99.9	60.9
	3	99.6	100	100	99.6
	4	92.8	100	100	92.8
Gust	1	100	100	86.6	86.6
	2	85	100	90.9	75.9
	3	87.5	100	96.6	84.1
	4	57.9	100	90.9	50.6
Shear	1	100	100	99.7	99.7
	2	51.6	100	84.6	37
	3	100	100	100	100
	4	98.2	100	100	98.2
	5	100	100	100	100

Below, the results of batch simulations using boxplots are then reported. The documentation of this tool is given in [26], and is quickly summarised for the sake of completeness, before moving on to the actual results.

A boxplot is a type of graph that provides a visualisation of the distribution of a set of data across several important statistical parameters. It is constructed in this way:

- **Center line (median)**: Within the box, there's a line representing the median of the data, which is the value that divides the dataset into two equal parts: 50% of the data lies above this line and the remaining 50% lies below.

- **Box**: The box itself extends from the Q1 (first quartile) to the Q3 (third quartile). The length of the box, known as the interquartile range (IQR), indicates the spread of the data in the central 50% of the distribution. In other words, the distance between Q3 and Q1 reflects the spread of the majority of the data.

- **Whiskers**: The lines extending from the box are called "whiskers". These represent the variability outside the central 50% of the data. Typically, the whiskers extend to data points that are within a maximum distance of 1.5 times the IQR above Q3 and below Q1. Any data point beyond this distance is considered an "outlier" and may be represented as an individual point on the plot.

- **Individual points (outliers)**: Points outside the whiskers represent "outlier" values, meaning they are significantly distant from the bulk of the data. These points can indicate extreme values or measurement errors.

Then, the boxplot tool provides a visual overview of the data distribution, allowing to identify the position of the median, the spread of the data within the central 50% (via the box), and the presence of extreme
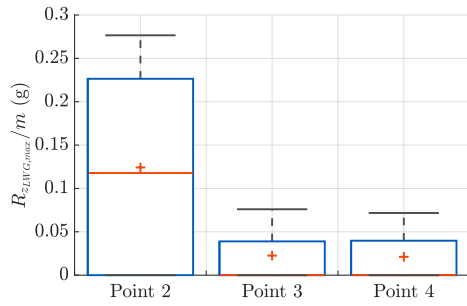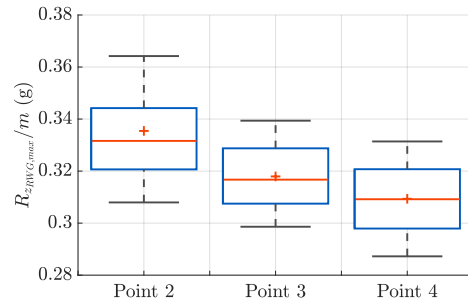
Figure 7.23: Ramp LWG boxplot
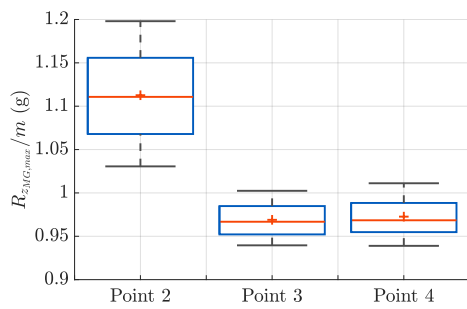

Figure 7.24: Ramp RWG boxplot
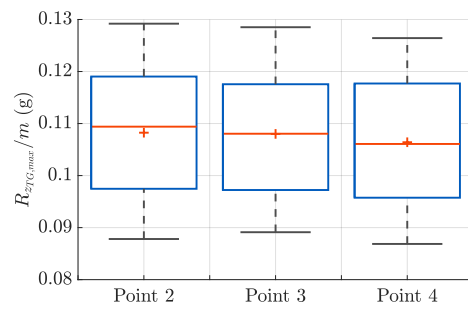

Figure 7.25: Ramp MG boxplot

Figure 7.26: Ramp TG boxplot
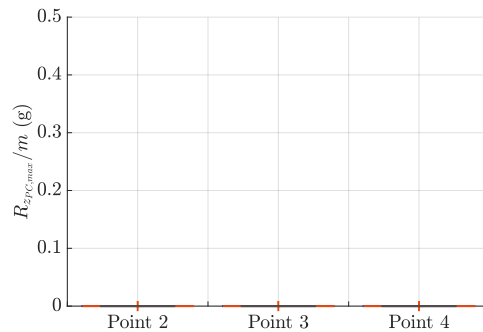
Figure 7.27: Ramp PC boxplot

Figure 7.28: Ramp boxplots

values (via the outliers). It's particularly useful for comparing the distribution of multiple groups of data or for identifying patterns or anomalies within the data itself. Regarding these boxplots, some comments and considerations can be made, also with the help of table 7.16.

Starting with the ramp, globally in figure 7.28, it is evident that point 2, overall, always shows higher values than the others, for all skids, and in particular for the left one, reaching maximum values more than 3 times larger than the other points for the same skid. However, this point is very similar to the one at $h_{enc} = 2$ discussed in section 7.2.5. Also, the percentage of success is almost total (only 1 case

over a thousand is not successful).

Then, the high value shown in the first boxplot is basically caused by the rebound of the LWG (which is either null or has a single spike), after that the RWG touches down. Here, as in the previous analysis, the aircraft resumes its original attitude shortly before landing, and for this reason, there are no unsatisfactory landings, although the overall values of the loads are slightly higher with respect to the other points (when the disturbance comes before and thus, a better stabilisation can be realised), as the landing is very close to resuming its original *stabilised* configuration.

Generally, the fact that the LWG boxes (for all points) extend from 0 to the maximum value, suggests that, in many cases, there is no contact of the left skid to the ground, which is perfectly normal as the wind disturbance always comes from the left of the aircraft.

To conclude about the ramp wind disturbance, the other skids have normal behaviour, so there is no ground contact of the PC, and the three remaining skids (RWG, MG and TG) follow a slightly inverted trend, so the overall loads are decreasing by moving from point 2 to point 4. This is in line with what was said earlier about the early adaptation to the incoming disturbance.

Moving on to the gust wind disturbance, the situation is quite varied, in that, whereas for the parametric study (section 7.2.2), all cases were always satisfactory, in this case, recalling the table 7.16, the load success rates are quite high but show that around one hundred simulations out of 1000 were not satisfactory. A more in-depth analysis is therefore necessary.

Regarding point 1, which is the worst case for (only) the loads, it is interesting to note from the second plot of figure 7.34 that the RWG has a wider extension with respect to the other points, as well as being the only skid exceeding its structural limit. This problem is similar to the one discussed previously for the ramp, in fact, since the disturbance is coming right before the touchdown (less than 2 s before it), and the overall gust is quite wide (remembering that the wavelength is equal to 50 m, so the time duration of it is 6 s as minimum, since the V_{TAS} at the touchdown is already lower than the trimmed one), this latter is strongly hitting the vehicle also after the touchdown, and for a prolonged period. Also, as expected from any kind of *late* wind encounter, the bank angle at the touchdown is already increased by the disturbance, and this is why the RWG is so stressed.

Generally speaking, this brings to the fact that (with a left-coming *late* disturbance) the RWG is always more stressed than the LWG, and actually, it is.

For point 2 the situation is slightly different since the disturbance is already finished when the touchdown occurs. So the vehicle is landing with a negative bank angle (residual from the wind adaptation process), firstly touching down with the LWG and then the RWG. In this case, the higher RWG load is because the aircraft pivots on the left skid, and therefore (in certain cases) bounces between the right and the left one.

While the same discussed condition is also valid for point 3, point 4 is totally different, and this is why it deserves to be further investigated. The main difference with the other points is that the LWG and the RWG have an opposite trend, as well as (in both cases) extremely high and low values. In fact, as in the

Figure 7.29: Gust LWG boxplot

Figure 7.30: Gust RWG boxplot

Figure 7.31: Gust MG boxplot
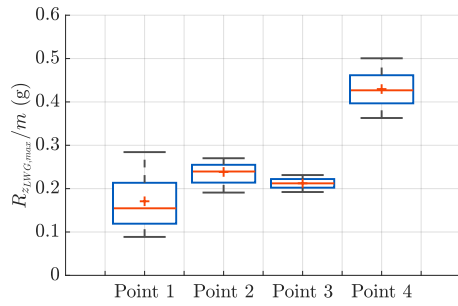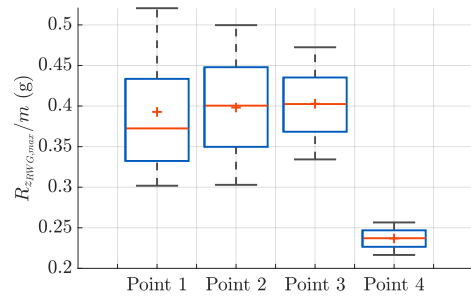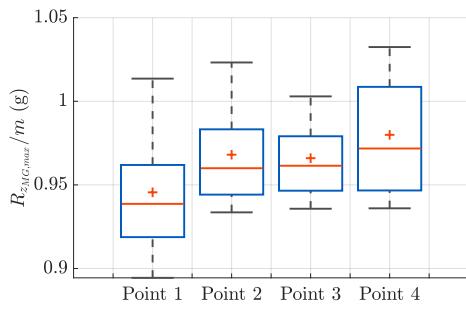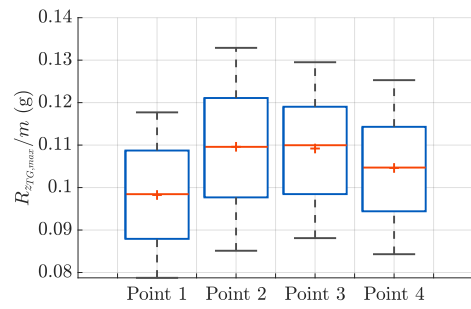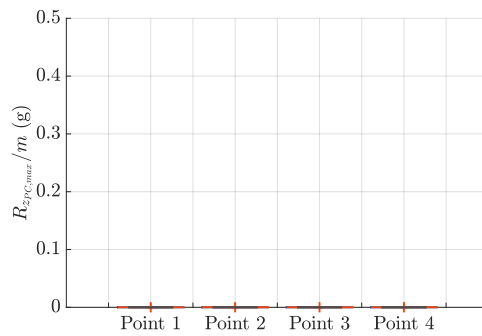

Figure 7.32: Gust TG boxplot

Figure 7.33: Gust PC boxplot

Figure 7.34: Gust boxplots

first two plots of figure 7.34, the LWG has a great increment with respect to all the other points, while the RWG is well below the others. The duration of the gust is always the same (50 m for the wavelength and almost 7 s for the temporal duration), but its peak value is way higher (3.5 m/s). This makes the adaptation phase pretty long and almost in time with respect to the touchdown (but never completed before it). As a consequence, the bank angle at the touchdown instant is positive (overshooting the zero value) and this lets the RWG land first. Then, the exact same case of points 2 and 3 occurs (with opposite skids): the vehicle pivots on the RWG and bounces back to the left one, producing a greater load on the latter.

However, the success rate for the loads of all points of the gust in table 7.16 is quite high, and instead, the xy-success is not so always satisfying, especially for point 4, where the peak of the gust plays a major role in exceeding the lateral allowed maximum value.

The last considerations are focused on the shear wind disturbance, referring to figure 7.40, and also the usual table 7.16 with the results.

To begin with, point 1 shows the already expected trend, where, in this case, the LWG touches down before the RWG, due to a negative bank angle at the touchdown instant. As already seen previously, the vehicle is still trying to adapt to the disturbance when it lands, and therefore the LWG receives a higher load than the RWG, which is barely touching the ground, with a very low average value for the acceleration.

While point 2 may seem rather distant from the previous point, especially due to the unusually high load of the LWG, it shows quite similar behaviour with regard to landing modes, i.e. first the LWG and then only slightly the RWG. However, while all skids see an average increase in their loads, the LWG has the highest one, which incidentally is the only one that goes beyond the structural limit. For this case in particular, the explanation is to be found in the in-depth study carried out in section 7.2.3, in which it was highlighted how, even with an average value of maximum value of the shear, the results in terms of assumed attitude once the second part of the shear meets the aircraft are amplified by the change of sign of the wind disturbance, in addition to the fact that, in this case, the global velocity variation is equal to 3 m/s, which is at the maximum tested condition of the parametric study.

In the case of point 3, there is a great overall decrease in all the loads, except for the RWG. This point, which is one of the only two points globally to always have a total success for every criterion, is constituted by a weak wind disturbance, with a maximum value of 0.5 m/s, which explains the low values for all the skids, but bring the vehicle in a particular condition with regards to the bank angle. In fact, since it is encountered a 3 meters, there is quite a good amount of time to adapt to it, if only the slope were not that small. A smaller value of the slope (0.5 m/s here) makes the disturbance more extensive over time, and then, at the touchdown, the vehicle is always barely banking to the right (coming from an overshoot that follows the previous negative bank). In the end, the landing is almost simultaneous, and the LWG and RWG loads are almost similar.

Point 4 has the same parameters as point 3, except for the height of the encounter. This means that,
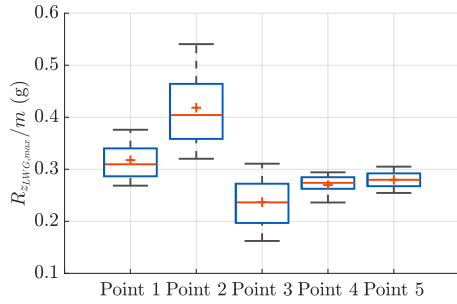
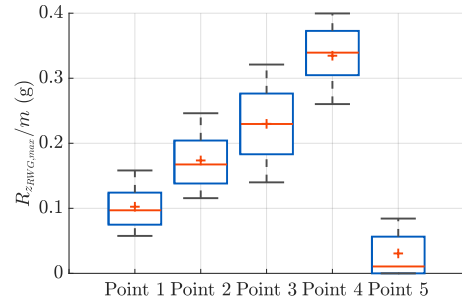Figure 7.35: Shear LWG boxplot

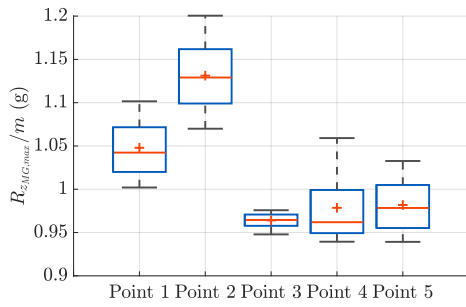Figure 7.36: Shear RWG boxplot
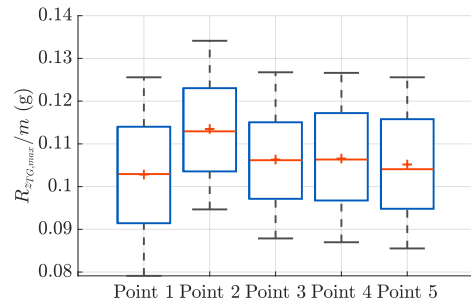

Figure 7.37: Shear MG boxplot
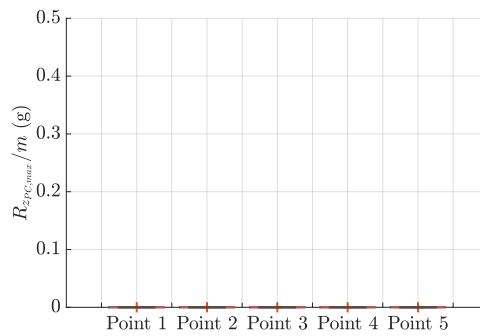

Figure 7.38: Shear TG boxplot

Figure 7.39: Shear PC boxplot

Figure 7.40: Shear boxplots

while having more time to recover from the second part of the shear, the bank angle is still positive (but in a decrease from the overshoot) at the touchdown instant. In addition, the heading of the vehicle is always greater than 270°, which makes the left side of the aircraft touch down first, but then immediately bounce back to the right. This is why the RWG is still increasing on average, while all the others are similar to the previous point.

Lastly, point 5 constitutes a rather peculiar condition, in that the contact of the RWG is sometimes absent. This is because, since the aircraft is adapted to the external disturbance (both in terms of bank angle and roll or yaw rate), the only element that distinguishes it from the undisturbed condition is the heading, which is greater than 270°, to counteract the disturbance coming from the right. Therefore, the aircraft behaves as if it were receiving a normal ramp-type disturbance, and so, once it lands, the disturbance stresses more the LWG, leaving the right one raised.

7.5   Landing capabilities

To summarise the results and draw up conclusive considerations on the landing process, a list of recurrent elements of an unsuccessful are listed below, trying to face a complete picture of what to avoid in order to achieve a successful landing.

- **xy criterion**: it is mainly influenced by the actual shape of the wind disturbance, as well as its duration and the height of the encounter. Generally speaking, whatever disturbance is encountered with a too-high peak and for a prolonged time interval, will probably make the vehicle land out of the runway.

- **MG liftoff criterion**: even if this element here was not so impactful on this analysis and the overall results, it has to be considered. In fact, a main gear liftoff case is strongly associated with an aircraft rollover in this case. Since the vertical loads on the main gear are never excessive, it is not associated with the liftoff of the complete aircraft. Instead if during and/or after touchdown the main gear lifts off, this is due to an excessive roll rate caused by strong lateral forces at the main skid. As soon as this occurs, the aircraft behaviour is uncontrolled and in the worst of cases the wing could make ground contact, destroying the structure. However, the few cases in which the MG was lifting off again were extreme cases, with very high values of the wind magnitudes.

- **Loads criteria**: for this part, some key points come out from the boxplot analysis, as well as previous considerations. To begin with, a late encounter is always letting the vehicle be in a transient condition, meaning that either the bank angle or the heading is not undisturbed. As a consequence, different things can happen depending on the specific situation, but generally either the vehicle can pivot on the wind-side skid, making the other one experience high stress or the wind is in any case hitting the skid also after the touchdown. Alternatively, even an early disturbance

can cause problems to the skids, but the trigger is always represented by the specific attitude of the vehicle in the proximity (and just after) the touchdown.

To conclude, as an engineering evaluation of the available data, the decided safety margin for the single criterion is expressed in the table 7.17, where the indicated number represents the minimum allowable percentage of success, either for the xy criterion and for the loads, is assumed to always be successful.

Table 7.17: Minimum percentage acceptance

Percentage	Minimum (%)
p_{ALL}	90

Then, by using the above-mentioned minimum percentage acceptance, table 7.16 can be extended and transformed into a conclusive success summary, displayed as table 7.18

Table 7.18: Final acceptability evaluation

Wind type	Point #	Acceptable
Ramp	2	No
	3	Yes
	4	Yes
Gust	1	No
	2	No
	3	No
	4	No
Shear	1	Yes
	2	No
	3	Yes
	4	Yes
	5	Yes

Chapter 8

Conclusions

This thesis aimed to explore and validate different landing configurations under conditions of crosswind disturbances in order to develop an appropriate landing controller, test the different wind disturbances and assess the landing capabilities and the framework of the new lateral friction model. The main elements developed in this work are outlined below:

- **Lateral friction force model**: useful to extend and improve the accuracy of the previous friction model. Starting with extensive literature research, ranging from helicopter skids to spaceplane skids, a final theoretical model was found in the Bekker model of the pressure-sinkage equation, used for the characterisation of the skid-terrain interaction. Then, once the correct parameters of the two soil types to be considered had been chosen, the values of the resulting friction coefficients were evaluated, and the main configuration was chosen to continue the analysis (grass-type terrain) because the relation between longitudinal and lateral coefficient seemed to be more reasonable for the grass than for asphalt.

- **Lateral controller**: used in the context of landing simulations. It is based on an energy method, inspired by the THCS (Total Heading Control System), and improved to respond to the necessities of the project. In particular, a 2nd order filter was applied to the noisy signals, many PI controllers were added to increase stability and to have more specific control over the single variables, and it was tested with a particular test wind input, consisting of a combination of ramps, gusts and constant wind. Additionally, an integral saturation was included to address the integral windup problem. The overall result is satisfactory and meets both the stated requirements and the expected results, i.e. the ability to keep the aircraft on track, whatever the external conditions.

- **Guidance algorithm**: crucial for the correct behaviour of the lateral controller, since it has the fundamental role of producing the correct input command to eliminate the lateral offset to the runway. A geometric approach has been used, being more general than a specific trajectory follower. In addition, a zero-crossing logic was implemented and successfully tested.

- **Different analyses and results**: used to evaluate the landing capabilities of the DLR HAP aircraft, to consider the limitations and to determine the limit cases for different wind types. Four different analyses were performed: the steady-state maximum crab angle analysis, the parameter study, the identification of the limiting cases with the help of the sensitivity analysis, and the batch process of the limiting cases. The main results include the overall maximum allowable crab angle for the grass terrain (13.47°) and extensive parametric characterisation of the three wind types, showing a significant influence of the altitude the wind disturbance is encountered at, the magnitude of the wind disturbance and the bank angle at the moment of touchdown. It turned out that the wind shear is the most critical disturbance type while gust encounters only rarely lead to a failed landing. Furthermore, overall limiting cases, signifying different combinations of parameters for each wind type were found. Finally, a Monte Carlo-based batch simulation was performed, within which all limiting cases were regarded in more detail. In doing so, continuous turbulence was superimposed on the wind perturbations and 1000 simulations were performed for each case. The final success rates for each case were different, ranging from 37% to 100% success rate.

By introducing a critical review of the work, less attention was given to some elements. The most important among them are listed here:

- **Tarmac friction model**: which was found to be not perfectly described by the theoretical model. In fact, the adopted Bekker model predicts the presence of ground penetration due to the pressure exerted on the skid, which is theoretically negligible on a rigid asphalt (like in the case of the tarmac), so it would be believable to experience less difference between the longitudinal and lateral friction coefficient values. However, as already said, the grass model is more conservative, and therefore it does not constitute a concern for the scientific value of the work.

- **Assumption of the aircraft as a point mass**: The aircraft was modelled as a point mass with prescribed mass and inertia characteristics as it is most common in the field of flight dynamics. While this is perfectly suitable for airborne analysis, this may pose a source of error for landing simulations in which a gear, touching down is further away from the aircraft's centre of gravity. In this case, it sometimes occurred that one of the wing skids touched down with a rebounce which in turn led the other wing skid to make ground contact. In some rare cases, this continued for a longer time leading to excess loads. However, in order to tackle this effect, a comprehensive logic was implemented that chose the maximum load values per skid based on its physical significance.

- **Runway's length**: it was considered to be infinite, without giving the possibility to check for any end-of-the-runway condition. However, the results show that only the very last encounters (encounter altitude below 5 m) are critical, and, in these conditions, the vehicle is always sinking, so it is not covering a long distance before the actual touchdown. If it takes the aircraft too much time to counteract a disturbance above h_{phase3} and the end of the runway is nearing, then a go-around will be needed.

To conclude, this work presents interesting scientific findings, both for the current development of the aircraft and the project and for future elements to be investigated, described briefly in the next chapter. In addition, the data set produced with this work can be used to make comparisons between simulation results and flight test results, currently scheduled for summer 2025.

Chapter 9

Future work

In this very last chapter, a brief list of the possible future hints is made, considering both some of the drawbacks found in this work and elements not considered so far:

- **Review of the tarmac friction model**: by the usage of different approaches, or even testing of some real skids to identify a more precise correlation between the friction coefficient and the dimensions of the skid for this different terrain type.

- **Engine shut-down procedure**: in order to prevent sinking if a disturbance is encountered right before the shut down of the engines. By doing so, the vehicle should not land until the equilibrium phase between *phase2* and *phase3* is not affected by any late wind component.

- **Touchdown configuration**: to study which could be the best attitude and general orientation to assume in the very last instants before the touchdown. In fact, some variables like the bank angle or the heading could be used to even further aggravate the allowable lateral wind conditions.

- **Non-zero sideslip landing**: to consider the possibility of withstanding higher absolute lateral disturbances, also because the ones tested in this work are quite low.

Bibliography

[1] Federal Aviation Administration (FAA). *Airplane Flying Handbook (FAA-H-8083-3C)*. 2021. Chap. 9.

[2] Federal Aviation Administration (FAA). *Airplane Flying Handbook (FAA-H-8083-3C)*. 2021. Chap. 4.

[3] I. I. Argatov. "Mathematical modeling of linear viscoelastic impact: application to drop impact testing of articular cartilage". In: The International Conference on BioTribology 2011. 2013, pp. 213–225.

[4] M. Bekker. *Introduction to terrain-vehicle systems*. Ann Arbor: The University of Michigan Press, 1969.

[5] R. C. Binns. "Normal and Crosswind Approach and Landing". URL: https://binnsflightservices.com/.

[6] J. E. Crosheck. "Skid Steering of Crawlers". In: *SAE Transactions* 84.2 (1975), pp. 1390–1404. URL: https://www.jstor.org/stable/44718025.

[7] R. C. Dreher and S. A. Batterson. *Coefficients of friction and wear characteristics for skids made of various metals on concrete, asphalt, and lakebed surfaces*. Tech. rep. Langley Research Center, Langley Air Force Base, VA, 1962.

[8] G. W. H. van Es, P. J. van der Geest, and T. M. H. Nieuwpoort. "Safety aspects of aircraft operations in crosswind". In: Flight Safety Foundation FSF, 11th Annual European Aviation Safety Seminar. Amsterdam: Nationaal Lucht- en Ruimtevaartlaboratorium (National Aerospace Laboratory - NLR), 1999.

[9] FAA. *Runway Overrun Prevention*. Tech. rep. 2007.

[10] D. J. Feld. "Stability and Steering Control During Slideout of Skid-equipped Horizontally Landing Spacecraft". In: AIAA/ASME 9th Structures, Structural Dynamics and Materials Conference. 68-308. Palm Springs, CA, 1968. DOI: https://doi.org/10.2514/6.1968-308.

[11] D. Fischenberg. "Identification of an Unsteady Aerodynamic Stall Model from Flight Test Data". In: Proceedings of the AIAA Atmospheric Flight Mechanics Conference. 1995, pp. 138–146.

[12] *Flight dynamics - Concepts, quantities and symbols - Part 1*. Tech. rep. ISO - International Organization for Standardization, 1988.

[13] G. Gonzalo et al. "On the capabilities and limitations of high altitude pseudo-satellites". In: *Progress in Aerospace Sciences* 98 (2018), pp. 37–56. DOI: `https://doi.org/10.1016/j.paerosci.2018.03.006`.

[14] "HAP alpha - High Altitude Platform". URL: `https://www.dlr.de/ft/en/desktopdefault.aspx/tabid-17605/`.

[15] Y. J. Hasan, N. Fezans, and A. Voß. "Landing Simulation of a High-altitude Platform With Skid-type Landing Gear – Flight Procedure, Controller, And Loads". In: 33rd Congress of the International Council of the Aeronautical Sciences. Stockholm, 2022.

[16] Y. J. Hasan and A. Roeser M.S. Voigt. "Evaluation of the controllability of a remotely piloted high-altitude platform in atmospheric disturbances based on pilot-in-the-loop simulations". In: *CEAS Aeronautical Journal* 14 (2023), pp. 225–242. DOI: `10.1007/s13272-022-00626-x`.

[17] Y. J. Hasan et al. "Flight mechanical analysis of a solar-powered high-altitude platform". In: *CEAS Aeronautical Journal* 14 (2023), pp. 201–223. DOI: `https://doi.org/10.1007/s13272-022-00621-2`.

[18] M. K. Kar. "Prediction of Track Forces In Skid-steering of Military Tracked Vehicles". In: *Journal of Terramechanics* 24.1 (1987), pp. 75–86.

[19] R. Khatwa and R. L. Helmreich. "Flight Safety Foundation - Approach-and-Landing Accident Reduction Task Force. Analysis of Critical Factors During Approach and Landing in Accidents and Normal Flight: Data Acquisition and Analysis Working Group Final Report". In: *SAE Transactions* 108.2 (1999), pp. 1173–1266.

[20] M. Kitano and M. Kuma. "An Analysis of Horizontal Plane Motion of Tracked Vehicles". In: *Journal of Terramechanics* 14.4 (1977), pp. 211–225.

[21] H. W. Krüs. "Criteria for crosswind variations during approach and touchdown at airports". In: Closing Symposium of the DFG Research Unit. Vol. 131. Braunschweig, 2016. DOI: `https://doi.org/10.1007/978-3-319-21127-5_10`.

[22] A. A. Lambregts. ""Integrated system design for flight and propulsion control using total energy principles". In: *AIAA paper* 83.2561 (1983). DOI: `https://doi.org/10.2514/6.1983-2561`.

[23] A. A. Lambregts. "THCS Generalized Airplane Control System Design". In: Proceedings of the EuroGNC 2013, 2nd CEAS Specialist Conference on Guidance, Navigation & Control. Delft, The Netherlands, 2013.

[24] A. A. Lambregts. "Total Energy Based Flight Control System". In: *United States Patent* 4,536,843 (1985).

[25] A. A. Lambregts. "Vertical flight path and speed control autopilot design using total energy principles". In: *AIAA paper* 83.2239 (1983), pp. 559–569. DOI: `https://doi.org/10.2514/6.1983-2239`.

[26]   J. C. Lansey. "Plot and compare histograms; pretty by default". URL: https://www.mathworks.com/matlabcentral/fileexchange/27388-plot-and-compare-histograms-pretty-by-default.

[27]   M. Nadeau Beaulieu, R. M. Botez, and A. Hiliuta. "Ground Dynamics Model Validation by Use of Landing Flight Test". In: *Journal of Aircraft* 44.6 (2007), pp. 2063–2067. DOI: https://doi.org/10.2514/1.26625.

[28]   M. Nadeau Beaulieu et al. "Ground Dynamics Model Validation by use of Landing Flight Test Data". In: AIAA Modeling and Simulation Technologies Conference and Exhibit. Keystone, Colorado, 2006.

[29]   General Accounting Office. *Aviation safety - FAA has not fully implemented weather-related recommendations: report to the Subcommittee on Technology, Committee on Science, House of Representatives.* Tech. rep. 1998. DOI: https://doi.org/10.21949/1403242.

[30]   A. J. Parente de Carvalho Júnior and P. Paglione. "Design of a flight control system based on the total heading control system philosophy". In: 19th International Congress of Mechanical Engineering. Brasilia, 2007.

[31]   S. Park, J. Deyst, and J. P. How. "A New Nonlinear Guidance Logic for Trajectory Tracking". In: AIAA Guidance, Navigation, and Control Conference and Exhibit. Providence, Rhode Island, 2004. DOI: https://doi.org/10.2514/6.2004-4900.

[32]   A. K. Sareen, M. R. Smith, and J. Howard. "Helicopter Skid Gear Dynamic Drop Analysis and Test Correlation". In: American Helicopter Society 54th Annual Forum. Washington, DC, 1998.

[33]   Airbus - Customer Services. *Flight Operations Briefing Notes.* Blagnac, 2006.

[34]   S. M. Stubbs. *Landing characteristics of a dynamic model of the HL-10 manned lifting entry vehicle.* Tech. rep. 68-308. Langley Research Center, Langley Station, Hampton, VA, 1966. DOI: https://doi.org/10.2514/6.1968-308.

[35]   C-H Tho et al. "Efficient Helicopter Skid Landing Gear Dynamic Drop Simulation Using LS-DYNA". In: *Journal of The American Helicopter Society* (2004), pp. 483–492.

[36]   R. D. Wismer and H.J. Luth. "Off-road Traction Prediction for Wheeled Vehicles". In: *Journal of Terramechanics* 10.2 (1973), pp. 49–61.

[37]   J. Wong. *Theory of Ground Vehicles.* 2nd ed. New York: John Wiley & Sons, Inc., 1993.